

DYNAMIC REACTOR OPERATION AND HIGH-TEMPERATURE CATALYSIS:  
DIRECT OXIDATION OF METHANE IN A REVERSE-FLOW-REACTOR

by

Dirk Walter Ralf Neumann

MS (Chemie-Diplom), Universität zu Köln, 1999

Submitted to the Graduate Faculty of  
School of Engineering in partial fulfillment  
of the requirements for the degree of  
Doctor of Philosophy

University of Pittsburgh

2003

UNIVERSITY OF PITTSBURGH

SCHOOL OF ENGINEERING

This dissertation was presented

by

Dirk Walter Ralf Neumann

It was defended on

July 23<sup>rd</sup>, 2003

and approved by

Anthony Cugini, Professor, Department of Energy

Robert Enick, Professor, Chemical and Petroleum Engineering Department

Irving Wender, Professor, Chemical and Petroleum Engineering Department

Dissertation Director: Götz Vesper, Professor,  
Chemical and Petroleum Engineering Department

to my parents

## ABSTRACT

### DYNAMIC REACTOR OPERATION AND HIGH TEMPERATURE CATALYSIS: DIRECT OXIDATION OF METHANE IN A REVERSE-FLOW-REACTOR

Dirk Neumann, PhD

University of Pittsburgh, 2003

Synthesis gas, a mixture of H<sub>2</sub> and CO, is a key intermediate product in the petrochemical industry. It is used for the production of methanol and liquid fuels (via Fischer-Tropsch synthesis), or as a source of hydrogen for ammonia synthesis and fuel cells.

An interesting alternative for the production of syngas to the conventionally used steam-reforming of methane (SRM) is catalytic partial oxidation of methane (CPOM) [1]. Here, methane is converted in a one-step process with oxygen or air over noble metal catalysts to synthesis gas. The reaction is characterized by extremely short contact times ( $\tau < 50$  ms) and very high temperatures exceeding 1000°C. While thermodynamics allow for optimum syngas yields, a complex interaction between total and partial oxidation reactions limits these under autothermal operation.

A way to overcome these autothermal limitations is by increasing catalyst temperatures, e.g. in a multifunctional reactor concept. A particularly efficient heat-integration is achieved through periodic switching of the direction of the gas flow in the dynamically operated reverse-flow reactor (RFR) [2].

We built a computer-controlled, laboratory-scale RFR for CPOM to gain general insights into the reaction behavior in this multifunctional reactor configuration. Experimental results demonstrate that total oxidation of methane can be reduced effectively, resulting in strongly increased syngas yields compared to autothermal reactor operation without heat integration.

Furthermore, maximum attainable syngas yields are shifted towards even shorter contact times compared to a conventional process, allowing for even higher space-time yields. In addition, experiments reveal that dynamic reactor operation intrinsically counteracts catalyst deactivation.

Detailed numerical simulations using elementary step kinetics are performed to investigate the influence of dynamic reactor operation on surface kinetics and reaction mechanism. It is shown that the reaction mechanism is characterized by methane partial and total oxidation reactions at the catalyst front edge, followed by endothermic reforming reactions in the second half of the catalyst bed, which occur due to advantageous temperature profiles in dynamic reactor operation.

Overall, the RFR is a promising configuration for efficient, small-scale production of syngas.

## ACKNOWLEDGEMENTS

I would foremost like to thank my advisor Dr. Götz Vesper for his constant support, the important, detailed discussions about my work and his exceptionally friendly and personal way of leading the research group. It has been an absolute pleasure working in his team.

Furthermore, I would like to thank my lab mates Sudipta, Mark, Judith, Arne, Uli Specht, Klaus Mehler and Tengfei for the fun we had in the lab which made work a lot more enjoyable.

In addition, I would like to thank the Max-Planck-Institute ‘für Kohlenforschung’, where I started my PhD, and their machine shop as well as Mr. Iländer for their help in building the reactor.

Finally, I would like to thank the faculty, staff and students of the Chemical Engineering Department at the University of Pittsburgh for their friendly support and help during my short stay in Pittsburgh.

Financial support by the ‘Fonds der Chemischen Industrie’ as well as the ‘Deutsche Forschungsgemeinschaft’ is gratefully acknowledged.

A big hug and kiss to my parents, my sister and Miriam for their love and support.

## TABLE OF CONTENTS

1.0	INTRODUCTION .....	1
2.0	FUNDAMENTALS .....	5
2.1	Production of Synthesis Gas .....	5
2.2	Catalytic Partial Oxidation of Methane .....	6
2.2.1	Multifunctional Reactor Concept: The Reverse-Flow Reactor .....	9
2.2.2	Regenerative Heat-Exchange .....	10
2.2.3	Surface Dynamics .....	12
2.2.4	Literature on CPOM in an RFR .....	14
2.3	Thermodynamics .....	16
3.0	EXPERIMENTS .....	19
3.1	Experimental Setup .....	19
3.2	Experimental Results .....	23
3.2.1	Dynamic Reactor Operation .....	23
3.2.2	Variation of the Feed Gas Composition .....	28
3.2.3	Variation of the Cycling Period .....	31
3.2.4	Variation of the Flow-Rate .....	32
3.2.5	Variation of the Pressure .....	39
3.2.6	Variation of the Catalyst Pore Size .....	40
3.2.7	Catalyst Deactivation .....	45
3.2.8	Testing Novel Nano-Structured Catalysts .....	54
3.3	Discussion .....	57

3.3.1	Reactor Temperatures and Syngas Yields .....	57
3.3.2	Converting Sensible Heat into Chemical Energy .....	58
3.3.3	Thermodynamics and Kinetics .....	62
4.0	REACTOR SIMULATION .....	67
4.1	Model Validation: Original Reactor Model in Steady-State Operation.....	67
4.2	Model Validation: Improved Reactor Model in Steady-State Operation .....	69
4.3	Model Validation: Improved Reactor Model in Dynamic Reactor Operation .....	75
4.4	Reaction Mechanism during Dynamic Reactor Operation .....	81
4.4.1	Reaction Mechanism during Initial Phase after Flow-Reversal .....	81
4.4.2	Reaction Mechanism during Second Part of a Semi-Cycle .....	86
4.5	Summary and Discussion.....	93
5.0	SUMMARY AND OUTLOOK.....	95
5.1	Summary .....	95
5.2	Outlook .....	96
	APPENDIX A .....	99
	APPENDIX B .....	100
	APPENDIX C .....	101
	APPENDIX D .....	104
	APPENDIX E .....	109
	APPENDIX F .....	110
	APPENDIX G .....	116
	APPENDIX H .....	126
	BIBLIOGRAPHY .....	131



## LIST OF TABLES

Table 1: <i>Reactor parameters for four different experimental long-term runs</i> .....	48
Table 2: <i>GC oven and detector parameters</i> .....	102
Table 3: <i>Retention times of gas phase components on a Haysep P column</i> .....	103
Table 4: <i>Energy and mass balance equations of the reactor model</i> .....	111
Table 5: <i>Reactor dimensions and physical properties used in the model</i> .....	112
Table 6: <i>Surface reaction steps and rate parameters</i> .....	113
Table 7: <i>Physical properties of a methane-air gas mixture</i> .....	121
Table 8: <i>Adjusted reaction rate parameters</i> .....	125

## LIST OF FIGURES

Figure 1: Oxygen ( $\theta_{O}$ ) and carbon ( $\theta_{C}$ ) surface coverages as well as $CO_2$ ( $y_{CO_2}$ ) and CO ( $y_{CO}$ ) mass fractions along the catalyst axis $z$ during ignition of CPOM on a Pt surface [15]; flow direction of the gases indicated by arrow.....	8
Figure 2: Schematic of regenerative heat-exchange in an RFR: Temperature profiles along the reactor axis $z$ during one semi-cycle .....	11
Figure 3: Schematic of mean temperatures along the reactor axis $z$ of a full cycle in periodic steady-state .....	12
Figure 4: Schematic of catalyst surface coverages ( $\theta_{O}$ : dashed line, $\theta_{C}$ : solid line) during a semi-cycle .....	13
Figure 5: Thermodynamic calculations: adiabatic (dashed lines) as well as optimum (solid lines) selectivities towards CO (left), $H_2$ (middle) and $CH_4$ conversions (right) as a function of the $CH_4/O_2$ ratio in a $CH_4$ /air mixture.....	18
Figure 6: Thermodynamic calculations: adiabatic (dashed lines) and optimum (solid lines) temperatures necessary to achieve maximum $S_{CO}$ (left), $S_{H_2}$ (middle) and $X_{CH_4}$ (right).....	18
Figure 7: Schematic of the RFR system.....	19
Figure 8: Quartz-metal hybrid reactor (left), foam monolith (middle) and extruded monolith (right) .....	21
Figure 9: Temperatures at the catalyst entrance and exit (left) as well as $H_2$ -concentrations at the reactor exit (right) during initial 7 minutes of transition from steady-state to dynamic RFR operation .....	24
Figure 10: Time dependent temperatures measured on either side of the catalyst bed; $CH_4/O_2 = 2.0$ , $\tau/2 = 15$ s, $\dot{V} = 3$ slm .....	25
Figure 11: $H_2$ - (left), $H_2O$ - (middle) and $CH_4$ - (right) concentrations during 2 semi-cycles ( $\tau/2 = 15$ s, $\dot{V} = 4$ slm, $CH_4/O_2 = 2.6$ ); .....	27
Figure 12: $S_{CO}$ (left), $S_{H_2}$ (middle) and $X_{CH_4}$ (right) as a function of the $CH_4/O_2$ -ratio for steady-state (SS, dotted lines) and RFR (solid lines) operation; ( $\dot{V} = 4$ slm, $\tau/2 = 15$ s).....	29

Figure 13: Temperatures as a function of the $CH_4/O_2$ -ratio: steady-state (left) and RFR (right) operation; $\dot{V} = 4$ slm, $\tau/2 = 15$ s .....	29
Figure 14: $S_{CO}$ (dashed line), $S_{H_2}$ (solid line) and $X_{CH_4}$ (dotted line, left) as well as maximum and mean temperatures (right) as a function of the cycling period $\tau/2$ ( $\dot{V} = 4$ slm, $CH_4/O_2 = 2.0$ ) .....	31
Figure 15: $S_{CO}$ (left), $S_{H_2}$ (middle) and $X_{CH_4}$ (right) as a function of the flow-rate for steady-state (SS, dotted lines) and RFR (solid lines) operation; $CH_4/O_2 = 2.0$ , $\tau/2 = 15$ s .....	33
Figure 16: Catalyst temperatures as a function of the flow-rate; left: steady-state (SS) reactor, right: RFR; $CH_4/O_2 = 2.0$ , $\tau/2 = 15$ s .....	34
Figure 17: Thermo-camera scans along the reactor axis with varying flow-rates .....	35
Figure 18: Temperatures in the RFR at the catalyst entrance and exit during 2 semi-cycles at 1 (left), 3 (middle) and 5 slm; $\tau/2 = 15$ s, $CH_4/O_2 = 2.0$ .....	36
Figure 19: Steady-state temperature profiles along the reactor axis $z$ in the conventional process: 1 (dashed line), 3 (solid line) and 5 (dotted line) slm; flow-direction indicated by arrow... 38	
Figure 20: Mean temperature profiles along the reactor axis $z$ in the dynamic RFR: 1 (dashed line), 3 (solid line) and 5 (dotted line) slm .....	38
Figure 21: Pressure drop across the reactor for 1 (circles), 3 (squares) and 5 (diamonds) slm during 2 semi-cycles (left); Mean syngas selectivities and $X_{CH_4}$ as a function of the absolute pressure (right); $CH_4/O_2 = 2.0$ , $\dot{V} = 4$ slm, $\tau/2 = 15$ s .....	40
Figure 22: $S_{CO}$ as a function of the flow-rate for 30 (left), 45 (middle) and 80 ppi (right) monolith; steady-state (SS, dotted lines) and RFR (solid lines) operation, $CH_4/O_2 = 2.0$ , $\tau/2 = 15$ s .....	43
Figure 23: $S_{H_2}$ as a function of the flow-rate for 30 (left), 45 (middle) and 80 ppi (right) monoliths; steady-state (SS, dotted lines) and RFR (solid lines) operation, $CH_4/O_2 = 2.0$ , $\tau/2 = 15$ s .....	43
Figure 24: $X_{CH_4}$ as a function of the flow-rate for 30 (left), 45 (middle) and 80 ppi (right) monoliths; steady-state (SS, dotted lines) and RFR (solid lines) operation, $CH_4/O_2 = 2.0$ , $\tau/2 = 15$ s .....	44
Figure 25: Steady-state temperatures as a function of the flow-rate for 30 (left), 45 (middle) and 80 ppi (right) monoliths, $CH_4/O_2 = 2.0$ .....	44
Figure 26: RFR temperatures as a function of the flow-rate for 30 (left), 45 (middle) and 80 ppi (right) monoliths, $CH_4/O_2 = 2.0$ , $\tau/2 = 15$ s .....	45

Figure 27: $S_{CO}$ (left), $S_{H_2}$ (middle) and $X_{CH_4}$ (right) as a function of catalyst activity; steady-state (dotted lines) and RFR (solid lines) operation; $CH_4/O_2 = 2.0$ , $\dot{V} = 4$ slm, $\tau/2 = 15$ s.....	47
Figure 28: Catalyst temperatures of the steady-state (SS, left) and the RFR process as a function of reactor catalyst activity; $CH_4/O_2 = 2.0$ , $\dot{V} = 4$ slm, $\tau/2 = 15$ s.....	48
Figure 29: $S_{CO}$ (left), $S_{H_2}$ (middle) and $X_{CH_4}$ (right) as a function of time: run 1: solid circles and dashed lines; run 2: hollow squares and solid lines; run 3: solid diamonds and solid lines; run 4: hollow triangles and dotted lines.....	51
Figure 30: RFR temperatures as a function of time; run 1: solid circles and dashed lines; run 2: hollow squares and solid lines; run 3: solid diamonds and solid lines; run 4: hollow triangles and dotted lines.....	52
Figure 31: $X_{CH_4}$ (dotted line), $S_{CO}$ (dashed line) and $S_{H_2}$ (solid line, left) as well as RFR temperatures (right) as a function of time using a Pt nano-catalyst; $CH_4/O_2 = 2.0$ , $\dot{V} = 4$ slm, $\tau/2 = 15$ s.....	56
Figure 32: $S_{CO}$ (left), $S_{H_2}$ (middle) and $X_{CH_4}$ (right) as a function of the $CH_4/O_2$ ratio using Pt nano-catalyst; steady-state (dashed lines) and RFR (solid lines) operation; $\dot{V} = 4$ slm, $\tau/2 = 15$ s.....	56
Figure 33: Schematic $H$ vs. $T$ diagram illustrating function principle of RFR.....	59
Figure 34: Efficiency of heat-integration in the RFR as a function of $CH_4/O_2$ -ratio ( $\dot{V} = 4$ slm, $\tau/2 = 15$ s, left), flow-rate ( $CH_4/O_2 = 2.0$ , $\tau/2 = 15$ s, middle) and catalyst deactivation ( $CH_4/O_2 = 2.0$ , $\tau/2 = 15$ s, $\dot{V} = 4$ slm, right).....	61
Figure 35: $S_{CO}$ (dashed line), $S_{H_2}$ (solid line) and $X_{CH_4}$ (dotted line) in thermodynamic equilibrium for a $CH_4/O_2$ ratio of 2.0 at different temperatures.....	63
Figure 36: Mole fractions of reactants and products in CPOM as a function of residence time at 1200°C (left) and 900°C (right); composition at $\tau = 0$ s equal to typical product composition measured in CPOM.....	64
Figure 37: Gas phase oxygen mole fractions versus reactor length at $T = 1000^\circ\text{C}$ : heterogeneous (solid line) vs. homogeneous (dashed line) kinetics ( $CH_4/O_2 = 2.0$ , $\dot{V} = 4$ slm, steady-state process).....	65
Figure 38: Schematic gas-composition vs. temperature diagram: thermodynamic equilibrium and kinetic influence.....	66
Figure 39: $S_{CO}$ (left), $S_{H_2}$ (middle) and $X_{CH_4}$ (right) as a function of the $CH_4/O_2$ ratio ( $\dot{V} = 4$ slm); experimental data (diamonds) and simulation results (lines, original model).....	68
Figure 40: Catalyst exit (left) and entrance (right) temperatures with varying $CH_4/O_2$ ratios ( $\dot{V} = 4$ slm); experimental data (diamonds) and simulation (lines, original model).....	69

Figure 41: $S_{CO}$ (left), $S_{H_2}$ (middle) and $X_{CH_4}$ (right) as a function of $CH_4/O_2$ ratio ( $\dot{V} = 4$ slm); experiments (dots) and simulation (lines, improved reactor model) results in steady-state reactor operation .....	71
Figure 42: Catalyst exit (left) and entrance (right) temperatures as a function of $CH_4/O_2$ ratio ( $\dot{V} = 4$ slm); experiments (dots) and simulation (lines, improved reactor model) results in steady-state reactor operation .....	72
Figure 43: $S_{CO}$ (left), $S_{H_2}$ (middle) and $X_{CH_4}$ (right) as a function of the flow-rate ( $CH_4/O_2 = 2.0$ ); comparison between experiments (dots) and simulation results (improved model, lines) ...	73
Figure 44: Catalyst exit (left) and entrance (right) temperatures as a function of the flow-rate ( $CH_4/O_2 = 2.0$ ); experiments (dots) and simulation (improved model, lines) .....	74
Figure 45: $S_{CO}$ (left), $S_{H_2}$ (middle) and $X_{CH_4}$ (right) as a function of the $CH_4/O_2$ ratio in dynamic reactor operation ( $\dot{V} = 4$ slm, $\tau/2 = 15$ s); comparison between experiments (dots) and simulation (lines, improved model).....	75
Figure 46: Mean catalyst entrance (left) and exit (middle) as well as maximum (at catalyst entrance/exit, right) temperatures as a function of the $CH_4/O_2$ ratio in RFR operation ( $\dot{V} = 4$ slm, $\tau/2 = 15$ s); experiments (dots) and simulation (lines, improved model).....	76
Figure 47: Time dependent temperatures measured on either side of the catalyst bed; left: simulation (improved model), right: experiment; $CH_4/O_2 = 2.0$ , $\tau/2 = 15$ s, $\dot{V} = 4$ slm.....	77
Figure 48: Time dependent $H_2$ (top), $H_2O$ , $CH_4$ , $CO_2$ and $CO$ (bottom) concentrations measured at the reactor exit during 2 semi-cycles; comparison between simulation (left, improved model) and experiment (right); $CH_4/O_2 = 2.0$ , $\tau/2 = 15$ s, $\dot{V} = 4$ slm.....	79
Figure 49: Schematic of gas accumulations during initial phase after flow-reversal .....	82
Figure 50: Partial and total oxidation product as well as $CH_4$ and $O_2$ concentrations at the reactor exit during initial 0.3 s after flow-reversal using improved reactor model ( $CH_4/O_2 = 2.0$ , $\tau/2 = 15$ s, $\dot{V} = 4$ slm) .....	83
Figure 51: Partial (left) and total (right) oxidation product concentrations along the center portion of the reactor (catalyst between $110 < z < 120$ mm, dark) during initial 0.2 s after flow-reversal (improved reactor model); flow-direction indicated by arrow ( $CH_4/O_2 = 2.0$ , $\tau/2 = 15$ s, $\dot{V} = 4$ slm) .....	84
Figure 52: Temperature profiles along the center portion of the reactor (catalyst between $110 < z < 120$ mm, dark) during initial 0.2 s after flow-reversal (improved reactor model), flow-direction indicated by arrow; $CH_4/O_2 = 2.0$ , $\tau/2 = 15$ s, $\dot{V} = 4$ slm .....	85
Figure 53: Syngas selectivities at the reactor exit during two semi-cycles; $CH_4/O_2 = 2.0$ , $\tau/2 = 15$ s, $\dot{V} = 4$ slm (calculated using improved reactor model) .....	86

Figure 54: <i>Partial (left) and total (right) oxidation product concentrations along the catalyst axis <math>z</math> during one semi-cycle (15 s); flow-direction indicated by arrow; <math>CH_4/O_2 = 2.0</math>, <math>\dot{V} = 4</math> slm; improved reactor model</i> .....	87
Figure 55: <i>Catalyst temperatures (upper left), <math>CH_4</math> concentrations (upper right), C- (lower left) and O- (lower right) surface coverages along the catalyst axis <math>z</math> during one semi-cycle (15 s); flow-direction indicated by arrow; <math>CH_4/O_2 = 2.0</math>, <math>\dot{V} = 4</math> slm; improved model</i> .....	89
Figure 56: <i>Catalyst temperatures as well as <math>CH_4</math>, partial and total oxidation product concentrations along the catalyst axis at 1 (solid line), 5 (dashed line), 10 (dots) and 15 s (dotted line) after flow-reversal; flow-direction from left to right; <math>CH_4/O_2 = 2.0</math>, <math>\tau/2 = 15</math> s, <math>\dot{V} = 4</math> slm (calculated using improved reactor model)</i> .....	92
Figure 57: <i><math>O_2</math> concentrations along the catalyst axis during one semi-cycle; <math>CH_4/O_2 = 2.0</math>, <math>\tau/2 = 15</math> s, <math>\dot{V} = 4</math> slm (calculated using improved reactor model)</i> .....	93
Figure 58: <i>Schematic of the GC column setup in oven 1</i> .....	102
Figure 59: <i>Syngas selectivities and methane conversions (left) as well as catalyst temperatures (right) as a function of mass transfer coefficient <math>\beta</math>; <math>CH_4/O_2 = 2.0</math>, <math>\dot{V} = 4</math> slm</i> .....	118
Figure 60: <i>Partial oxidation selectivities and methane conversions (left) as well as catalyst temperatures (right) as a function of catalyst thermal conductivity; <math>CH_4/O_2 = 2.0</math>, <math>\dot{V} = 4</math> slm</i> .....	119
Figure 61: <i>Syngas selectivities and methane conversions (left), catalyst temperatures (right) as a function of <math>a_v</math>; <math>CH_4/O_2 = 2.0</math>, <math>\dot{V} = 4</math> slm, <math>\beta = 0.05</math> m/s</i> .....	122
Figure 62: <i><math>O_2</math>- (upper left) and <math>CH_4</math>- (upper right) concentrations as well as C- (lower left) and O- (lower right) surface coverages along the catalyst axis <math>z</math> between 0.04 and 0.14 s after flow-reversal; <math>CH_4/O_2 = 2.0</math>, <math>\tau/2 = 15</math> s, <math>\dot{V} = 4</math> slm (calculated using improved reactor model)</i> .....	127
Figure 63: <i>Partial (left) and total (right) oxidation product concentrations along the catalyst axis <math>z</math> between 0.04 and 0.14 s after flow-reversal; <math>CH_4/O_2 = 2.0</math>, <math>\tau/2 = 15</math> s, <math>\dot{V} = 4</math> slm (calculated using improved reactor model)</i> .....	128
Figure 64: <i>Catalyst temperatures along the catalyst axis <math>z</math> between 0.04 and 0.14 s after flow-reversal, <math>CH_4/O_2 = 2.0</math>, <math>\tau/2 = 15</math> s, <math>\dot{V} = 4</math> slm (calculated using improved reactor model)</i> .....	128

## LIST OF SYMBOLS

$\alpha$	[W/m <sup>2</sup> /K]	heat-transfer coefficient
$a_v$	[m <sup>2</sup> /m <sup>3</sup> ]	specific surface area
$\beta$	[m/s]	mass transfer coefficient
$c_p$	[J/mol/K]	heat-capacity
cpi	[-]	cells per square inch
$d_m$	[cm]	monolith diameter
$D_{eff}$	[m <sup>2</sup> /s]	dispersion coefficient
$E_{act}$	[kJ/mol]	activation energy
$\varepsilon$	[-]	monolith porosity
$\eta$	[-]	efficiency
$\Delta H_r$	[kJ/mol]	reaction enthalpy
$\dot{H}_{sh}$	[kJ/s]	flow of sensible heat
$\Delta \dot{H}_{RFR-SS}$	[kJ/s]	difference in flow of latent heat between RFR and steady-state process
i.d.	[cm]	inner diameter
$k_{ext}$	[W/m <sup>2</sup> /K]	external heat-loss coefficient
$l_{cat}$	[cm]	catalyst bed length
$\lambda$	[W/m/K]	thermal conductivity
$\mu$	[kg/m/s]	viscosity
$\dot{n}_i$	[mol/s]	molar flow of species i
o.d.	[cm]	outer diameter
p	[bar]	pressure
ppi	[-]	pores per linear inch

$\rho$	[kg/m <sup>3</sup> ]	density
$S_{H_2}$	[%]	hydrogen selectivity
$S_{CO}$	[%]	carbon-monoxide selectivity
$t$	[s]	time
$\tau$	[s]	cycling period
$T$	[°C, K]	temperature
$\Delta T_{ad}$	[K]	adiabatic temperature rise
$\dot{V}$	[slm]	volumetric flow-rate in standard liters per minute (slm)
$X_{CH_4}$	[%]	methane conversion
$z$	[mm]	reactor length



## 1.0 INTRODUCTION

The exploitation of natural gas as an alternative to crude oil is gaining increased attention in recent years. Apart from the utilization as a source of energy (due to the large heat of combustion relative to  $\text{CO}_2$  formed), natural gas can also be used for the production of liquid chemicals necessary for many large-scale industrial processes. The uncertainty about remaining world oil reserves and unstable oil prices therefore prompts the currently oil based petrochemical industry to investigate processes which use natural gas as a substitute feedstock.

The known reserves of natural gas are enormous and challenge those of crude oil. Furthermore, natural gas is found as a by-product of crude oil reserves. Since oil wells are often located in remote locations far from industrial complexes, this energy source is so far not exploited sufficiently. As the transportation of gaseous fuels is expensive, it is desirable to convert the natural gas into liquid fuels (e.g. methanol or hydrocarbons via the Fischer-Tropsch (FT) reaction [3]). In addition, about 10 % of the natural gas is currently flared, polluting the environment (both  $\text{CH}_4$  and  $\text{CO}_2$  are greenhouse gases) [4, 5]. Strategies for the efficient exploitation of natural gas must therefore take into consideration the intended use, location as well as infrastructure.

Natural gas mainly consists of methane (~95 %) and traces of higher hydrocarbons as well as some nitrogen. Methane can be converted either directly (i.e. in a one step process) or indirectly (via several steps) into liquid chemicals. While the direct conversion is still studied at a fundamental level [4] and results in low reaction yields, the indirect process is frequently applied in industry. Here, methane is converted in a primary step to synthesis gas (syngas;  $\text{H}_2$ -CO mixture), followed by different processes to manufacture the desired chemical [3]. These processes are well known and have been used industrially for many decades.

While the production of syngas is a required step in the indirect conversion of methane, it is also responsible for a large part of the total investment costs in a large scale industrial plant. Consequently, much research is focusing on the improvement of current, as well as the development of novel, more efficient processes for the conversion of methane to syngas.

A promising technology that has received much attention during the last decade is catalytic partial oxidation of methane (CPOM) at high temperature and short contact time conditions. In

this process, methane is converted with oxygen or air over noble metal catalysts to syngas in a simple, one-step reaction. The system is characterized by extreme autothermal temperatures exceeding 1000°C, which result in very high reaction rates and hence very high space-time yields can be achieved. While the exothermicity of the reaction renders expensive external heating for autothermal operation unnecessary, fast reaction rates allow for compact reactors which would make the conversion of methane in remote locations or in mobile applications feasible.

CPOM has been studied intensively both experimentally and in detailed reactor simulations during the last decade [1, 6-16]. However, the process still lacks the development of an adequate reactor concept. Also, a close investigation of thermodynamics as well as kinetics governing the system is necessary to optimize the process.

Thermodynamics show that in CPOM, a complex interaction between partial and total oxidation reactions effectively limits obtainable syngas yields under autothermal operation: High temperatures, which are thermodynamically necessary for good syngas yields, are only achieved due to combustion of some of the methane feed, which is by definition detrimental for syngas selectivities.

Veser et al. [15] investigated the kinetics of CPOM over Pt monoliths using detailed numerical simulations. They proposed that the catalyst bed can be divided into two sections: a total oxidation zone at the catalyst entrance which coincides with a dominant oxygen coverage on the catalyst surface, followed by a partial oxidation zone and a dominant carbon coverage. Veser suggests a close correlation between reaction selectivities and surface coverages.

To improve the process (i.e. increase reaction yields) above the limit set by autothermal operation, the formation of the total oxidation products must be reduced (or at best eliminated) while at the same time the high temperatures, which are thermodynamically necessary for high syngas yields, must be maintained. This can be achieved by providing additional heat to the system and increasing the catalyst temperature, e.g. by preheating the feed gas. Initial investigations by Hickman and Schmidt [17] showed that preheating of the reactants indeed results in increased syngas yields. While external preheating can be realized easily, it is expensive and hence not economical. A much more profitable way is to integrate the sensible heat leaving the reaction zone in a multifunctional reactor concept [18, 19]. Friedle and Veser

[20] observed enhanced partial oxidation selectivities when performing CPOM in a counter current heat-exchange reactor.

A much more efficient heat-integration - compared to recuperative heat-exchange in a counter current heat-exchange reactor - is achieved by regenerative heat-exchange in a dynamically operated reverse-flow reactor (RFR) [19, 21]. In this reactor configuration, the flow-direction of the gases through the reaction tube is reversed periodically, while solid state heat-reservoirs placed on either side of the catalyst bed allow for a very efficient regenerative heat-exchange [22].

Conducting CPOM in an RFR allows the raising of catalyst temperatures based on the mildly exothermic partial oxidation reaction. Total oxidation is reduced and syngas yields can thus be enhanced above the limits set by autothermal operation. Additionally, periodic flow-reversal results in an inversion of the surface coverages with respect to the flow direction of the gases. As a result, transient coverages develop for a certain time-period before steady-state values are again reached. As mentioned above, surface coverages have a decisive influence on reaction selectivities. By adjusting the switching periodicity it might be possible to tailor surface coverages in a way to 'kinetically' suppress total oxidation and thus enhance syngas yields.

It is the aim of this work to evaluate the performance of CPOM in an RFR. After a brief overview of current technologies for the production of syngas, in particular CPOM, chapter 2.0 explains in detail the principle of regenerative heat-exchange in an RFR. Furthermore, a possible process enhancement by stabilizing transient surface coverages in the dynamic reactor is illustrated. Thermodynamic calculations comparing adiabatic and optimum syngas yields (hence quantifying the limitations set by autothermal reactor operation) conclude the introductory part of this thesis.

A laboratory scale reactor is used to experimentally investigate characteristics of the process and develop a systematic understanding of the reaction and reactor behavior. A description of the experimental setup as well as experiments performed is presented in chapter 3.0. It is generally observed that efficient heat-exchange in dynamic reactor operation strongly increases catalyst entrance temperatures and syngas yields when compared to a conventional reactor without heat-integration. Additionally, maximum attainable syngas yields are shifted towards even shorter contact times and hence higher space-time yields in the RFR. Long-term experiments reveal that regenerative heat-exchange intrinsically counteracts catalyst deactivation in the RFR and results

in a slower decrease of syngas yields with decreasing catalyst activity when compared to a conventional process. Generally, the presented data suggests that enhancements observed in the RFR are due to heat-integration in the multifunctional reactor concept and advantageous temperature profiles along the reactor axis. However, excessive temperatures and the onset of homogeneous reactions limit the stability of the system and reduce the applicable range of flow-rates. The experimental part of this thesis concludes with a detailed discussion. Calculations are performed to estimate the efficiency of regenerative heat-exchange in the laboratory setup. Additionally, a particular focus is placed on evaluating the importance of catalytic surface kinetics in the system as compared to thermodynamics. Experimental data shows that product concentrations are not at thermodynamic equilibrium, which suggests that due to short residence times of gases in the reaction zone, secondary reforming and water gas shift reactions do not reach equilibrium.

Apart from thermal enhancements in the RFR, it is also investigated whether inversion of surface coverages immediately following flow-reversal has an effect on syngas yields. Because high temperatures result in very low surface coverages which make an experimental investigation of this feature impossible, detailed numerical simulations are performed which are described in chapter 4.0. In a first step, an existing model is used and compared to experimental data of the conventional process without heat-integration. While yields and catalyst exit temperatures match well, catalyst entrance temperatures are strongly over-predicted by the model. Therefore, the model is extended to better fit experimental data. Using this improved model, the dynamic process is simulated. Investigation of the reaction mechanism in the dynamic process reveals that the catalyst bed can be divided into two parts: an initial oxidation zone (partial and total) is followed by a reforming section. The extent to which these reactions occur is solely dependent on dynamic temperature profiles along the catalyst axis, which are influenced by regenerative heat-exchange in RFR operation. Additionally, results indicate that surface kinetics occur orders of magnitude faster than the thermal dynamics of the system and can be regarded as quasi-stationary. Effects of transient surface coverages on syngas yields are not observed.

Chapter 5.0 concludes this work with a summary and outlook.

## 2.0 FUNDAMENTALS

### 2.1 Production of Synthesis Gas

Synthesis gas, a mixture of H<sub>2</sub> and CO, is one of the most important intermediate products in the petrochemical industry, where, for example, it is used for the production of methanol, hydrocarbons or as a source of hydrogen in the ammonia synthesis [3-5, 23, 24]. There are three processes commonly used for the production of syngas: steam reforming of methane (SRM), autothermal reforming (ATR) and partial oxidation of methane (POM).

Steam reforming of methane is the key reaction frequently used in industry. Here, methane is converted with water over Ni-catalysts in a strongly endothermic reaction to yield CO and H<sub>2</sub> in a molar ratio of 1:3:



The process is conducted in large tubular reformers to achieve high temperatures which are thermodynamically necessary for good syngas yields, making SRM a major energy consumer. For most downstream processes (e.g. methanol and Fischer-Tropsch synthesis) the desired H<sub>2</sub>/CO ratio is 2.0. Therefore, the steam reformer is typically followed by additional water gas shift stages in the process scheme to adjust the H<sub>2</sub>/CO ratio to the desired value:

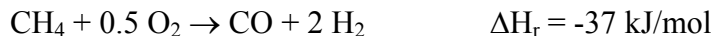


As the residence times inside the reactors lie in the range of 1 s, large reactor volumes are necessary for high throughputs.

ATR, also known as the Topsoe process, is a combination of homogeneous oxidation of methane and subsequent reforming reactions inside a single reactor vessel. Methane and oxygen (CH<sub>4</sub>/O<sub>2</sub> ratio of ~1.7) as well as small amounts of water (to reduce carbon formation) are fed to a burner where they react homogeneously to a mixture of partial and total oxidation products.

Autothermal temperatures above 2000 K are achieved. The mixture is then directed over a Ni catalyst, where endothermic reforming and shift reactions occur, resulting in thermodynamic equilibrium composition at the exit temperature of the catalyst [23]. The main advantage of ATR compared to SRM is the autothermal operation, with a shortcoming being the necessity of feeding pure oxygen (which is expensive to produce) to achieve the high temperatures.

An interesting alternative to these frequently used industrial processes is partial oxidation of methane, first investigated as early as 1946 by Prettre at al. [25]. In this process, methane is converted with oxygen or air to form H<sub>2</sub> and CO in a one-step reaction, directly yielding an H<sub>2</sub>/CO ratio of 2:



Due to the mild exothermicity of the partial oxidation route, this reaction can be conducted autothermally and is hence potentially clean (i.e. the process does not produce any emissions). Furthermore, the CO:H<sub>2</sub> ratio of 1:2 is ideal for most downstream processes, making partial oxidation of methane a simple, one-step process.

A non-catalytic partial oxidation process was developed by Texaco and Shell which results in high syngas yields at high temperatures and pressures [23]. Problems related to the homogeneous process are excessive temperatures, long residence times as well as excessive coke formation, which strongly reduce the controllability of the process.

## 2.2 Catalytic Partial Oxidation of Methane

Catalytic partial oxidation of methane (CPOM) over various transition and noble metals is characterized by reaction temperatures exceeding 1000°C, which result in very high reaction rates and thus extremely short residence times in the millisecond range (hence the name of this class of reactions: ‘high-temperature short contact time catalysis’) [17]. The H<sub>2</sub>/CO-ratio, the compactness of the reactor (due to the short residence times) and the autothermal operation make this process particularly attractive for syngas production where simple and compact, yet efficient processes are required.

Thermodynamic calculations for a methane/air system (chapter 2.3) show that temperatures around 1000-1100°C are necessary to achieve optimum syngas yields. As in the non-catalytic process, however, the high temperatures observed under autothermal operation cannot be achieved due to the mild exothermicity of the partial oxidation route ( $\Delta H_r = -37$  kJ/mol,  $\Delta T_{ad} \sim 250$  K), but rather due to combustion (total oxidation) of some of the methane feed, which is a highly exothermic reaction ( $\Delta H_r = -800$  kJ/mol,  $\Delta T_{ad} \sim 2000$  K). The reaction equilibrium is ultimately characterized by a complex interaction between partial and total oxidation reactions: while the combustion of methane results in high temperatures, these high temperatures shift the reaction equilibrium towards the partial oxidation route. Partial oxidation is only mildly exothermic, which thus leads to lower temperatures (relative to combustion), favoring total oxidation reactions. Overall, this interplay reduces obtainable partial oxidation yields under autothermal operation.

The kinetics of the heterogeneously catalyzed reaction on a Pt surface were investigated by Vesper and Frauhammer [15]. Detailed numerical simulations revealed that total oxidation occurs due to a preferential oxygen adsorption onto the catalyst surface. As a consequence, in a steady-state process, an oxygen rich zone forms at the catalyst front edge which primarily results in the combustion of methane. This total oxidation is generally detrimental for syngas selectivities, but the strong exothermicity of the reaction results in high temperatures which are necessary to push reaction selectivities towards the partial oxidation products in the further course of the reaction. Following the oxygen coverage, the catalyst surface is predominantly covered with carbon which coincides with the formation of partial oxidation products. The catalyst bed can therefore generally be divided into two parts: a zone at the catalyst entrance with a dominantly oxygen covered surface, which leads to total oxidation of methane and high temperatures. This is followed by a zone with a dominantly carbon covered surface which yields the desired syngas selectivities.

Modeling of the ignition process confirmed these findings. Figure 1 shows oxygen and carbon surface coverages as well as CO<sub>2</sub> and CO concentrations in the gas phase during initial stages of the ignition process along the catalyst axis  $z$  (reproduced from [15]).

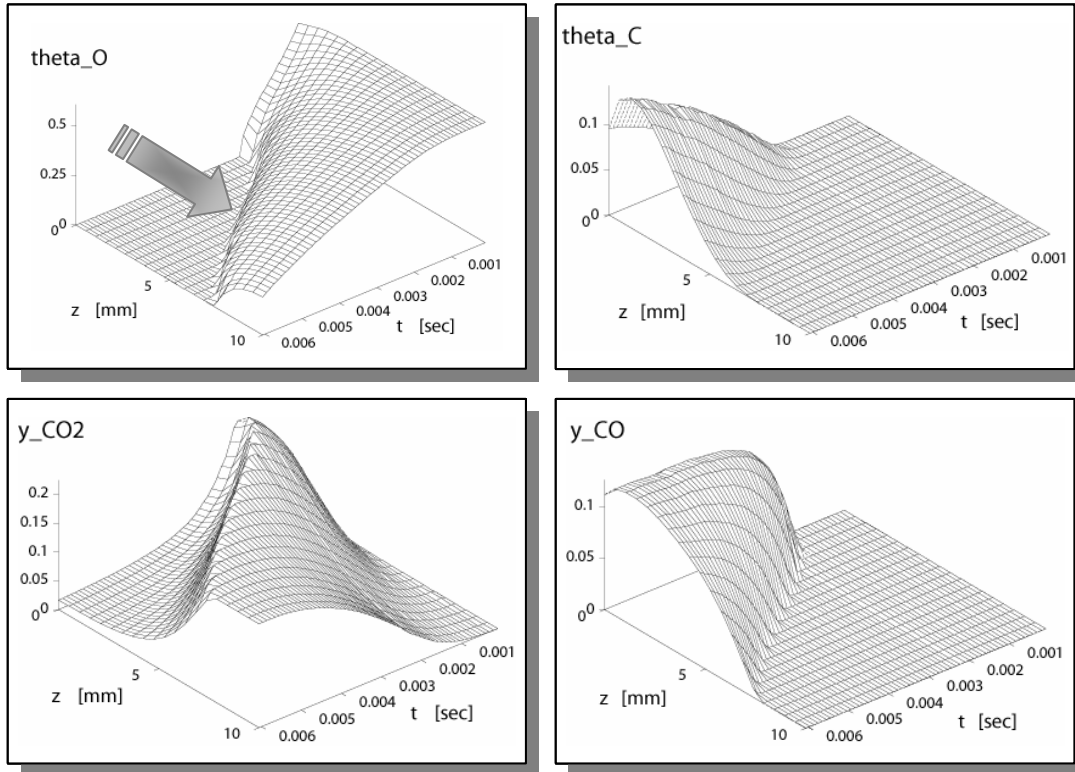


**Figure 1:** Oxygen ( $\theta_O$ ) and carbon ( $\theta_C$ ) surface coverages as well as  $CO_2$  ( $y_{CO_2}$ ) and CO ( $y_{CO}$ ) mass fractions along the catalyst axis  $z$  during ignition of CPOM on a Pt surface [15]; flow direction of the gases indicated by arrow

Before ignition, the catalyst surface is completely covered with oxygen due to a higher oxygen sticking coefficient on the Pt surface compared to methane. Once the reaction ignites at the front edge of the catalyst, oxygen is removed from the surface. In parallel, a  $CO_2$  wave is pushed through the reactor. As soon as the surface sites are free of oxygen, carbon is deposited on the surface and partial oxidation to CO occurs. Veser thus suggested that surface coverages have a decisive influence on reaction selectivities and hence syngas yields.

The dominant reaction mechanism of CPOM over different metal catalysts has been debated heavily in the literature over several years. The two reaction pathways discussed are the direct route, where CO and  $H_2$  are formed directly from methane, and the indirect route, where initial methane combustion is followed by secondary reforming and water-gas shift reactions to yield partial oxidation products. Even though both reaction pathways theoretically (in an adiabatic reactor and sufficiently long residence times) result in the same product gas composition, the



route taken has a decisive influence on temperature profiles and spatial concentrations along the reactor axis. It is generally suggested that the dominant mechanism is dependent on the catalyzing metal: indirect route for transition metal catalysts like Ni [25, 26], and direct oxidation over noble metal catalysts [17, 27]. A detailed discussion regarding the reaction pathway in the investigated system is performed in chapter 4.4.

As mentioned above, thermodynamics limit obtainable syngas yields under autothermal operation. To increase reaction yields above this limit, it is necessary to maintain reactor temperatures at a high level but at the same time decrease or at best eliminate the total oxidation zone at the catalyst entrance. This apparently contradictory requirement can be met by integrating the sensible heat of the product gases in a multifunctional reactor concept. In this way, it is possible to increase catalyst temperatures based on the only mildly exothermic partial oxidation reaction. The efficient heat-integration in a reverse-flow reactor (RFR) [22] makes this configuration a particularly interesting concept for CPOM.

### 2.2.1 Multifunctional Reactor Concept: The Reverse-Flow Reactor

The improvement of reactor performance by integrating several unit operations into a single reactor vessel has distinct advantages over the conventional sequential arrangement such as higher efficiency and lower cost. These so-called multifunctional reactor concepts have been the subject of intense research in the last two decades [28]. Common additional process functions are hereby for example integrated heat-exchange as well as selective addition of reactants or removal of product gas [19] (e.g. via selective membranes). Process enhancements are usually achieved by improvement of temperature and/or concentration profiles along the reactor axis. As pointed out by Agar [18], however, multifunctionality is typically restricted to one further process function in addition to the chemical reaction, and the development of truly multifunctional concepts is still in its early stages. A recent development in multifunctional reactor concepts is the analysis of the performance of autothermal coupling of exo- and endothermic reactions [28-32].

A frequently used multifunctional reactor concept incorporates the integration of heat released by an exothermic reaction either by recuperative heat-exchange in a countercurrent heat-

exchange reactor or by regenerative heat-exchange in a reverse-flow reactor (RFR). The highly efficient heat-integration in the RFR makes this a particularly suitable reactor configuration for weakly exothermic reactions.

The classical application of a dynamic RFR is closely related to the phenomenon of a moving reaction front. In a weakly exothermic reaction, the heat released might not be sufficient to keep the reaction ignited so that the reaction front moves along the catalyst bed. The front part of the catalyst bed acts as a regenerative heat-exchanger and increases the cold feed gas temperature while the reaction front creeps towards the exit of the reactor. To prevent the reaction from extinguishing once the reaction front reaches the outlet of the reactor, the flow through the reaction tube is reversed, and the reaction front wanders in the opposite direction.

Pioneering work concerning reverse-flow reactor operation has been performed by Matros and coworkers [2, 22, 33], which resulted in the industrial implementation of this technique for SO<sub>2</sub> oxidation [2]. Further large-scale applications of this reactor concept have been primarily realized for the incineration of waste gases [21, 34, 35]. Several studies have been performed on the production of sulfur in the Claus process [18, 36], the production of HCN [18, 37] as well as methane reforming [18].

### 2.2.2 Regenerative Heat-Exchange

The main advantage of an RFR compared to a conventional steady-state reactor is the intense, regenerative heat-exchange. Inert packing materials, so called inert zones, are placed on either side of the reaction zone and act as regenerative heat-exchangers in addition to the catalyst bed. Figure 2 shows a schematic of the temperature profile along the reactor axis in the RFR under operating conditions. Cold reactants enter the catalyst bed and react exothermically on the catalyst surface. Hot product gases exit the reaction zone and exchange heat with the inert zone downstream of the catalyst (Figure 2, 1.,  $t = 0$ ), which is therefore heated. The gas flow through the reaction tube is reversed, and cold reactants entering the reactor are heated up by the hot inert zone, which is now located upstream of the catalyst. The reactants enter the catalyst bed at an elevated temperature, which adds to the heat of reaction and leads to an overall increase of the

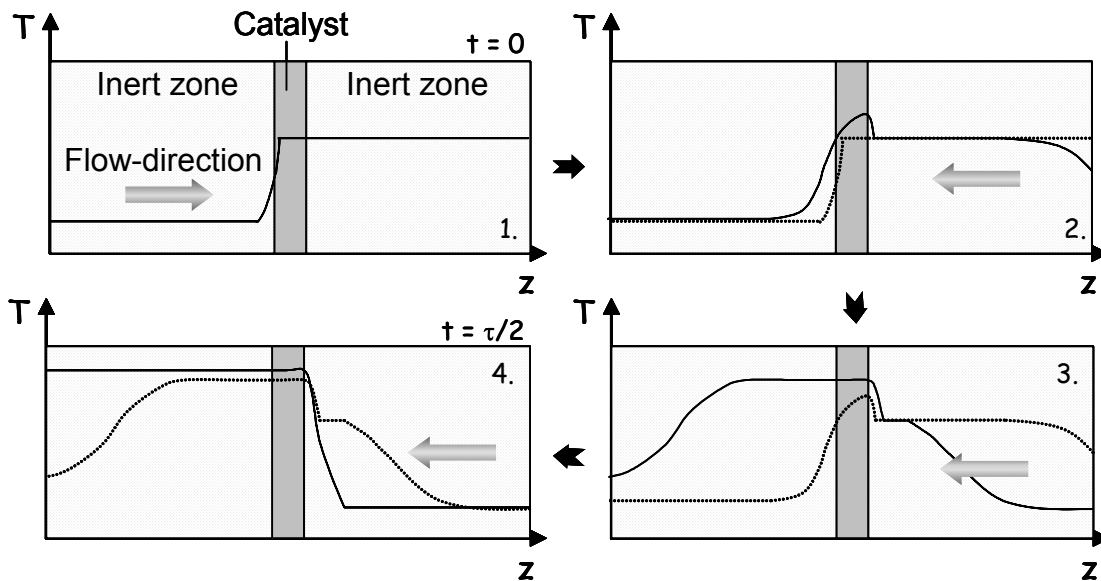


**Figure 2:** Schematic of regenerative heat-exchange in an RFR: Temperature profiles along the reactor axis  $z$  during one semi-cycle

catalyst temperature (Figure 2, 2., previous temperature profiles are represented by the dashed line, current ones by the solid lines). Hot product gases exit the reaction zone and exchange heat with the cold inert zone downstream of the catalyst bed. The continuous heat-exchange now leads to a cooling of the heat-reservoir upstream and a heating of the heat-reservoir downstream of the catalyst (Figure 2, 3.- 4.).

To prevent the catalyst temperature from dropping once the inert zone upstream of the catalyst has been cooled down, the flow is reversed periodically (with  $t = \tau/2$ ), resulting in a very efficient heat-integration.

When the flow-reversals are repeated frequently enough, the characteristics (temperatures, concentration profiles) of a full cycle are identical to the preceding one and the system has reached the so-called periodic steady-state. Figure 3 schematically shows average temperatures of a full cycle under periodic steady-state conditions along the reactor axis. It is a very beneficial temperature profile, because heat is concentrated in the region of the catalyst bed while the reactor ends remain cold, which facilitates the handling of the gases as well as the sealing of the reactor.

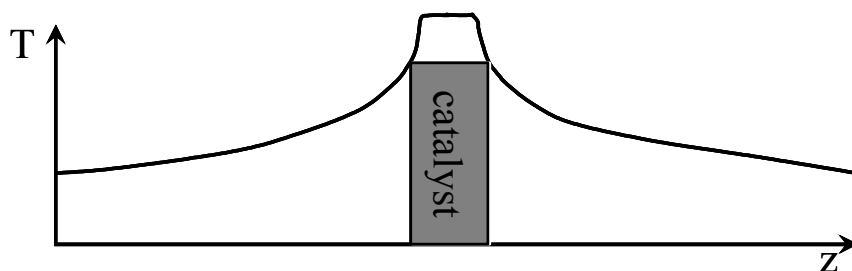


**Figure 3:** Schematic of mean temperatures along the reactor axis  $z$  of a full cycle in periodic steady-state

In a perfectly adiabatic reactor, heat-integration theoretically leads to infinitely high temperatures even for weakly exothermic reactions. However, particularly in small-scale reactors, inevitable heat losses to the environment limit maximum temperatures.

### 2.2.3 Surface Dynamics

In addition to regenerative heat-exchange, dynamic reactor operation leads to transient surface coverages by a temporal distribution of the feed gas. The flow-reversal results in an inversion of surface coverages with regard to the direction of the gas flow. As explained in chapter 2.2, steady-state operation is characterized by a predominantly oxygen covered surface at the catalyst entrance (leading to total oxidation) which is followed by a broad carbon coverage (leading to partial oxidation), see Figure 4, 1. Due to flow-reversal, the surface coverages are inverted with respect to the flow direction. Therefore, the dominant carbon coverage is positioned at the catalyst entrance, and the oxygen rich coverage is positioned at the catalyst exit (Figure 4, 2.). With time progressing, the surface coverages are adjusted to the original steady-state profiles. In this transient condition, a state is reached where carbon is the main surface species over the complete catalyst (Figure 4, 3.), before oxygen is again built up at the catalyst entrance (Figure 4, 4.). By carefully adjusting the cycling period, it should generally be possible to stabilize these transient conditions and tailor the coverages in such a way that dominant oxygen coverage at the

catalyst entrance (leading to total oxidation) is minimized, ‘kinetically’ reducing the amount of total oxidation of methane and increasing syngas yields.

Due to fast reaction rates observed in CPOM, it can be expected that the time-frame in which surface coverages are in a transient state is much shorter than the time-frame necessary for efficient regenerative heat-exchange. Global improvements in syngas yields due to this kinetic effect through periodic flow-reversal should thus only be minor. However, transient surface coverages can also be obtained through reactant feed cycling (e.g. pulsing of oxygen). If it can therefore be shown that syngas yields can in principle be improved by transient surface coverages, the overall process could further be optimized by superimposing reactant feed cycling onto the switching of flow-direction.

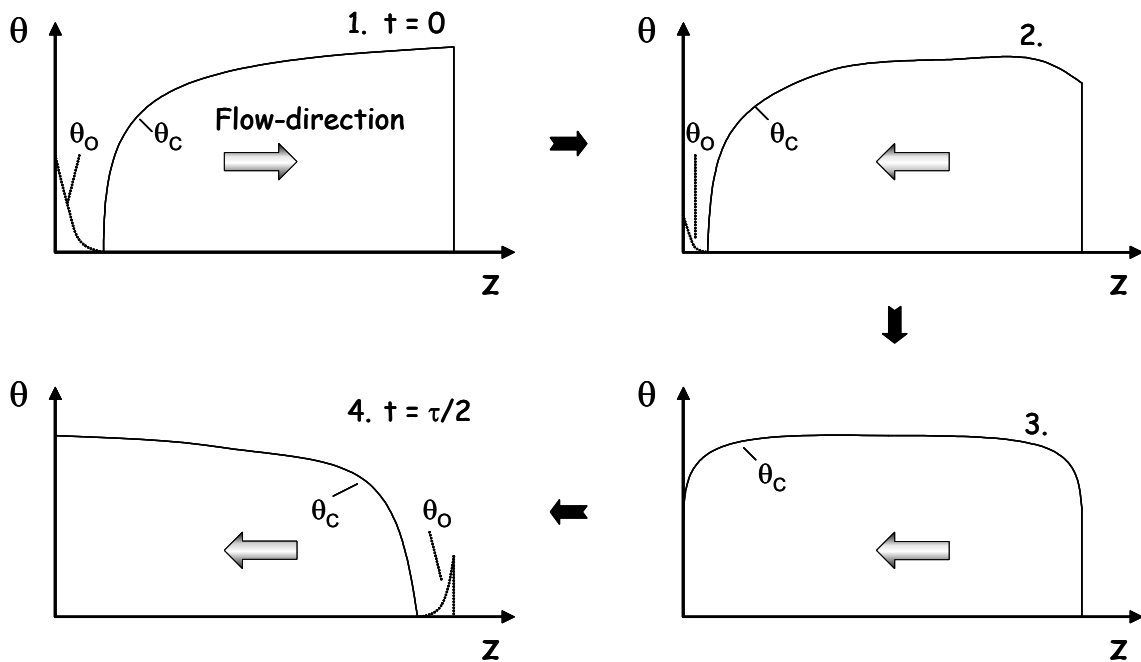


**Figure 4:** Schematic of catalyst surface coverages ( $\theta_0$ : dashed line,  $\theta_c$ : solid line) during a semi-cycle

#### 2.2.4 Literature on CPOM in an RFR

To date, only one experimental study investigating CPOM in an RFR has been published. Blanks et al. [38] investigated the conversion of natural gas with air in an adiabatic pilot-plant scale reactor using a Ni on alumina methane reforming catalyst. The reaction was characterized by relatively long residence times of 0.25 s and cycling periods of around 1 h. Excessively high temperatures in the inert zones led to the onset of homogeneous reactions in the heat-reservoir. The problem was controlled by pre-burning (combusting) some of the natural gas before feeding it to the reactor. In this way, endothermic reforming reactions occurring in parallel with total oxidation of methane at the catalyst front edge resulted in decreasing temperatures and a better control of the process. Furthermore, the authors faced problems due to carbon depositions in the inert zones, which were removed by bursting steam through the reactor for several minutes after every semi-cycle. Syngas selectivities ( $S_{H_2}$ : 80-85 %,  $S_{CO}$ : 86-92 %) and methane conversions ( $X_{CH_4}$ : 85-97 %) were reported for only one specific run in excess nitrogen.

Several simulation studies regarding CPOM in an RFR were performed. De Groote and Froment [39] modeled catalytic partial oxidation and autothermal reforming of natural gas over a Ni catalyst in an industrial scale reactor. They used a 1D heterogeneous model accounting for interfacial and intraparticle gradients and investigated the influence of several operating conditions ( $\tau/2$ , interstitial velocity, reactor length and feed gas temperature) on reactor performance. The kinetic equations they used to describe the reaction were global kinetics consisting of total oxidation of methane as well as reforming and water gas shift reactions. They investigated catalytic partial oxidation of methane with oxygen as well as air. CPOM with oxygen led to excessively high temperatures, which could only be lowered to an acceptable level by addition of large amounts of steam and high  $CH_4/O_2$  ratios. This in return resulted in low conversions and selectivities and shifted the product-gas  $H_2/CO$  ratio up to high values of 5. Catalytic partial oxidation of methane with air on the other hand led to high syngas selectivities above 90 % and methane conversions between 74-80 % at acceptable maximum temperatures. They furthermore investigated the role of carbon formation on the catalyst surface and concluded that coke formation is not excessive and can be avoided by appropriate operating conditions. Overall, they concluded that the large scale production of synthesis gas using Ni-catalysts in an RFR is feasible.

Gosiewski et al. [40] developed a mathematical model for the catalytic conversion of methane to syngas over a Pt catalyst. The kinetics were described with a set of four reaction rate equations: total oxidation of methane, methane reforming with H<sub>2</sub>O and CO<sub>2</sub> and the water gas shift reaction. They investigated the influence of intra-particle diffusion in the catalyst pellet on the rate of reaction and temperature profiles. They showed that due to the large temperature gradients in the reactor, diffusion limitations inside the catalyst pellet may not be omitted. They concluded that performing catalytic partial oxidation of methane with pure oxygen leads to excessively high temperature, which can be lowered by enlarging the pellet size or by adding water to the feed gas.

Gosiewski [41] then extended these studies using the same model and investigated reverse-flow reactors with pelletized and monolithic catalysts, as well as pelletized catalysts operating under cycling of the feed gas composition. The feed gas cycling consisted of a semi-cycle in which total combustion of methane predominantly takes place (low CH<sub>4</sub>/O<sub>2</sub> ratio of the feed gas), and a semi-cycle in which reforming reactions mainly occur (high CH<sub>4</sub>/O<sub>2</sub> ratios and the addition of steam or CO<sub>2</sub>). He furthermore added kinetic equations describing the formation and gasification of carbon deposits, as well as homogeneous combustion of methane to the model and investigated the reactor configurations with particular attention towards the deposition of coke on the catalyst. Gosiewski concluded that the RFR with catalyst pellets leads to the accumulation of a heat-wave and results in unacceptably high temperatures. The temperatures may be lowered by addition of steam to the feed gas, but at the expense of methane conversion. The monolithic RFR resulted in low maximum temperatures and no coke formation if monolith parameters were chosen carefully. However, a stationary monolith reactor reached only slightly higher maximum temperatures (the inlet temperatures chosen were 673 K compared to 473 in case of reverse-flow operation) and better conditions for carbon gasification at higher syngas yields. According to Gosiewski, the realization of a monolithic RFR should therefore not only be preceded by an economic analysis but also an experimental investigation. Finally, superimposing cycling of the feed gas composition onto a pelletized catalyst bed led to very high syngas yields and in addition to good conditions for carbon gasification, which would be the major advantage compared to a stationary process.

All these simulation studies have in common that the authors investigated CPOM in an industrial scale adiabatic reactor. Furthermore, the authors used reaction rate equations

consisting of total oxidation of methane, as well as reforming reactions and water-gas shift reaction, thus assuming an indirect partial oxidation mechanism. The heat-integration in the RFR combined with primary combustion of methane inevitably led to the accumulation of a heat-wave which resulted in unacceptably high temperatures. These could only be lowered by addition of water and/or CO<sub>2</sub> to the feed gas to enhance endothermic reforming reactions. The assumption of global reaction equations (which in none of the cases included a *direct* oxidation path for partial oxidation reaction) has a decisive influence on maximum temperature and temperature profiles in the catalyst bed.

### 2.3 Thermodynamics

CPOM is characterized by a complex interaction between partial and total oxidation reactions. High temperatures thermodynamically favor partial oxidation, while low temperatures favor total oxidation of methane. However, total oxidation of methane is an extremely exothermic reaction ( $\Delta H_r = - 800$  kJ/mol) and thus results in high temperatures (where the reaction equilibrium is shifted towards partial oxidation), whereas partial oxidation is only mildly exothermic ( $\Delta H_r = - 37$  kJ/mol) and results in lower temperatures. Overall, this interplay effectively limits obtainable syngas yields under autothermal operation. To quantify these limitations, thermodynamic calculations are performed.

Thermodynamic equilibrium compositions at different CH<sub>4</sub>/O<sub>2</sub> ratios and temperatures for a methane/air mixture presented in the following are calculated using standard thermo-physical properties of gases [42, 43]. Details of the procedure used for calculating thermodynamic temperatures and yields are listed in Appendix A (page 99).

Figure 5 shows syngas selectivities as well as methane conversions as a function of the CH<sub>4</sub>/O<sub>2</sub> ratio for a methane/air mixture. Data points labeled ‘adiabatic’ represent thermodynamic equilibrium yields at the respective adiabatic temperature (shown in Figure 6) of the methane/air mixture. Data points labeled ‘optimum’ represent equilibrium selectivities and conversions at temperatures where maximum syngas yields are achieved. Respective optimum temperatures are shown in Figure 6.



At adiabatic conditions, CO selectivities ( $S_{CO}$ ) exhibit a maximum of 86 % at a  $CH_4/O_2$  ratio of 1.5.  $H_2$  selectivities ( $S_{H_2}$ ) reach a value of about 92 % at  $CH_4/O_2$  ratios greater than 1.7 with a strong decrease towards smaller  $CH_4/O_2$  ratios.  $CH_4$  conversions ( $X_{CH_4}$ ) increase continuously with decreasing  $CH_4/O_2$  ratios and reach 100 % at a  $CH_4/O_2$  ratio of 1.4.

Figure 5 shows that at optimum temperatures and a  $CH_4/O_2$  ratio of 2.0, complete methane conversions and ideal partial oxidation selectivities can be achieved in thermodynamic equilibrium. Decreasing the  $CH_4/O_2$  ratio below 2.0 results in a decrease of syngas selectivities (since a stoichiometric surplus of oxygen is available to the reaction which results in total oxidation of some of the methane), while an increase of the  $CH_4/O_2$  ratio above 2.0 results in decreasing methane conversions (since lack of oxygen is limiting the overall conversion).

Clearly, autothermal (adiabatic) conditions limit syngas yields which can generally reach ideal values (close to 100 %) at sufficiently high temperatures. Adiabatic conditions reduce  $S_{CO}$  by about 15 %,  $S_{H_2}$  by about 10 % and  $X_{CH_4}$  by about 20 % compared to yields at optimum temperatures.

Figure 6 shows the corresponding temperatures. Assuming a feed temperature of 25°C, the adiabatic temperature increases continuously from 600°C at a  $CH_4/O_2$  ratio of 2.8 to about 1250°C at a  $CH_4/O_2$  ratio of 1.0. Optimum temperatures for maximum  $S_{CO}$  increase from 760°C at a  $CH_4/O_2$  ratio of 2.8 to above 1300°C at a  $CH_4/O_2$  ratio of 1.6. Optimum temperatures for  $S_{H_2}$  and  $X_{CH_4}$  exhibit a maximum at a  $CH_4/O_2$  ratio of 2.0 (927 and 1027°C, respectively). To reach optimum temperatures, a temperature increase above adiabatic limits is thus required. Figure 6 indicates that temperatures around 1050°C are necessary to achieve optimum syngas yields.

The interaction between dominant partial oxidation of methane at high temperatures and total oxidation of methane at low temperatures as well as the mild exothermicity of partial and strong exothermicity of total oxidation reactions thus results in a distinct limitation in syngas yields under autothermal (adiabatic) conditions.

While these thermodynamic calculations neglect the influence of reaction kinetics on syngas yields, they can nevertheless serve as a guideline. They clearly indicate that temperatures in excess of adiabatic temperatures are beneficial for syngas yields, and hence heat-integration should lead to process improvements. A more detailed discussion of the interaction between kinetics and thermodynamics in CPOM is performed in chapter 3.3.

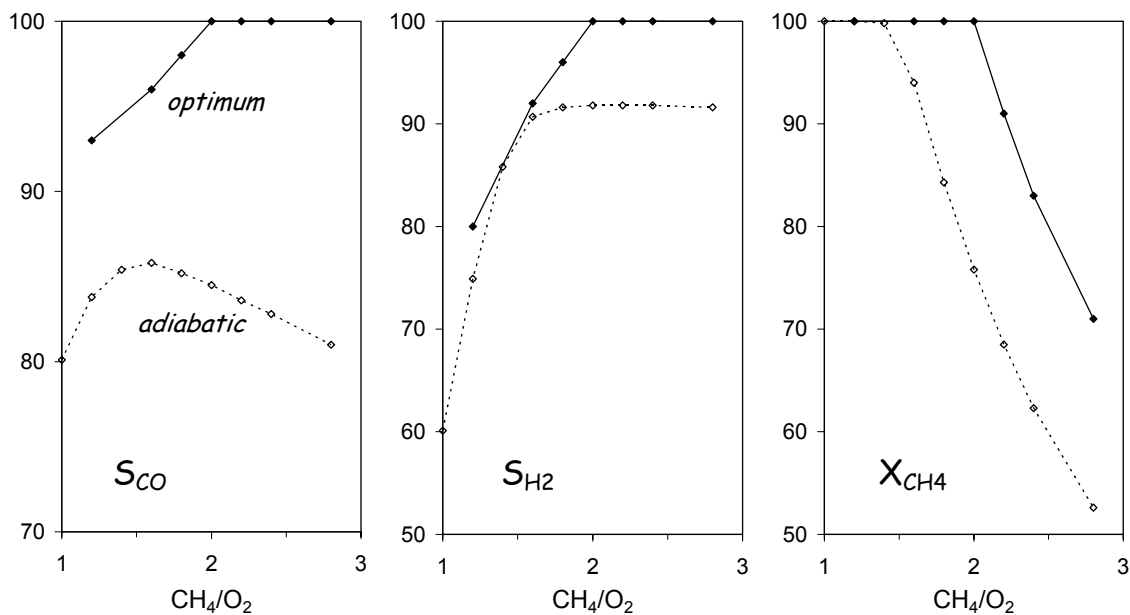


**Figure 5:** Thermodynamic calculations: adiabatic (dashed lines) as well as optimum (solid lines) selectivities towards CO (left),  $\text{H}_2$  (middle) and  $\text{CH}_4$  conversions (right) as a function of the  $\text{CH}_4/\text{O}_2$  ratio in a  $\text{CH}_4/\text{air}$  mixture

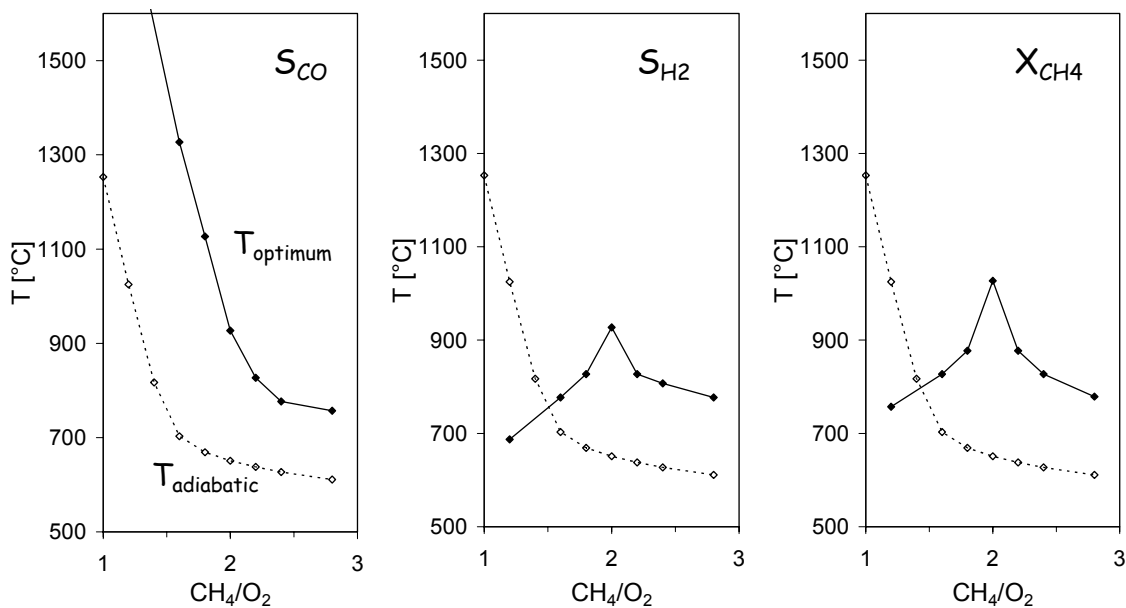


**Figure 6:** Thermodynamic calculations: adiabatic (dashed lines) and optimum (solid lines) temperatures necessary to achieve maximum  $S_{\text{CO}}$  (left),  $S_{\text{H}_2}$  (middle) and  $X_{\text{CH}_4}$  (right)

### 3.0 EXPERIMENTS

#### 3.1 Experimental Setup

Figure 7 shows a schematic of the experimentally used RFR system. It consists of a plug-flow reactor and four valves which are used to direct the gas flow through the reaction tube. The product gases are analyzed with a mass-spectrometer (MS) as well as a gas-chromatograph (GC).

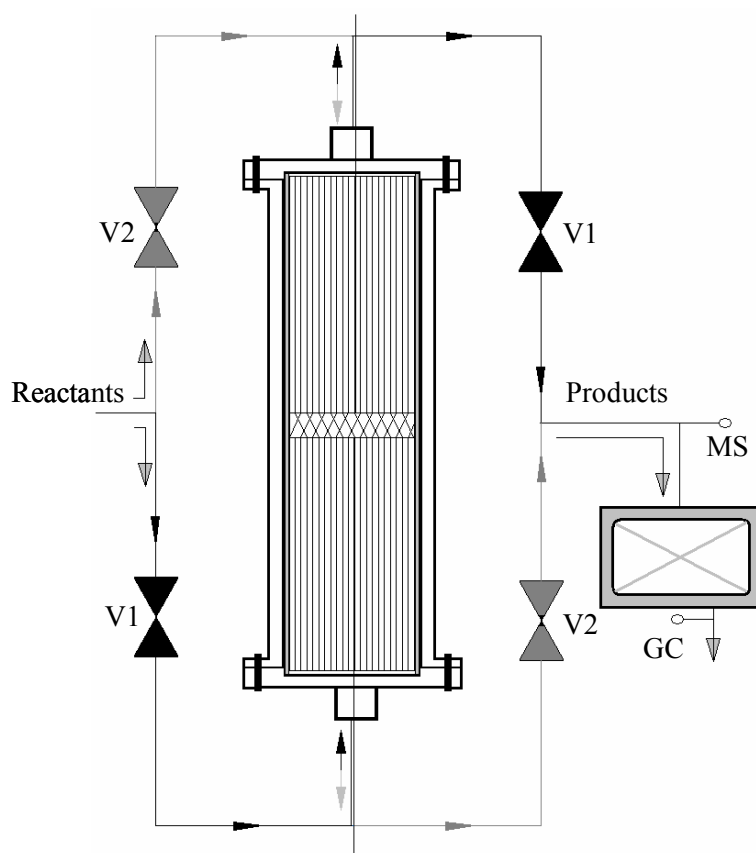


**Figure 7:** Schematic of the RFR system

The reactor design is based on knowledge gained from performing steady-state experiments in a quartz-glass tube as well as a counter-current heat exchange reactor [20]. These preceding investigations revealed that standard steel cannot be used as a reactor wall material since it does not withstand the excessive temperatures during reactor operation, and high-temperature steel becomes catalytically active, degrading the reactor and reaction yields. Therefore, the high temperature section of the reactor has to consist of an inert material like quartz-glass or ceramic. At the same time, the integration of the reaction tube into the RFR system necessitates a mechanically stable connection. Several reactor configurations had to be tested until these guidelines were adequately met.

A first reactor consisted of a quartz-tube which was glued to metal caps using ceramic paste. This proved to be inefficient since thermal and mechanical stresses resulted in the breakage of the glass at the glass-metal interface. In a second reactor design, a quartz-tube was inserted into a metal housing without any sealing between the glass and the metal. While no breakage occurred during reactor operation, heat losses to the metal housing were unacceptably high and resulted in low reaction yields. A solution to these difficulties was found in the construction of a quartz-metal hybrid reactor (Figure 8). It consists of a high-temperature resistant quartz-tube (1.8 cm i.d., 2.2 cm o.d., 24.0 cm long) into which the catalyst and the inert zones (diameter  $\sim$ 1.7 cm) are inserted. The monoliths themselves are rolled in alumina paper (0.3 mm thick) to avoid a bypass between the ceramic and the quartz-tube. The glass-tube is then wrapped in several layers of alumina cloth and inserted into a steel-tube housing (2.7 cm i.d., 3.0 cm o.d.). At either end of the quartz tube, alumina paper is pressed between the metal and the glass to prevent any gases from bypassing the inner tube by flowing through the outer shell (between the glass and the metal). Finally, the steel housing is embedded into an insulation cloth to minimize heat losses.

The catalysts used in the experiments are Pt-coated alumina foam monoliths (1.7 cm diameter, 1.0 cm long, 45 ppi [= pores per linear inch], Figure 8), which are prepared by standard impregnation and calcination procedures, yielding  $\sim$ 5-6 wt % Pt. While Rh catalysts are more selective, using less selective Pt catalysts has the advantage of making any improvements in syngas yields due to the reactor configuration more apparent. Detailed instructions on the catalyst preparation are listed in Appendix B (page 100). Even though these procedures were followed precisely, different catalysts exhibited differences in catalytic activity, which resulted

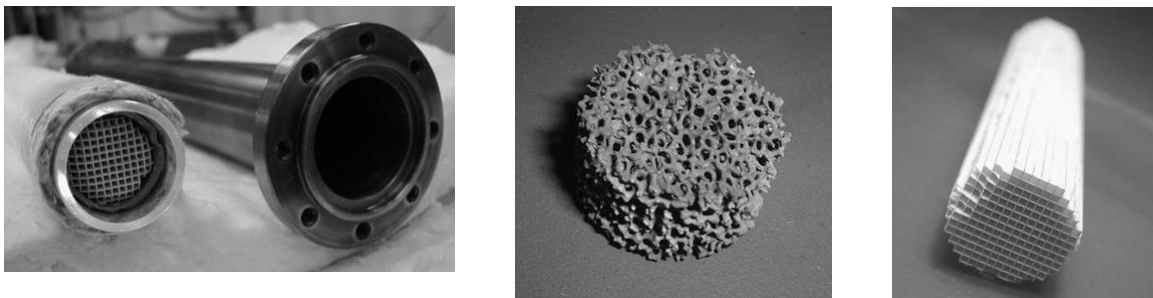


**Figure 8:** *Quartz-metal hybrid reactor (left), foam monolith (middle) and extruded monolith (right)*

in different syngas yields under the same operating conditions (up to 5 % in  $S_{CO}$  and 5-10 % in  $S_{H_2}$  and  $X_{CH_4}$ ). Possible reasons might be differences in the geometries of the alumina supports, e.g. pore size distributions or specific surface areas, and a non homogeneous distribution of the Pt-coating. Nevertheless, most of the experiments performed compared RFR with steady-state conventional reactor operation using the same catalyst, so that differences between different catalysts are not critical. For all other cases, problems related to comparing different catalysts are discussed in the corresponding chapter.

Inert materials (so called inert zones, cordierite extruded monoliths; 1.7 cm diameter, 11.0 cm long, 350 cpi [= cells per square inch], Figure 8) are placed before and after the catalyst bed to act as radiation shields as well as solid-state heat-reservoirs for the regenerative heat exchange in dynamic reactor operation. Although cordierite has a low density and low heat-capacity which reduces the capability of accumulating large amounts of heat, it is used due to its ready availability and inertness.

Temperatures are measured with type K (Ni/CrNi) thermocouples on either side of the catalyst bed. Both thermocouples are moveable and hence allow the measurement of temperature profiles in the (extruded) inert zones along the reactor axis. However, due to the irregular foam structure of the catalyst support, it is not possible to measure temperature profiles inside the monolithic catalyst itself. There are mainly three sources of error related to the measurement of the temperatures. First, temperature measurements with thermocouples typically have a relative error of +/- 2.5 %. According to the manufacturer's data sheet, the readings are only accurate up to temperatures of about 1100-1200°C. Second, the exact location of the thermocouple tip is

unknown. It is consequently not obvious whether the gas or the solid phase temperature (or a mixture of both) is measured. Third, the average pore size of the 45 ppi foam monolith (commonly used in the experiments) is roughly 1 mm and larger than the diameter of the thermocouple (diameter about 0.1 mm). It is thus not known if, or to what extent, the thermocouple penetrates into the catalyst bed (this depends on the actual arrangement of extruded inert zone and the random channels of the foam monolith). Because very steep temperature profiles are observed at the catalyst entrance, this can lead to a large error. The frequency with which temperature measurements can be performed is restricted by the experimental setup and temperatures can only be measured approximately every 0.8 s.

The pressure is measured at the reactor inlet and outlet using pressure transmitters (Jumo 4AP-30). The pressure drop across the reactor length is dependent on the flow-rate but stays below 0.1 bar for all cases.

Flow of methane (4.0 grade, Valley National Gas) and air (0.1 grade, VNG) is controlled by standard mass flow controllers (MKS 1179A).

The switching of the flow direction through the reaction tube is accomplished with two sets of two magnetically operated valves (V1 and V2, Figure 7), which are positioned parallel in front of and behind the reactor. By keeping two diagonally positioned valves open while closing the remaining two, a flow of the gases through the reactor is achieved. Reversing the flow-direction is accomplished by closing the valves that are open and opening the ones that are closed.

To prevent water from condensing in the capillaries, the tubes leading away from the reactor are heated to above 100°C using heating tapes.

Product gases are analyzed using a mass spectrometer (Balzers Quadstar GSD 300) giving qualitative, time resolved measurements, and a double oven gas chromatographic system (Shimadzu GC-14B) for quantitative measurements. The GC determines the concentrations of the components CH<sub>4</sub>, O<sub>2</sub>, N<sub>2</sub>, H<sub>2</sub>, H<sub>2</sub>O, CO and CO<sub>2</sub>. Appendix C (page 101) lists details of the column configuration as well as oven and detector parameters. Atom balances for all atomic species close in a typical run to better than 2 %. Selectivities towards partial oxidation products as well as methane conversions are calculated using molar concentrations of the product gases and several different sets of key components. An example of how these calculations are performed is shown in Appendix D (page 104). Additionally, a vessel with a two liter volume can be connected in series before the GC. This ensures an appropriate mixing of non-stationary

product gases and allows for a simple and reliable quantitative measurement of mean component concentrations for a full cycle during dynamic reactor operation.

The switching of valves, temperature and pressure readings as well as data-processing is computer controlled (software LabView 6.i).

For a direct comparison of the results at reverse-flow operation with results from a conventional reactor, the same reactor setup is used for steady-state experiments by omitting the switching of flow-direction. In this way, it is assured that all differences between steady-state results and results at forced unsteady conditions are exclusively due to differences in reactor operation rather than differences in the experimental setup.

## 3.2 Experimental Results

### 3.2.1 Dynamic Reactor Operation

Dynamic reactor operation results in a non steady-state heat-integration. As a consequence, temperature and concentration profiles are time dependent and repeat periodically with the cycling time of flow-reversal  $\tau$ . After the initial start-up phase (the startup procedure for the reactor operation is listed in Appendix E, page 109), the so-called periodic steady-state has been reached once temperature and concentration profiles during a cycle are identical to the preceding and following cycle. An example for the approach of temperatures measured on either side of the catalyst bed (left graph) as well as  $H_2$ -concentrations measured at the outlet of the reactor (right) towards periodic steady-state conditions is shown in Figure 9.

During the initial 30 s, the reactor is operated at steady-state conditions and temperatures and concentrations remain constant. Then, periodic flow-reversal begins and flow-direction is switched every 15 s (i.e.  $\tau/2 = 15$  s). Characteristic temperature curves develop at the catalyst entrance and exit which will be discussed in more detail later.  $H_2$ -concentrations increase strongly in reverse-flow mode and show a time-dependent behavior as well.

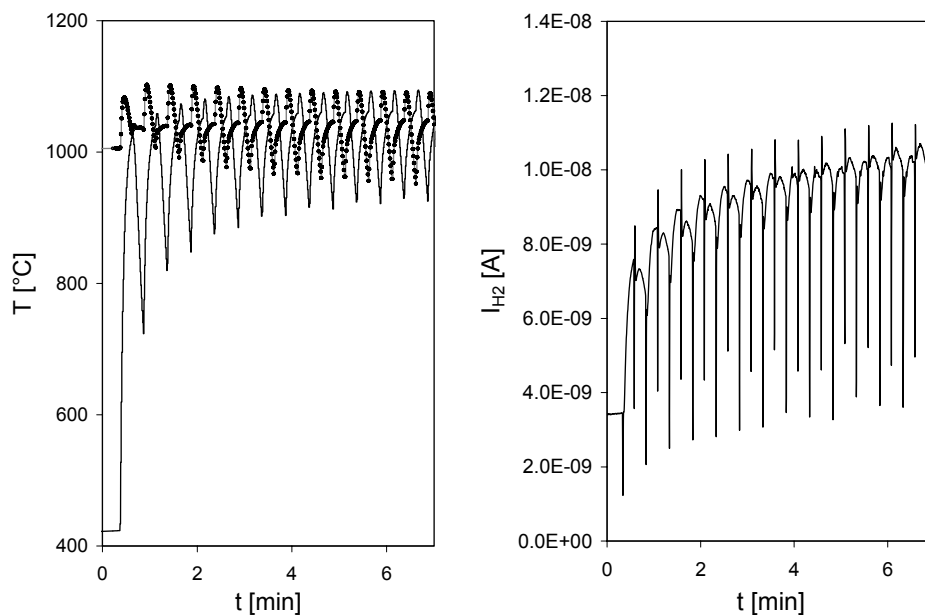


**Figure 9:** *Temperatures at the catalyst entrance and exit (left) as well as  $H_2$ -concentrations at the reactor exit (right) during initial 7 minutes of transition from steady-state to dynamic RFR operation*

Periodic steady-state conditions are usually reached within half an hour after reverse-flow mode has been initiated. In the following, some of the main characteristic properties measured in periodic steady-state of the RFR are presented.

Figure 10 shows the progression of temperatures measured at the catalyst entrance and exit during two semi-cycles at a flow-rate of 3 slm (standard liters per minute), a semi-cycling period of 15 s and a  $CH_4/O_2$  ratio of 2.0. The position of the catalyst entrance and exit is defined relative to the gas-flow, which changes direction through the reaction tube every semi-cycle. Stationary thermocouples positioned at either end of the catalyst bed therefore measure the entrance temperature during one half-period and the exit temperature during the next half-period (and vice-versa). The two semi-cycles shown in Figure 10 have been marked ‘1st’ and ‘2nd semi-cycle’ respectively. Solid squares represent catalyst entrance temperatures in the first semi-cycle, while hollow squares represent temperatures at the exit of the reaction zone. In the second semi-cycle, the relative positions switch and hollow squares display entrance temperatures while solid squares represent exit temperatures.



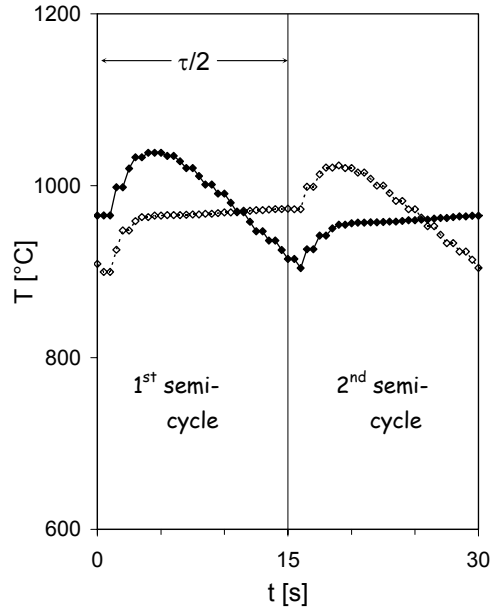


**Figure 10:** Time dependent temperatures measured on either side of the catalyst bed;  $CH_4/O_2 = 2.0$ ,  $\tau/2 = 15$  s,  $\dot{V} = 3$  slm

Catalyst entrance temperatures proceed through a maximum within the first couple of seconds after flow-reversal which is followed by a continuous decrease. Catalyst exit temperatures initially show a strong increase which flattens during the course of the semi-cycle. The offset time observed at the beginning of a semi-cycle occurs due to thermal inertia of the system as well as some time lag of the temperature reading due to the experimental setup.

The temperature curve at the catalyst entrance can be explained with dynamic heat-integration in the RFR. Temperatures are generally determined by the heat of reaction, the feed gas temperature, convective cooling as well as heat losses towards the surroundings. In periodic steady-state, the amount of heat accumulated in the inert zone downstream of the catalyst during one semi-cycle has a maximum value at the point of flow-reversal (end of semi-cycle). After flow-reversal, cold reactants entering the reactor are heated up by the heat-reservoir - which is now upstream of the reaction zone - prior to entering the catalyst bed. During the semi-cycle, the feed gas maintains a maximum temperature for a certain time which depends on the amount of heat accumulated in the inert zone as well as convective heat-transport of the reactants (which is mainly influenced by the flow-rate). The catalyst entrance temperature increases continuously

during this time, since feed gas is providing additional heat to the heat of reaction. Once the heat-reservoir is empty, the feed gas temperature drops and consequently results in a decrease of the catalyst entrance temperature. The slope of the decrease is directly dependent on the amount of heat accumulated in the heat-reservoir and therefore on the physical properties of the inert zone. If no further flow-reversal were to take place, the temperatures would eventually result in the temperatures of the steady-state process (once the inert zone upstream of the catalyst can no longer provide additional heat).

In contrast to catalyst entrance temperatures, exit temperatures are not as dependent on the heat-integration. A strong temperature rise within the first couple of seconds is followed by an almost constant temperature during the remaining part of the semi-cycle. Initially, the relatively cold monolith exit zone (which was the catalyst entrance in the preceding semi-cycle) is heated by hot effluent product gases and leads to the observed temperature increase. Thereafter, catalyst exit temperatures are essentially constant and are not influenced by varying catalyst entrance temperatures. This observation indicates that to some extent sensible heat is converted into chemical energy and results in an increase in syngas yields, since changing catalyst entrance temperatures do not have an effect on catalyst exit temperatures. This phenomenon will be discussed in more detail in chapter 3.3.2.

Time dependent product gas concentrations are measured qualitatively with an MS at the outlet of the RFR system. The location of the MS probe enables the measurement of the product gas stream independent of the flow-direction through the reactor (see Figure 7). Therefore, concentration curves repeat periodically with  $\tau/2$ . As an example, Figure 11 shows  $H_2$ ,  $H_2O$  and  $CH_4$  concentrations during 2 semi-cycles ( $\tau/2 = 15$  s,  $\dot{V} = 4$  slm,  $CH_4/O_2 = 2.6$ ).

The concentrations show a distinct spike immediately after every flow-reversal. Thereafter,  $H_2$  concentrations exhibit a broad convex curve while  $H_2O$  and  $CH_4$  concentrations show a broad concave curve.

The experimental procedure does not include a flushing phase with an inert gas before each semi-cycle. These phases are usually part of a technical RFR and prevent reactants from exiting the system after flow-reversal. This can be a very important aspect e.g. for downstream processes, where reactants of the first (RFR) process might poison the catalyst used in the following process. Furthermore, yield losses can be substantial if large reactor volumes are used.

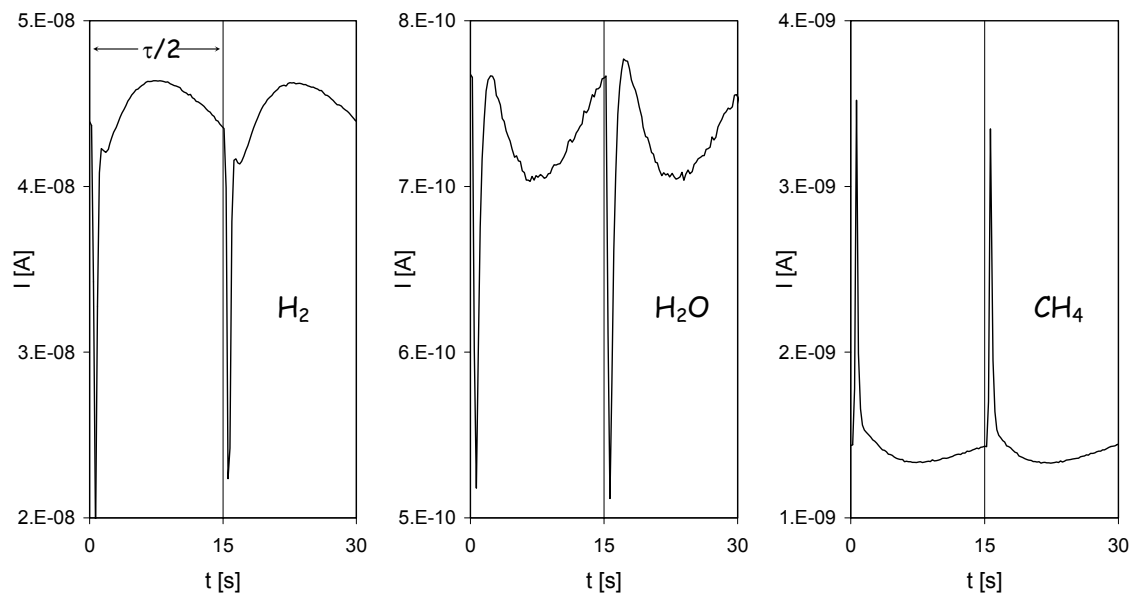


**Figure 11:**  $H_2$ - (left),  $H_2O$ - (middle) and  $CH_4$ - (right) concentrations during 2 semi-cycles ( $\tau/2 = 15$  s,  $\dot{V} = 4$  slm,  $CH_4/O_2 = 2.6$ );

However, in the investigated system, high throughputs and the compactness of the reactor result in a negligible effect on global yields. If nevertheless reactants have to be prevented from exiting the system (because they for example poison a catalyst of a downstream process), this could be realized through the installation of a heated Pt-gauze at the exit of the RFR system. Since catalyst contact times in high temperature CPOM are only in the order of several milliseconds, an adequate conversion of back-flushed reactants could be achieved in this additional reactor downstream of the RFR process and overall syngas yields further enhanced.

Since no flushing phase is implemented in the current setup, small amounts of reactants exit the system after every semi-cycle. This leads to the observed dip in product concentrations and peak in reactant concentrations after every semi-cycle as displayed in Figure 11. The progression of the concentration profiles following the dip is dependent on temperature profiles inside the catalyst bed, which cannot be measured experimentally due to the foam structure of the monolith. For a given set of reactor parameters, an optimum temperature profile seems to exist around eight seconds into the semi-cycle, where maximum  $H_2$  concentrations and minimum  $H_2O$  and  $CH_4$  concentrations are observed. A more in depth analysis of the influence of temperature

profiles onto reaction selectivities (i.e. the reaction mechanism) will be performed in the simulation part of this thesis (chapter 4.4).

In the following experimental sections, selectivities and methane conversions as well as temperatures will be shown as averages of a full cycle at periodic steady-state conditions. This facilitates the comparison between results obtained in the dynamic RFR with results from the conventional steady-state reactor.

### 3.2.2 Variation of the Feed Gas Composition

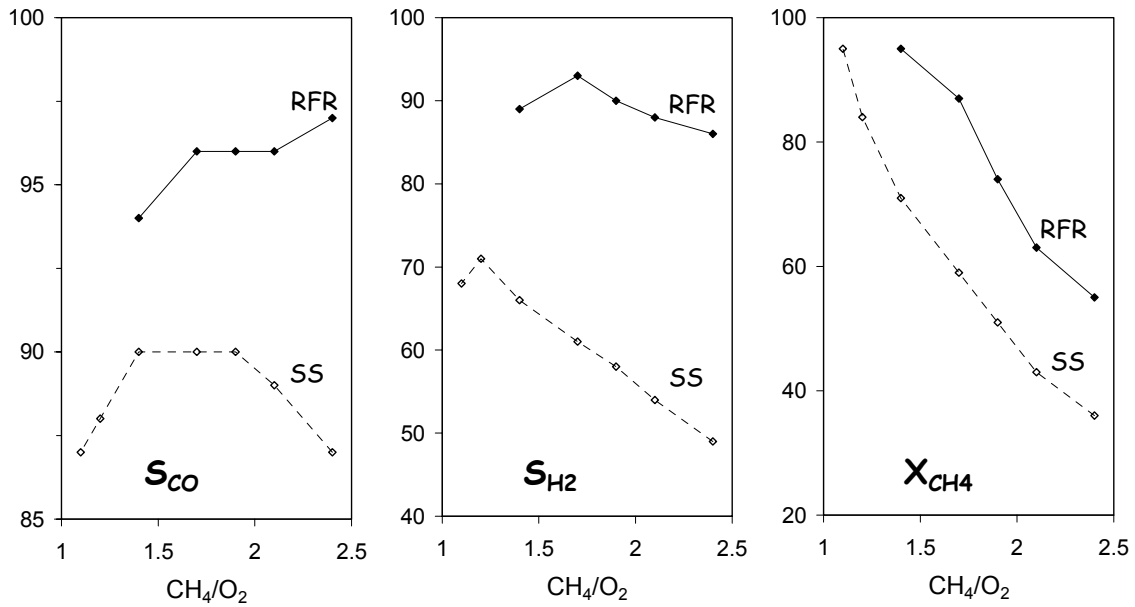
CPOM is characterized by a complex interaction between partial and total oxidation reactions. The stoichiometric point for partial oxidation is at a  $\text{CH}_4/\text{O}_2$  ratio of 2.0 and for total oxidation at 0.5. The  $\text{CH}_4/\text{O}_2$  ratio of the feed gas is therefore a decisive parameter for influencing reaction selectivities and is investigated in the following.

Figure 12 shows partial oxidation selectivities and methane conversions for different  $\text{CH}_4/\text{O}_2$  ratios in the RFR (at a constant flow rate  $\dot{V} = 4$  slm, semi-cycle period  $\tau/2 = 15$  s) and a comparison to conventional steady-state (SS) reactor operation. Oxygen conversions are always close to 100 % and are therefore not displayed.

CO selectivities exhibit a relatively constant value for all  $\text{CH}_4/\text{O}_2$  ratios (~90 % in the conventional process and 96 % in RFR operation).  $\text{H}_2$  selectivities show a maximum at a  $\text{CH}_4/\text{O}_2$  ratio of 1.2 ( $S_{\text{H}_2} = 71$  %) in steady-state operation and at a  $\text{CH}_4/\text{O}_2$  ratio of 1.7 ( $S_{\text{H}_2} = 93$  %) in the RFR. Methane conversions increase continuously with lower  $\text{CH}_4/\text{O}_2$  ratios (from 36 % at  $\text{CH}_4/\text{O}_2 = 2.4$  to 95 % at  $\text{CH}_4/\text{O}_2 = 1.1$  in the stationary process and 55 % at  $\text{CH}_4/\text{O}_2 = 2.4$  to 95 % at  $\text{CH}_4/\text{O}_2 = 1.4$  in RFR operation).

RFR operation results in a pronounced increase in syngas yields over the whole range of  $\text{CH}_4/\text{O}_2$  ratios investigated as well as a shift in maximum  $S_{\text{H}_2}$  towards higher  $\text{CH}_4/\text{O}_2$  ratios compared to the conventional process.

Figure 13 shows corresponding temperature measurements. Displayed RFR temperatures represent mean catalyst entrance and exit temperatures averaged over a full cycle as well as maximum temperatures (at the catalyst entrance and exit) during that cycle.



**Figure 12:**  $S_{CO}$  (left),  $S_{H_2}$  (middle) and  $X_{CH_4}$  (right) as a function of the  $CH_4/O_2$ -ratio for steady-state (SS, dotted lines) and RFR (solid lines) operation; ( $\dot{V} = 4 \text{ slm}$ ,  $\tau/2 = 15 \text{ s}$ )

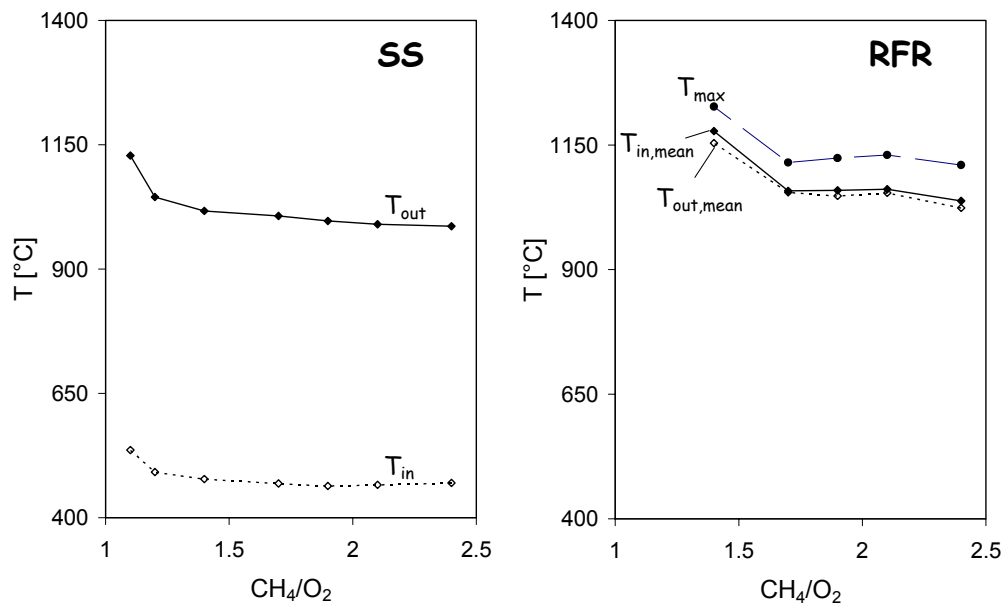


**Figure 13:** Temperatures as a function of the  $CH_4/O_2$ -ratio: steady-state (left) and RFR (right) operation;  $\dot{V} = 4 \text{ slm}$ ,  $\tau/2 = 15 \text{ s}$

Both the dynamic and the steady-state process exhibit almost constant temperatures over a broad range of  $\text{CH}_4/\text{O}_2$  ratios ( $\sim 500^\circ\text{C}$  at the catalyst entrance and  $\sim 1000^\circ\text{C}$  at the catalyst exit between  $1.2 < \text{CH}_4/\text{O}_2 < 2.4$  in steady-state;  $\sim 1050^\circ\text{C}$  mean catalyst entrance and exit as well as  $\sim 1120^\circ\text{C}$  maximum temperature between  $1.4 < \text{CH}_4/\text{O}_2 < 2.4$  in the RFR). A sharp increase in temperatures is observed at a  $\text{CH}_4/\text{O}_2$  ratio of 1.2 in the conventional process and at a  $\text{CH}_4/\text{O}_2$  ratio of 1.4 in the RFR.

The influence of the  $\text{CH}_4/\text{O}_2$  ratio on selectivity and conversion as well as temperature for the steady-state process was investigated by Vesper et al. [15]. Decreasing the  $\text{CH}_4/\text{O}_2$ -ratio below 2.0 has two opposing effects on the reaction mechanism: stoichiometrically, the highly exothermic combustion of methane is increasingly favored, which should thus result in decreasing syngas selectivities and increasing temperatures. However, increasing temperatures shift the reaction equilibrium towards the less exothermic partial oxidation of methane. As a consequence, temperatures remain constant over a broad range of  $\text{CH}_4/\text{O}_2$  ratios while maximum syngas selectivities are observed at  $\text{CH}_4/\text{O}_2$  ratios smaller than the stoichiometric point of 2.0. The shift in maximum attainable syngas yields towards lower  $\text{CH}_4/\text{O}_2$  ratios thus reflects the fact that the reactor operates under non-optimal conditions. In the RFR, maximum  $\text{H}_2$  selectivities are shifted towards higher  $\text{CH}_4/\text{O}_2$  ratios compared to the steady-state process (Figure 12), which is therefore an indication of improved process efficiency.

The integrated heat-exchange in the RFR process results in increased catalyst temperatures when compared to the process without heat-integration, as can be seen from higher temperatures in Figure 13. This temperature increase is particularly pronounced at the catalyst front edge, where mean temperatures of the dynamic reactor are about twice as high as the ones measured under steady-state conditions.

Syngas yields are limited in autothermal CPOM due to a complex interaction between total and partial oxidation reactions. High temperatures which are thermodynamically necessary to push reaction selectivities towards the partial oxidation products only occur due to combustion of some of the methane feed, reducing obtainable syngas yields. In the RFR on the other hand, high catalyst temperatures are achieved due to very efficient regenerative heat-exchange. High feed gas temperatures effectively reduce total oxidation of methane at the catalyst entrance and result in the observed pronounced increase in syngas yields in dynamic reactor operation.

### 3.2.3 Variation of the Cycling Period

The semi-cycling period  $\tau/2$  is a unique operating parameter of the dynamic reverse-flow reactor. It sets the time frame in which heat is stored and removed in the inert zones on both sides of the catalyst bed and thus has a decisive influence on temperature profiles along the reactor axis. Two limiting cases can be distinguished: a)  $\tau/2 \rightarrow \infty$ , which reflects the transition to the steady-state conventional process without heat-integration, and b)  $\tau/2 \rightarrow 0$ , where the gas-flow stagnates and the reaction extinguishes. One can expect that an optimum cycling time exists between these two extremes. This was tested experimentally by measuring syngas yields as a function of the cycling period. Results for a flow-rate of 4 slm and a  $\text{CH}_4/\text{O}_2$  ratio of 2.0 are shown in Figure 14.

Methane conversions and partial oxidation selectivities (left graph) show a maximum at a semi-cycling period of about 10 s while mean catalyst temperatures (right graph) show a

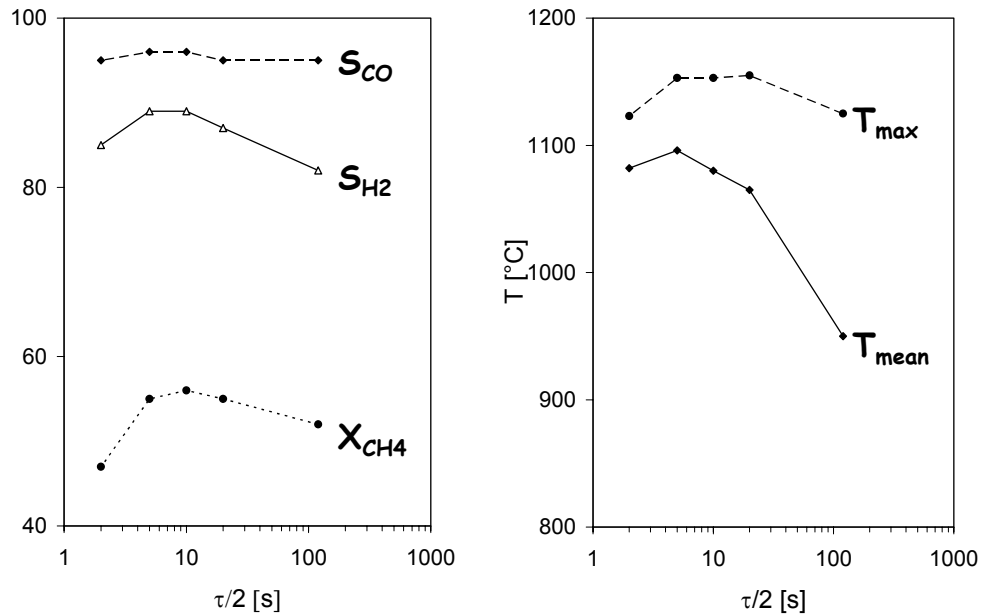


**Figure 14:**  $S_{\text{CO}}$  (dashed line),  $S_{\text{H}_2}$  (solid line) and  $X_{\text{CH}_4}$  (dotted line, left) as well as maximum and mean temperatures (right) as a function of the cycling period  $\tau/2$  ( $\dot{V} = 4$  slm,  $\text{CH}_4/\text{O}_2 = 2.0$ )

maximum at  $\tau/2 = 5\text{-}10$  s ( $T = 1100^\circ\text{C}$ ). Maximum temperatures show a broad maximum around  $\tau/2 = 10$  s and vary only within  $30^\circ\text{C}$  over the  $\tau/2$ -range investigated ( $T = 1120\text{-}1150^\circ\text{C}$ ).

At a flow-rate of 4 slm, optimal heat-integration thus occurs at a cycling period  $\tau/2 \approx 10$  s, as reflected in maximum syngas yields and mean reactor temperatures. Compared to large-scale industrial processes, where cycling times are usually in the range of minutes to hours, they are very short. High throughputs attainable in high temperature catalytic reactions result in high convective heat-transport and therefore lead to a fast cooling of the heat-reservoir. Furthermore, low thermal capacity and density of the cordierite inert zones prevents accumulation of large amounts of heat. While cordierite extruded monoliths were used as heat-reservoirs due to their ready availability, replacement of cordierite with e.g. alumina (higher heat-capacity) extruded monolith is hence a possibility to optimize the process.

The cycling frequency allows to optimize reactor operation with respect to syngas yields. At the same time, maximum temperatures stay within a narrow range. This is particularly important regarding catalyst activity (chapter 3.2.7) and overall reactor stability, which decrease faster at higher temperatures.

### 3.2.4 Variation of the Flow-Rate

One of the major advantages in high temperature catalysis is the very high reaction rates which allow for short catalyst contact times. Therefore, high space-time yields are attainable in very compact reactors. The influence of space-time on reactor performance was investigated by measuring syngas yields as a function of the flow-rate.

Figure 15 shows methane conversions and syngas selectivities at different flow-rates  $\dot{V}$  (1-5 slm, upper limit set by range of mass flow controllers) at a constant  $\text{CH}_4/\text{O}_2$ -ratio of 2.0 and a semi-cycling period  $\tau/2$  of 15 s for the RFR and the steady-state (SS) process. Again, dynamic reactor operation leads to a pronounced increase in syngas yields compared to conventional reactor operation (except at 1 slm for  $S_{\text{CO}}$  and  $X_{\text{CH}_4}$ , which are about 5 % and 2 % lower in the RFR than in the steady-state process, respectively). Furthermore, while the steady-state process exhibits maximum syngas yields at a flow-rate of 3 slm ( $S_{\text{CO}} = 92$  %,  $S_{\text{H}_2} = 70$  %,  $X_{\text{CH}_4} = 59$  %),



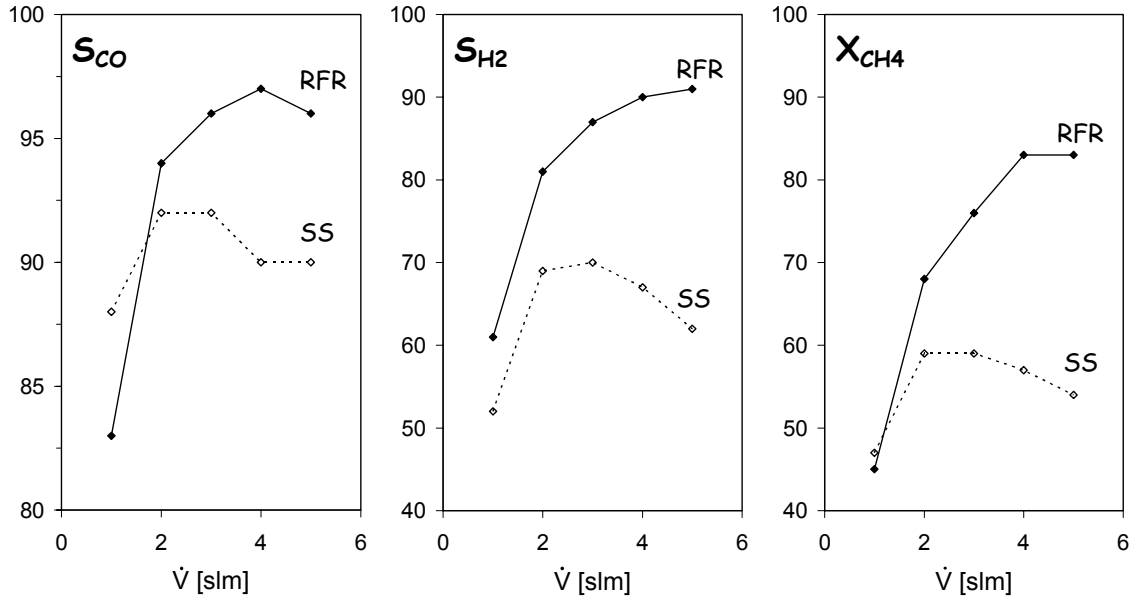


**Figure 15:**  $S_{CO}$  (left),  $S_{H_2}$  (middle) and  $X_{CH_4}$  (right) as a function of the flow-rate for steady-state (SS, dotted lines) and RFR (solid lines) operation;  $CH_4/O_2 = 2.0$ ,  $\tau/2 = 15$  s

partial oxidation selectivities as well as methane conversions increase continuously in the RFR with higher flow-rates (from  $S_{CO} = 83$  %,  $S_{H_2} = 61$  %,  $X_{CH_4} = 45$  % at 1 slm to  $S_{CO} = 96$  %,  $S_{H_2} = 91$  %,  $X_{CH_4} = 83$  % at 5 slm). Apparently, maximum attainable syngas yields are shifted towards even higher flow-rates and hence even shorter contact-times in the RFR.

This behavior can be understood with changes in catalyst entrance and exit temperatures at varying flow-rates as shown in Figure 16. In the conventional process, increasing the throughput results in increasing catalyst exit and decreasing catalyst entrance temperatures. In RFR operation, however, mean catalyst entrance and exit as well as maximum temperatures increase continuously with higher flow-rates and run parallel to catalyst exit temperatures of the steady-state process.

Increasing the flow-rate in the conventional process has two opposing effects on temperature profiles and therefore reaction selectivities: On one hand, it leads to an increase of heat generated by the reaction since more reactants are converted per unit time. This results in elevated catalyst temperatures - as can generally be seen from increasing catalyst exit temperature with higher

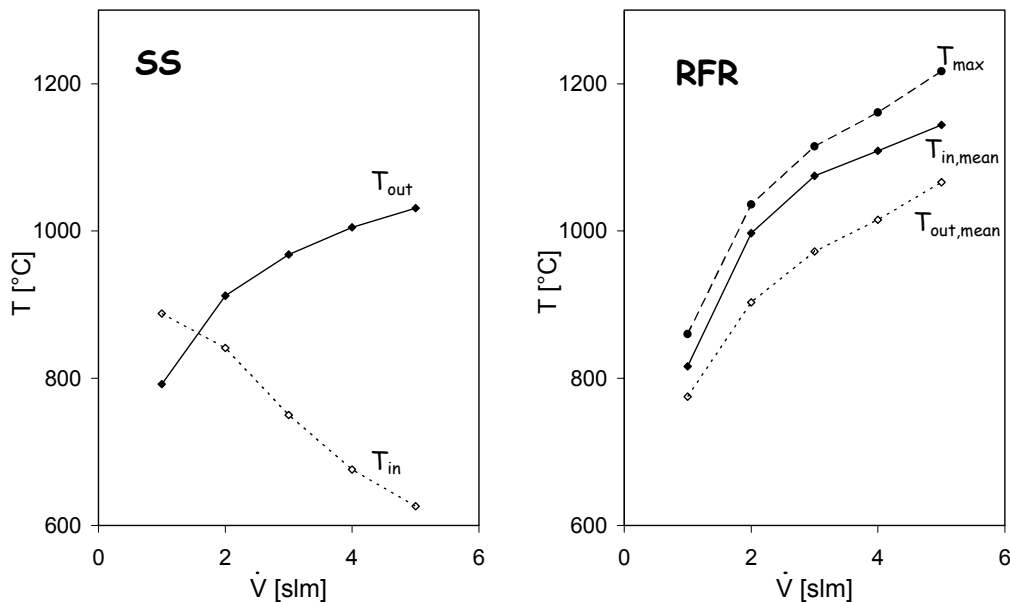


**Figure 16:** Catalyst temperatures as a function of the flow-rate; left: steady-state (SS) reactor, right: RFR;  $CH_4/O_2 = 2.0$ ,  $\tau/2 = 15$  s

flow-rates - and is therefore favorable for syngas yields. On the other hand, increasing the flow-rate leads to higher convective heat transport. This results in a shift of the reaction front further into the catalyst bed and hence a decrease of the catalyst entrance temperature (see Figure 16), thus thermodynamically favoring total oxidation of methane in this zone [16]. These two competing effects lead to maximum selectivities and conversions at a flow-rate of 3 slm in the conventional reactor.

In RFR operation on the contrary, mean catalyst entrance temperatures increase continuously with higher flow-rates and run parallel to exit temperatures of the steady-state process (see Figure 16). To rationalize this behavior, the thermal dynamics of the RFR were studied qualitatively using a thermo-camera. For this, CPOM was performed in a quartz glass reactor without the metal housing, thus allowing IR radiation to be detected with the camera.

Figure 17 shows thermo-camera scans along the reactor axis, which were recorded at flow-rates between 1-4 slm. The catalyst is positioned roughly between 110 and 120 mm. The curves

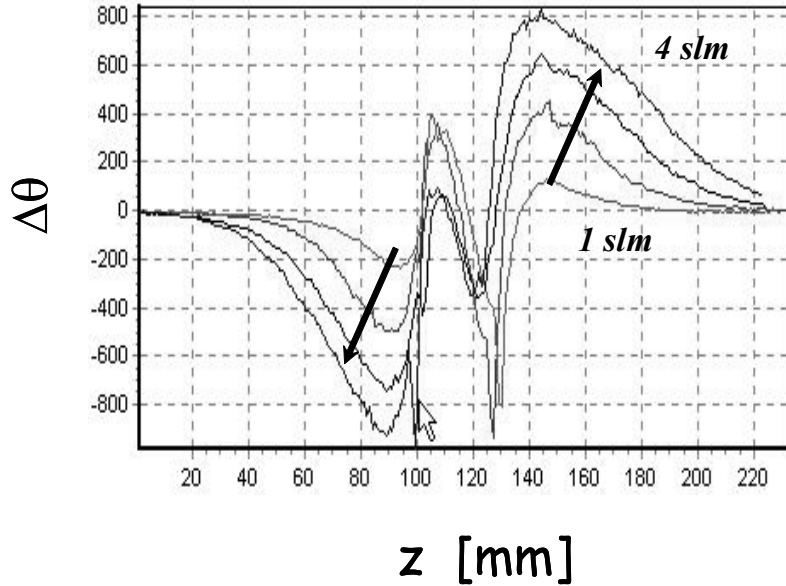


**Figure 17:** *Thermo-camera scans along the reactor axis with varying flow-rates*

represent differences between maximum and mean temperatures (of a full cycle) at every point during one cycle. Clearly,  $\Delta\theta$  increases strongly with higher flow-rates and a much larger part of the inert zone is used for heat-exchange. The amount of sensible heat accumulated in the inert zone is proportional to  $\Delta\theta$  (since  $dH = c_p \cdot dT$ ) and thus increases with higher flow-rates as well. Because more heat is available, regenerative heat-exchange leads to continuously increasing catalyst entrance temperatures with higher flow-rates, as observed in Figure 16. The detrimental effect (with respect to syngas yields) of decreasing temperatures at the catalyst front edge observed in the conventional reactor does therefore not occur in the RFR and explains continuously increasing syngas yields with higher throughputs.

Differences in dynamic behavior of the temperature at the catalyst front and backside in the RFR with varying flow-rates are shown in Figure 18. An in depth discussion of the temperature curve at a flow-rate of 3 slm is performed in chapter 3.2.1. In agreement with above results, the temperature level increases strongly with higher flow-rates. The progression of the temperatures is qualitatively similar for the 3 and 5 slm cases. However, at higher flow-rates maximum catalyst entrance temperatures appear somewhat earlier within the semi-cycle and the slope

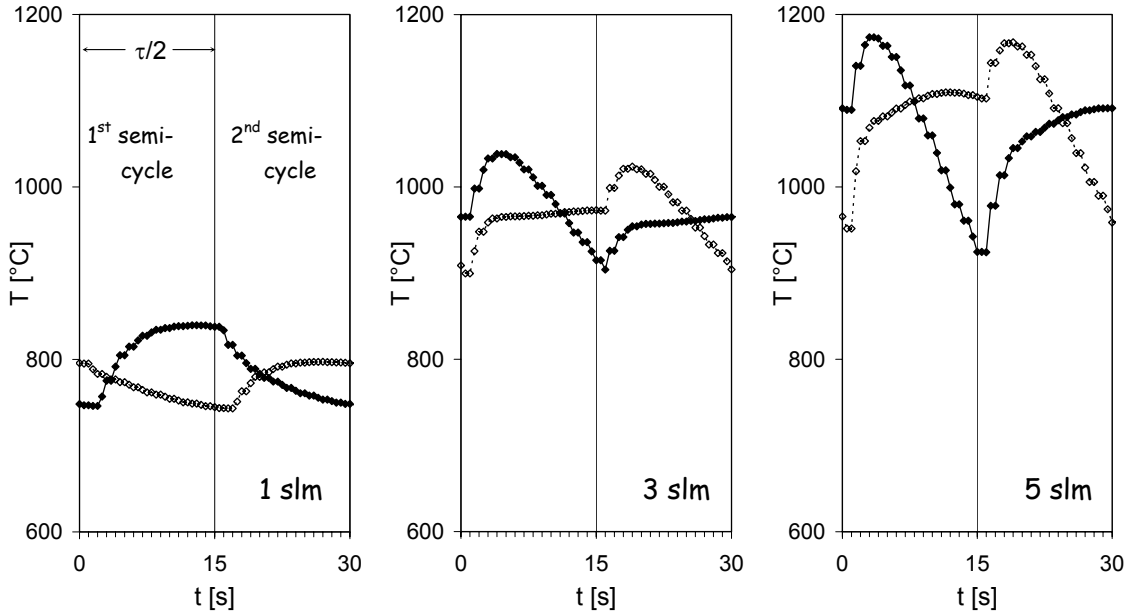


**Figure 18:** *Temperatures in the RFR at the catalyst entrance and exit during 2 semi-cycles at 1 (left), 3 (middle) and 5 slm;  $\tau/2 = 15$  s,  $CH_4/O_2 = 2.0$*

thereafter is steeper due to higher convective heat-transport. The catalyst exit temperature at 5 slm shows a slightly convex curve after the initial strong increase. Temperatures at a flow-rate of 1 slm exhibit a different behavior: the catalyst entrance temperature increases continuously while the catalyst exit temperature decreases during a semi-cycle. These differences are a result of different steady-state temperatures at 1 slm (see Figure 16): at very low flow-rates, catalyst entrance temperatures are higher than catalyst exit temperatures. As a consequence, catalyst exit temperatures decrease and catalyst entrance temperatures increase in RFR operation, as observed in Figure 18.

While the overall temperature level of the catalyst is important for global syngas yields and increases with higher flow-rates, the progression of catalyst entrance and exit temperature during a semi-cycle will be used in chapter 4.0 to evaluate the validity of the reactor model.

Finally, Figure 19 shows steady-state temperature profiles of the conventional process along the reactor axis for different flow-rates (1, 3 and 5 slm, catalyst bed positioned between  $11 \text{ cm} < z < 12 \text{ cm}$ ). As a comparison to steady-state temperature profiles, Figure 20 shows mean temperature profiles for three different flow-rates (1, 3, 5 slm) during dynamic reactor operation

( $\text{CH}_4/\text{O}_2 = 2.0$ ,  $\tau/2 = 15$  s). While the temperature in the region of the reaction zone is elevated compared to the steady-state process, the reactor ends are much colder particularly at high flow-rates, which is generally desirable for the handling of the gases. Evidently, the heat is localized in the region of the catalyst bed in dynamic operation, which is not only advantageous for syngas yields, but also facilitates the design and operation of the reactor, e.g. the sealing of the reactor ends.

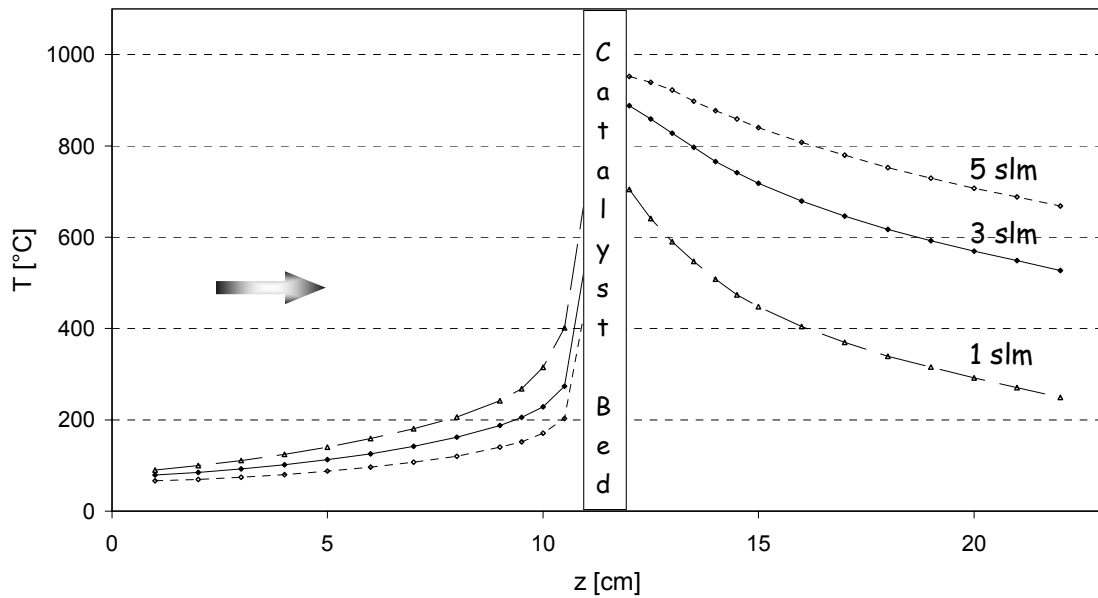


**Figure 19:** Steady-state temperature profiles along the reactor axis  $z$  in the conventional process: 1 (dashed line), 3 (solid line) and 5 (dotted line) slm; flow-direction indicated by arrow

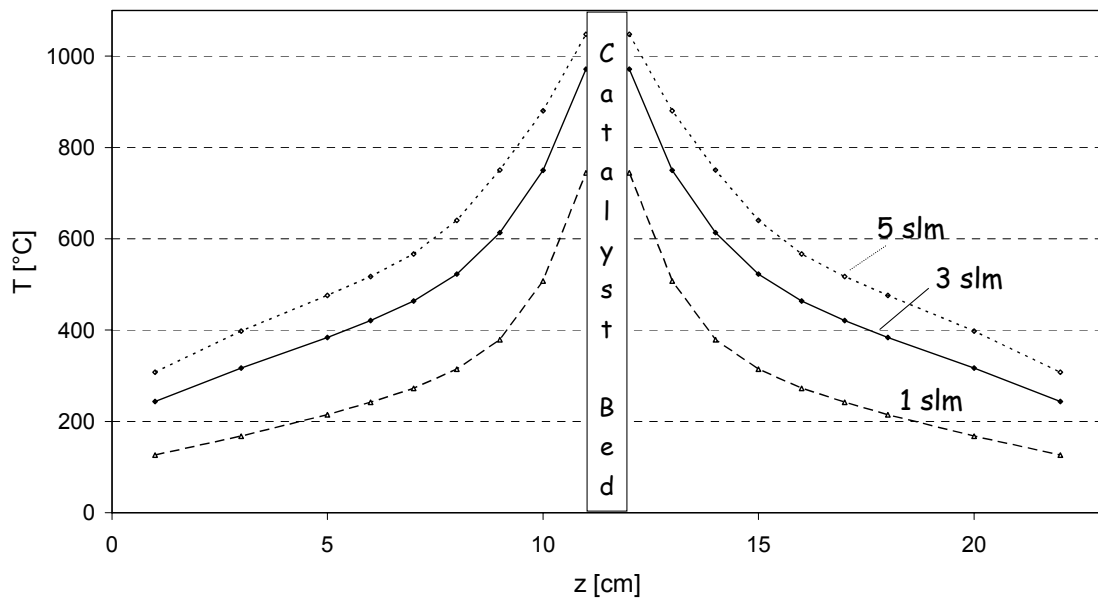


**Figure 20:** Mean temperature profiles along the reactor axis  $z$  in the dynamic RFR: 1 (dashed line), 3 (solid line) and 5 (dotted line) slm

### 3.2.5 Variation of the Pressure

The absolute pressure inside the reactor is strongly dependent on the flow-rate due to the experimental setup (i.e. long capillaries between the reactor and the GC). For flow-rates between 1-5 slm, the absolute pressure inside the reactor varies between 1.2 and 2.2 bar. To ensure that differences in selectivities and conversions with a variation of the flow-rate do not occur due to differences in pressure, the influence of absolute pressure inside the reactor on syngas yields was investigated. Regulation of the absolute pressure was accomplished by installing a needle-valve into the RFR system immediately behind the point where the product gas streams are combined. Opening the valve resulted in a reduction of the absolute pressure inside the reactor.

The pressure drop across the whole reactor length is also dependent on the flow-rate and was investigated as well.

Figure 21 (left graph) shows the progression of the pressure drop across the reactor at a flow-rate of 1, 3 and 5 slm during two semi-cycles as well as mean syngas selectivities and methane conversions as a function of the absolute pressure inside the reactor (right graph) at a flow-rate of 4 slm, a semi-cycling period of 15 s and a  $\text{CH}_4/\text{O}_2$  ratio of 2.0.

The pressure drop across the reactor length increases with higher flow-rates but stays well below 0.1 bar. Such low pressure drops are commonly observed in monolithic systems due to the open structure (> 80 % porosity) of the support material.

As seen in the right-hand graph in Figure 21, CO and  $\text{H}_2$  selectivities as well as  $\text{CH}_4$  conversions remain constant within experimental error (+/- 2 %) over the range of pressures investigated. It can be concluded that the pronounced differences in syngas yields with a variation of the flow-rate observed in chapter 3.2.4 do not arise due to differences in absolute pressure inside the reactor.

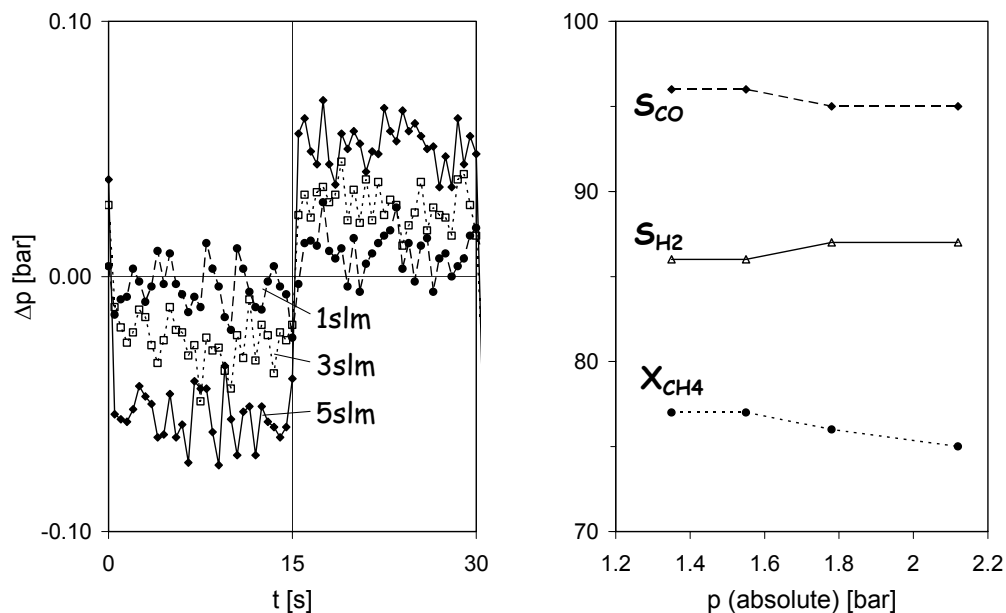


**Figure 21:** Pressure drop across the reactor for 1 (circles), 3 (squares) and 5 (diamonds) slm during 2 semi-cycles (left); Mean syngas selectivities and  $X_{CH_4}$  as a function of the absolute pressure (right);  $CH_4/O_2 = 2.0$ ,  $\dot{V} = 4$  slm,  $\tau/2 = 15$  s

### 3.2.6 Variation of the Catalyst Pore Size

A heterogeneously catalyzed reaction is comprised of several steps including external mass transfer of molecules, their adsorption and desorption to and from the catalyst surface as well as the actual chemical reaction. High autothermal temperatures observed in CPOM result in very high reaction rates on the catalyst surface, which thus suggests that potentially one of the other processes is rate limiting. Veser et al. [15] modeled the system using detailed elementary step reaction kinetics and concluded that the reaction is limited by adsorption of the reactants due to a very low methane sticking coefficient. Bodke et al. [6] experimentally investigated the effect of the support geometry on syngas yields and argued that mass transfer limitations exist which can be reduced e.g. by decreasing the pore size.

To study the behavior of CPOM in dynamic reactor operation using different catalyst supports, the performance of three monoliths with different pore sizes (30, 45 and 80 ppi [= pores per inch]) was studied.



Figure 22 - Figure 24 show selectivities towards CO and H<sub>2</sub> as well as CH<sub>4</sub> conversions as a function of the flow-rate for 30, 45 and 80 ppi monoliths, comparing the steady-state conventional process (SS) with RFR operation. (Previously shown results had been obtained with 45 ppi monolith supports.)

The curves qualitatively show the same behavior as observed in chapter 3.2.4, independently of the pore size of the catalyst support. Nevertheless, quantitative differences exist between different monoliths. While H<sub>2</sub> selectivities and CH<sub>4</sub> conversions increase with decreasing pore size both in conventional and RFR operation, S<sub>CO</sub> shows highest selectivities with the 45 ppi monolith and slightly lower values in the 80 ppi case. Furthermore, the maximum of the curves in the steady-state process becomes broader with decreasing pore size. Selectivities and conversions stay almost constant at high flow-rates in the 80 ppi monolith which suggests that higher flow-rates are attainable without loss in syngas yields as compared to monoliths with larger pores.

Additionally, at flow-rates above 2 slm, absolute enhancements in syngas selectivities and methane conversions in RFR compared to steady-state operation are more pronounced for catalysts with larger pore sizes, i.e. the raise in yields is most apparent for the 30 ppi monolith. Nevertheless, smaller pores generally result in higher syngas yields, both in steady-state as well as dynamic reactor operation.

Selectivity and conversion curves again correlate with temperature profiles. Figure 25 shows catalyst entrance and exit temperatures of the steady-state process, while Figure 26 shows mean and maximum catalyst temperatures measured during RFR operation for the three different catalyst supports. A reduction of catalyst pore size results in lower catalyst exit temperatures in the conventional reactor, while no definite trend can be observed for catalyst entrance temperatures (probably due to the error related to their measurement). In RFR operation, maximum as well as mean catalyst temperatures are much lower for catalyst supports with smaller pore sizes.

In CPOM, more syngas selective catalysts generally exhibit lower catalyst temperatures due to lower reaction enthalpies for partial compared to total oxidation of methane. As observed in Figure 22 - Figure 24, reducing the catalyst pore size enhances partial oxidation reactions and results in increased syngas yields in the conventional and the RFR process. Correspondingly, catalyst exit temperatures decrease with smaller pore sizes (Figure 25). This improvement could

occur due to increased mass transfer rates [6] or higher specific surface areas in the case of monoliths with smaller pores.

Catalyst exit temperatures of the steady-state process directly correlate to the amount of heat accumulated in the heat-reservoir downstream of the catalyst and hence the regenerative heat-exchange in the RFR. Decreasing catalyst exit temperatures result in a smaller amount of heat stored in the inert zone. Therefore, absolute enhancements in the RFR compared to steady-state conditions are more pronounced for less selective catalysts (in this investigation: catalysts with larger pores) due to higher catalyst exit temperatures.

Presented results clearly show that increasing the selectivity of the catalyst or catalyst support not only results in much lower reactor temperatures in steady-state operation (and hence less amount of sensible heat in the system) but also in the RFR (Figure 26). This insight is particularly important regarding a potential catalyst deactivation because it renders the reduction of maximum temperatures (within a certain limit) possible. As will be shown in the next chapter, excessive temperatures result in a fast catalyst deactivation which can hence be avoided by using more selective catalysts (or ‘better’ catalyst supports).

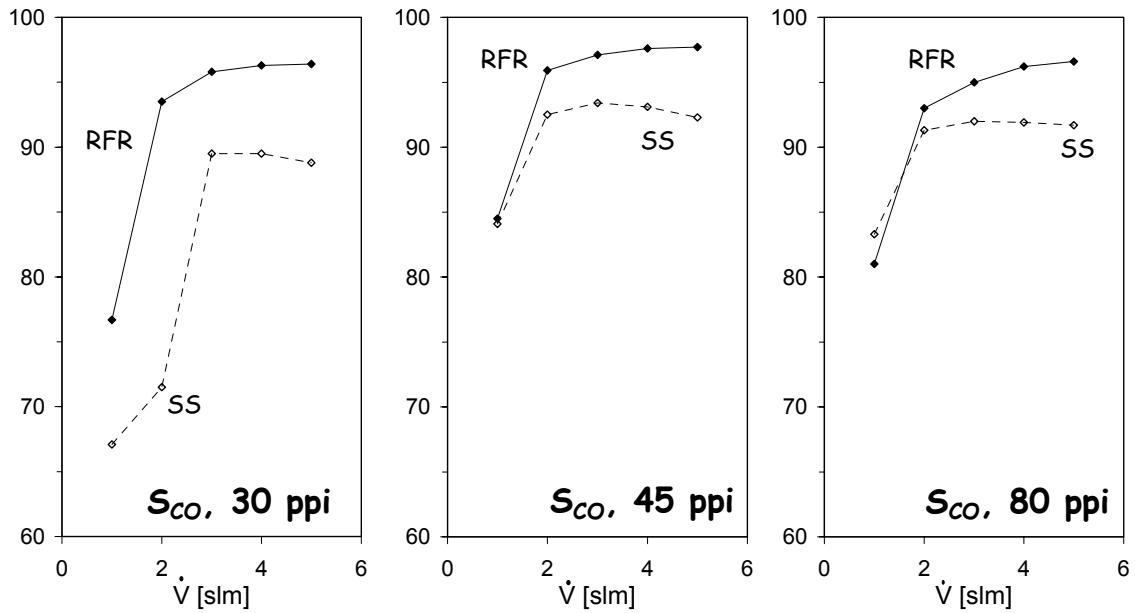


**Figure 22:**  $S_{CO}$  as a function of the flow-rate for 30 (left), 45 (middle) and 80 ppi (right) monolith; steady-state (SS, dotted lines) and RFR (solid lines) operation,  $CH_4/O_2 = 2.0$ ,  $\tau/2 = 15$  s

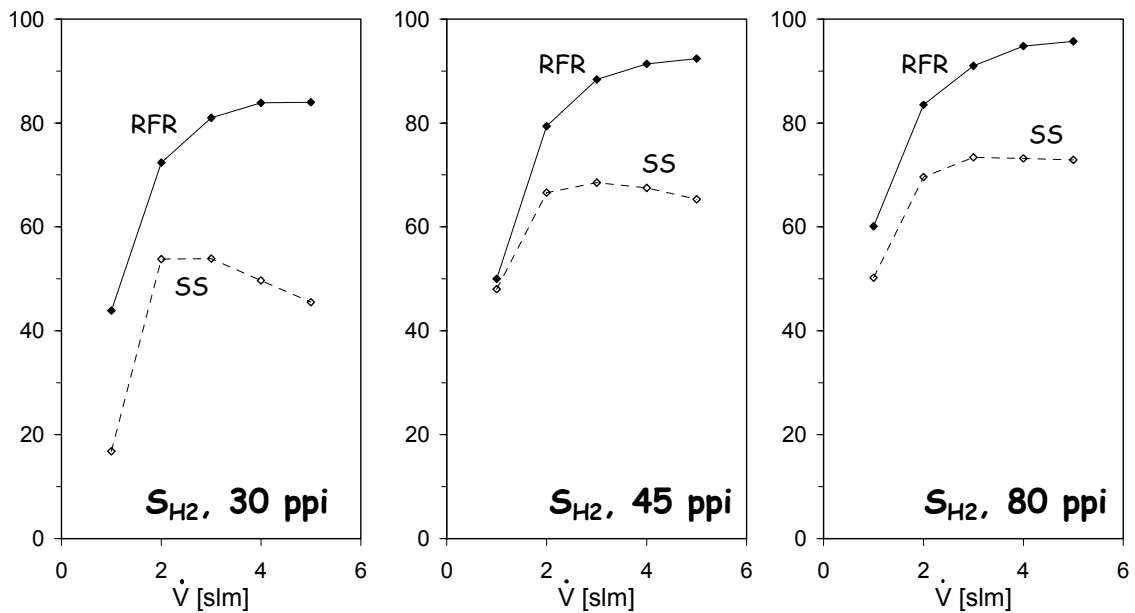


**Figure 23:**  $S_{H_2}$  as a function of the flow-rate for 30 (left), 45 (middle) and 80 ppi (right) monoliths; steady-state (SS, dotted lines) and RFR (solid lines) operation,  $CH_4/O_2 = 2.0$ ,  $\tau/2 = 15$  s

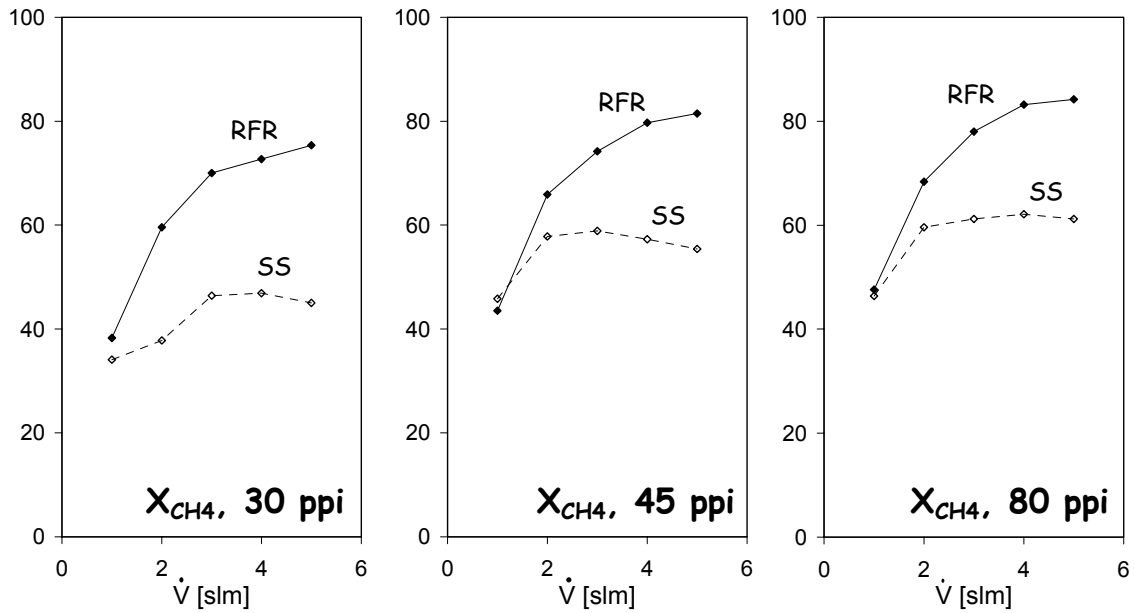


**Figure 24:**  $X_{CH_4}$  as a function of the flow-rate for 30 (left), 45 (middle) and 80 ppi (right) monoliths; steady-state (SS, dotted lines) and RFR (solid lines) operation,  $CH_4/O_2 = 2.0$ ,  $\tau/2 = 15$  s

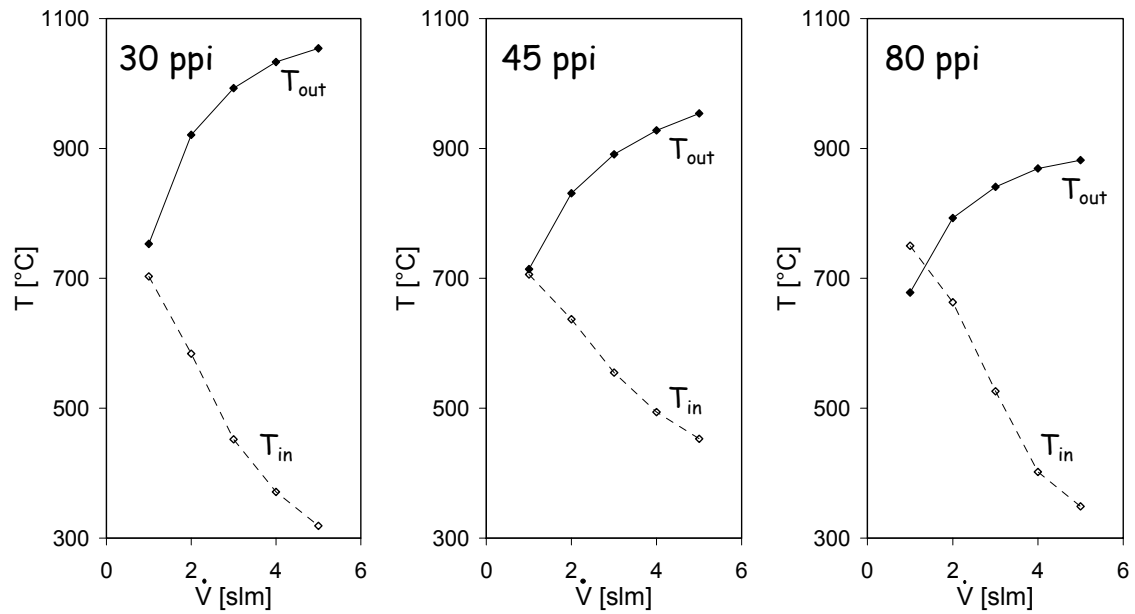


**Figure 25:** Steady-state temperatures as a function of the flow-rate for 30 (left), 45 (middle) and 80 ppi (right) monoliths,  $CH_4/O_2 = 2.0$

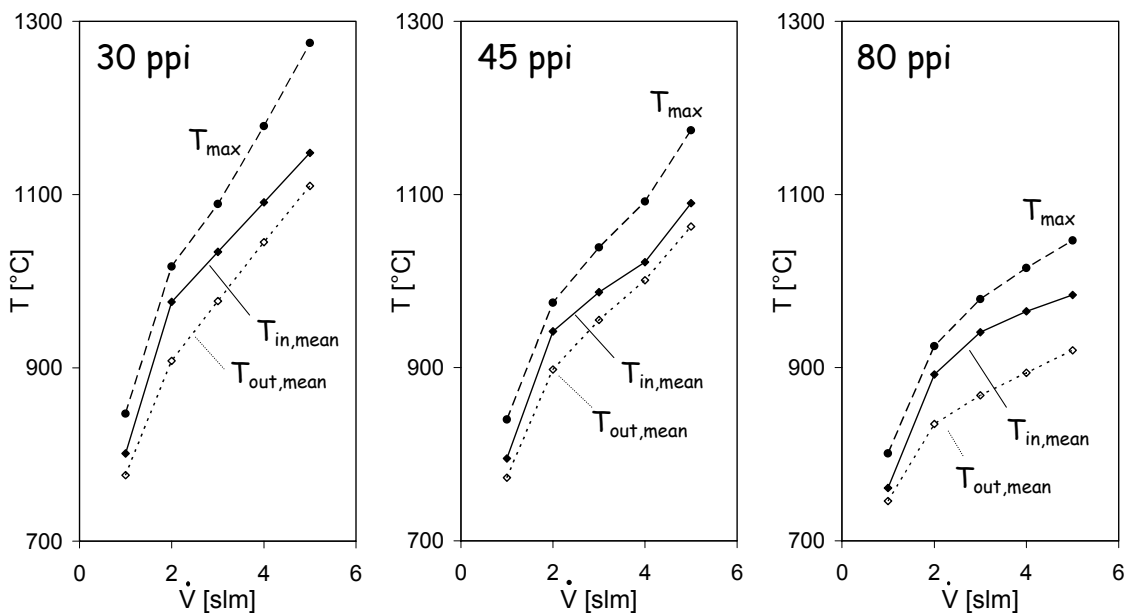


**Figure 26:** RFR temperatures as a function of the flow-rate for 30 (left), 45 (middle) and 80 ppi (right) monoliths,  $CH_4/O_2 = 2.0$ ,  $\tau/2 = 15$  s

### 3.2.7 Catalyst Deactivation

Catalyst deactivation is a problem generally encountered in catalytic reactions. Poisoning as well as loss of active sites due to chemical, thermal and mechanical processes result in a decrease of catalyst activity over time. In many systems, a loss in catalyst activity results not only in decreasing conversions but also decreasing selectivities. Several processes can be held responsible for a catalyst deactivation. Catalyst poisoning by adsorption of for example sulfur, lead or phosphorus onto the catalyst surface and blocking of active metal particles by coke deposition are common causes. At high temperatures, thermal processes like particle sintering and metal evaporation often result in a loss of active sites.

In the investigated system, catalyst poisoning is not likely to occur due to high desorption rates at the high temperature conditions. Furthermore, coke deposition downstream of the catalyst is not observed under normal reaction conditions for the Pt catalyst. While deactivation is already observed in conventional reactor operation, excessive temperatures in the RFR could result in an accelerated deactivation of the catalyst by metal evaporation and sintering [44, 45].

Furthermore, constant flow-reversals in the RFR lead to a periodic ignition/extinction behavior on the catalyst front edge and could result in a degradation of the catalyst due to changes in structure of the active metal sites.

To gain insights into the deactivation behavior of the catalyst in dynamic reactor operation, several long-term experiments were conducted. The studies addressed foremost the following potential deactivation mechanisms: 1. The influence of temperature level as well as maximum temperatures at the catalyst front and backside on the rate of catalyst deactivation; 2. The influence of cycling frequency on the deactivation behavior (due to constant ignition/extinction behavior of the catalyst).

A first experiment was performed to investigate general differences between the steady-state and the RFR process with varying catalyst activity. For this purpose, the reactor was operated in dynamic mode starting with a fresh catalyst and syngas yields recorded as a function of time. Every few hours, reactor operation was switched to steady-state conditions and a measurement taken.

Figure 27 displays partial oxidation selectivities as well as methane conversions for RFR and steady-state operation as a function of time ( $\text{CH}_4/\text{O}_2 = 2.0$ ,  $\dot{V} = 4$  slm,  $\tau/2 = 15$  s). CO selectivities drop by  $\sim 4$  % in steady-state operation over a course of 20 hours while they stay almost constant at  $\sim 97$  % in the RFR.  $\text{H}_2$  selectivities decrease by 31 % in the conventional reactor and by 8 % in the RFR, while  $\text{CH}_4$  conversions decrease by 19 % in steady-state and by 9 % in RFR operation. The fact that syngas selectivities generally decrease with time shows that in the investigated system, a less active catalyst is also less selective.

A strong catalyst deactivation is observed over the course of 20 hours which results in a pronounced decrease in syngas yields. However, the graphs clearly show that with decreasing catalyst activity (i.e. increasing time), the drop in syngas yields is much more pronounced in the conventional process than in the RFR (particularly apparent for  $S_{\text{H}_2}$ ). Obviously, dynamic reactor operation intrinsically counteracts catalyst deactivation.

This feature is a direct result of advantageous temperature profiles in the RFR. Figure 28 shows catalyst temperatures of the steady-state and the RFR process as a function of catalyst deactivation. Increasing catalyst deactivation results in decreasing catalyst entrance and increasing catalyst exit temperatures in the conventional reactor. This suggests a shift of the

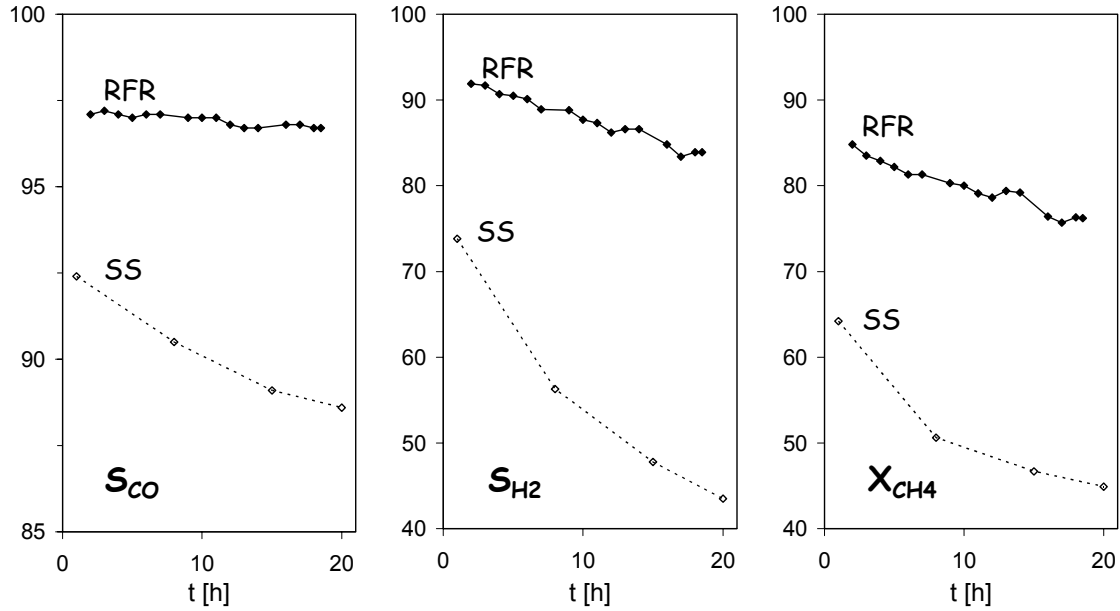


**Figure 27:**  $S_{CO}$  (left),  $S_{H2}$  (middle) and  $X_{CH4}$  (right) as a function of catalyst activity; steady-state (dotted lines) and RFR (solid lines) operation;  $CH_4/O_2 = 2.0$ ,  $\dot{V} = 4 \text{ slm}$ ,  $\tau/2 = 15 \text{ s}$

reaction front further into the catalyst bed and is consistent with decreasing conversion rates at lower catalyst activities. In the RFR, however, mean and maximum catalyst temperatures increase continuously. Decreasing reaction selectivities result in increased catalyst exit temperatures in the conventional reactor and hence lead to an increased amount of heat integrated in the RFR, as was already discussed in chapter 3.2.6. As a consequence, catalyst entrance temperatures increase continuously in the RFR which counteracts catalyst deactivation and results in a less dramatic decrease in syngas yields in dynamic reactor operation. Nevertheless, this advantageous feature comes at the expense of a further increase in catalyst temperatures. This could lead to an even faster catalyst deactivation if a temperature sensitive catalyst is used.

To investigate the influence of temperature level, maximum temperatures and cycling frequency on the rate of catalyst deactivation, several additional long-term experiments were performed. Table 1 lists four different runs and their respective set of reactor operating parameters. While run 1 is the experiment discussed in more detail above, run 4 is identical to run 1 and was performed to test the reproducibility of the deactivation behavior of the catalyst.

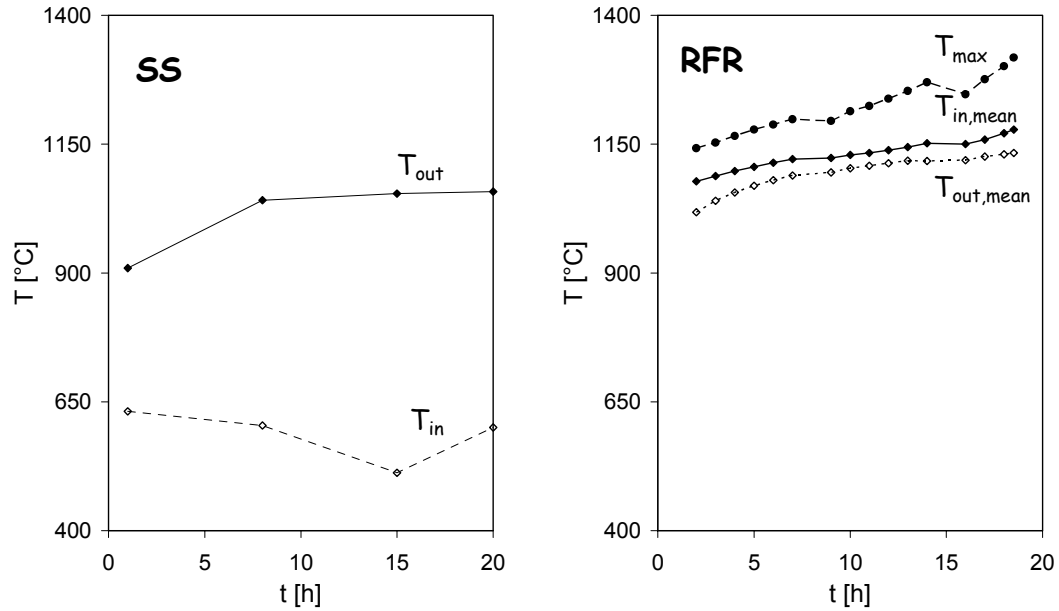


**Figure 28:** Catalyst temperatures of the steady-state (SS, left) and the RFR process as a function of reactor catalyst activity;  $CH_4/O_2 = 2.0$ ,  $\dot{V} = 4$  slm,  $\tau/2 = 15$  s

**Table 1:** Reactor parameters for four different experimental long-term runs

No. of run	flow rate $\dot{V}$ [slm]	$CH_4/O_2$	$\tau/2$ [s]	duration [h]
1	4	2.0	15	20
2	4	2.0	30	10
3	2	2.0	15	40
4	4	2.0	15	20

Figure 29 shows selectivities towards CO and H<sub>2</sub> as well as CH<sub>4</sub> conversions as a function of time for the four runs. While CO selectivities remain constant in run 3 (~ 95 % over the course of 40 hours), runs 1, 2 and 4 show a slight decrease (from 97 to ~ 96.5 % in runs 1 and 4 in 20 hours and by about the same amount but in 10 hours in run 2). The decrease in H<sub>2</sub> selectivities is most pronounced in run 2 (~ 6 % in 10 hours), slightly less pronounced in runs 1 and 4 (~ 8 and 6 % in 20 hours, respectively) and run 3 (~ 8 % in 40 hours). The decrease in CH<sub>4</sub> conversions



for the 4 runs qualitatively shows a similar behavior as the decrease in  $S_{H_2}$  (by 9 % in 20 hours in run 1, by 6 % in 20 hours in run 4, by 7 % in 10 hours in run 2 and by 6 % in 40 hours in run 3).

Catalyst deactivation proceeds faster in runs 1, 2 and 4 compared to run 3 as observed by a more pronounced decrease in syngas yields over time. A comparison between operating parameters of runs 1 and 3 suggests that lower flow-rates are preferable for a slower catalyst deactivation. Particularly run 2 shows a very strong deactivation behavior. The fact that the cycling time for run 2 is longer than for runs 1 and 4 but the catalyst deactivates faster, suggests that cycling frequency does not have a major influence on catalyst deactivation.

To investigate the potential influence of thermal effects on catalyst deactivation, maximum and mean catalyst entrance and exit temperatures were measured and are displayed in Figure 30. Maximum temperatures increase continuously by about 200°C within 10 hours in run 2 and about the same amount within 20 hours in run 1 and 4. In run 3, they increase by 80°C within 40 hours. Mean catalyst entrance temperatures increase by 130°C in runs 1 and 4, by 70°C in run 2 and by 90°C in run 3. Exit temperatures increase by 110°C in run 1, by 140°C in run 4, by 120°C in run 2 and by 110°C in run 3. Temperatures levels are generally lower in run 3 than in runs 1, 2 and 4. This is particularly pronounced for maximum temperatures. Mean catalyst entrance temperatures in run 2 are lower than in runs 1 and 4, but maximum temperatures increase faster with time.

In the investigated system it is highly likely that deactivation occurs due to sintering and/or metal evaporation due to high temperature conditions. However, different effects are potentially overlaid and restrict the possibility of interpreting the presented results. Even though the information content of the long-term runs regarding deactivation of the catalysts is thus limited, some general conclusions shall be drawn.

The slopes of the temperature and yield curves imply that catalyst deactivation proceeds fastest in run 2 and slowest in run 3. A major difference between these runs are maximum temperatures, which are 200-300°C higher in run 2, while mean catalyst entrance temperatures are almost identical. This strongly suggests that excessive maximum temperatures (and not the temperature level in general) are detrimental for catalyst activity, either due to sintering or metal evaporation effects.

A further observation made during the experiments suggests that metal evaporation does in fact occur to some extent: While the color of a fresh inert zone is beige to white, a distinct

discoloration to grey is observed after several hours of reactor operation. While this change in color could potentially also occur due to a change in the cordierite structure at high temperature conditions, it could also suggest that evaporated Pt from the catalyst is deposited on the walls of the extruded monolith. However, this observation should be confirmed by an analysis of the metal content on the inert zone e.g. by EDX measurements.

As mentioned above, the cycling frequency (and hence detrimental effects of restructuring of the metal due to repeated ignition/extinction of the reaction) does not seem to have a major effect on catalyst activity since the deactivation rate in run 2 is equal (or even higher) than in runs 1 and 4 even though the cycling periodicity is longer.

Furthermore, the asymptotic behavior of temperature and yield curves in run 3 suggests that the rate of catalyst deactivation is reduced towards the end of the run and a constant catalyst activity might be reached. However, temperatures towards the end of the run are generally higher than in the beginning. This suggests that temperatures are not the only cause for deactivation and an additional deactivation mechanism (e.g. restructuring of the fresh catalyst) also plays a role.

It is thus suggested that several overlaid processes influence catalyst deactivation in the investigated system. While the cycling frequency does not seem to have an effect on the catalyst degradation, maximum temperatures were found to have a strongly detrimental effect which suggests that metal evaporation and/or sintering reduce catalytic activity.

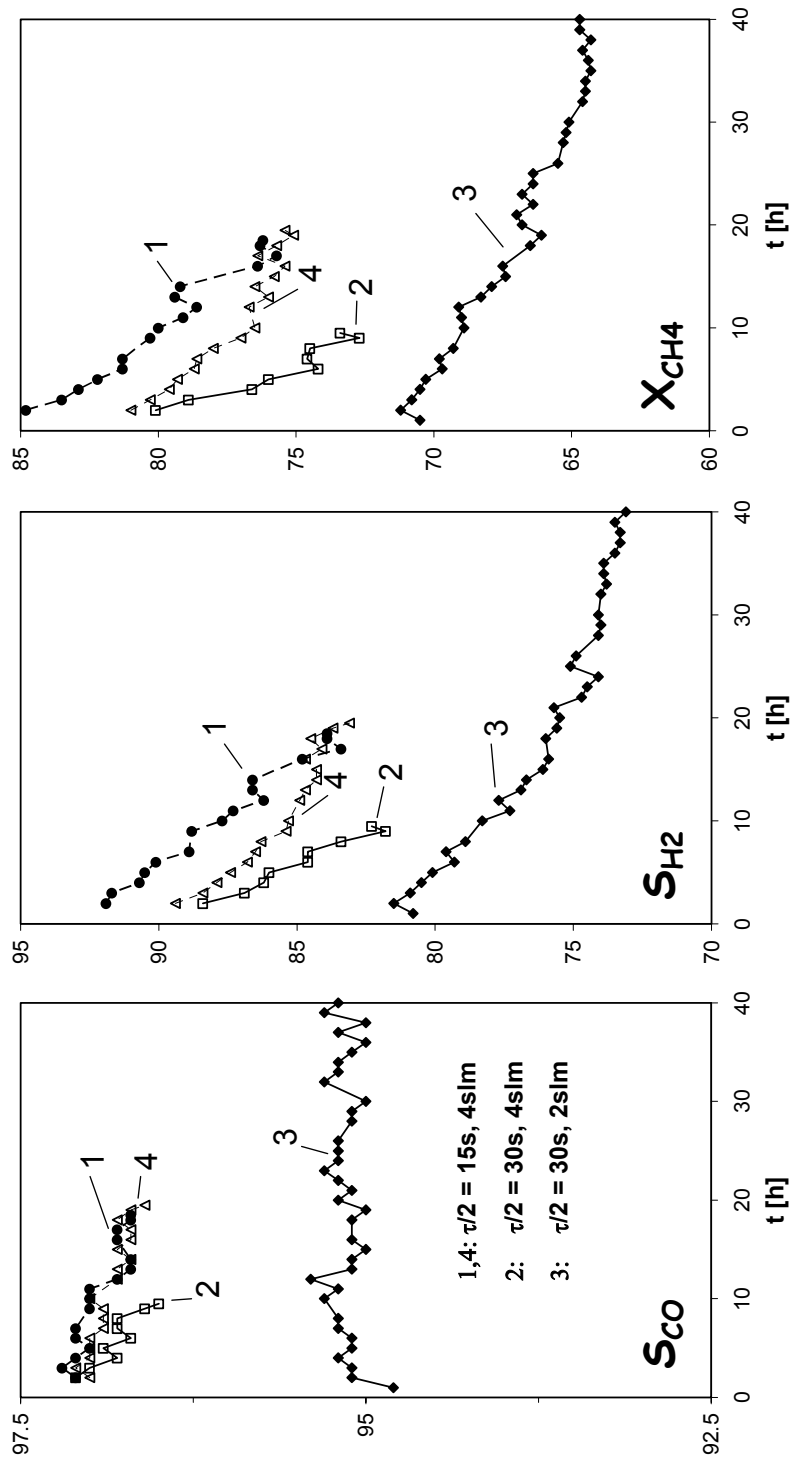


**Figure 29:**  $S_{CO}$  (left),  $S_{H_2}$  (middle) and  $X_{CH_4}$  (right) as a function of time: run 1: solid circles and dashed lines; run 2: hollow squares and solid lines; run 3: solid diamonds and solid lines; run 4: hollow triangles and dotted lines

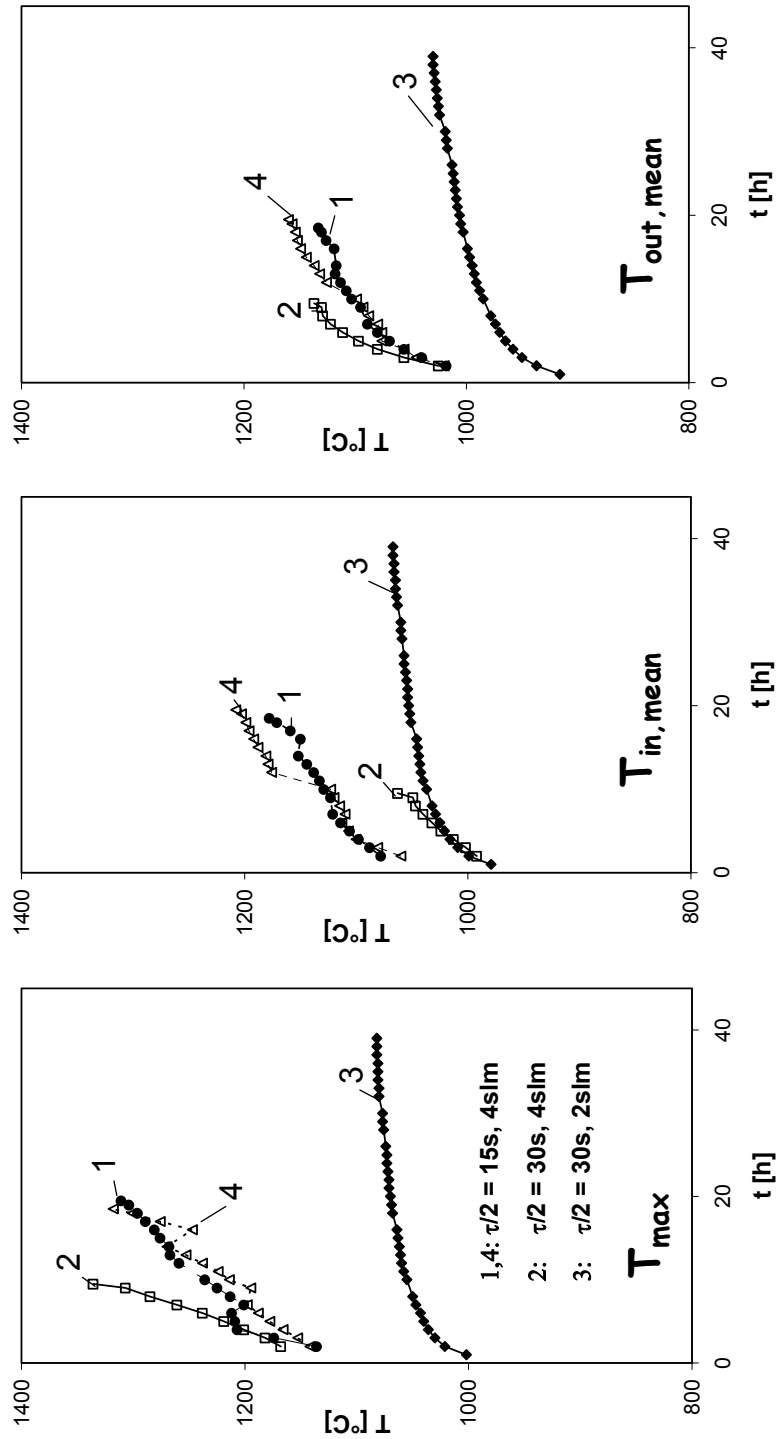


**Figure 30:** RFR temperatures as a function of time; run 1: solid circles and dashed lines; run 2: hollow squares and solid lines; run 3: solid diamonds and solid lines; run 4: hollow triangles and dotted lines

In addition to the conclusions drawn from the experiments, some general observations made during the long-term runs are listed in the following:

1. The ignition of homogenous reactions inside the inert zone upstream of the catalyst (where oxygen is still present) occurred if the temperature level in this heat-reservoir increased above  $\sim 1350$  °C. In those cases it was observed that during a semi-cycle the temperature upstream of the catalyst increased with time when under normal circumstances convective heat-transport of the reactants reduced it. Parallel to these temperature peaks, partial oxidation product concentrations measured with the MS showed a dip. It is therefore assumed that unselective homogeneous combustion of methane occurred upstream of the catalyst. Two reasons (or probably a combination of both) could potentially lead to these extreme temperatures and ignite homogeneous gas phase chemistry: a) the inert zone downstream of the catalyst is heated up too much during the preceding semi-cycle so that after flow-reversal, the temperature level of this inert zone is too high; b) radiation effects on the leading edge of the catalyst result in an increase of the temperature upstream of the catalyst.

Similar observations were made by Blanks et al. [38] who investigated CPOM in an RFR using Ni catalysts. Ignition of homogeneous reactions in the inert zones quickly (within a couple of minutes) leads to temperatures which exceed the range of the thermocouples and result in melting of the inert zone as well as breakage of the thermocouple. Furthermore, deposition of carbon inside the inert zones was noticed which could clog the channels. Therefore, experiments were stopped once maximum temperatures exceeded  $1300$ - $1350$ °C, which was observed to be the critical temperature.

2. During the deactivation experiments it was observed that with increasing temperature, additional peaks appeared in the gas chromatogram. The positions of the peaks correlate to ethane, ethylene and/or acetylene. Unfortunately, the GC setup does not allow to differentiate between these 3 substances due to similar retention times on the column used. Nevertheless, the concentrations measured for these components were well below 0.1 % and therefore not significant. Furthermore, during the course of several days to weeks of reactor operation at excessively high temperatures, a red/brown substance which is soluble in acetone is deposited in the capillaries leading away from the reactor.

The actual concentrations of these products are extremely small and not detectable with the GC or MS. An analysis of the oily substance gave no conclusive results (i.e. the exact composition is not known) but it is assumed that it is a mixture of different hydrocarbons.

Finally, a more general result which can be extracted from presented experiments is that evidently minimum catalyst activity is necessary to maintain reactor temperatures at an acceptable level at high flow-rates. As observed in the experiments, once the catalyst activity is too low, excessive temperatures at high flow-rates result in the ignition of homogeneous reactions and necessitate the shutdown of the reactor operation.

### 3.2.8 Testing Novel Nano-Structured Catalysts

The presented experiments show that efficient regenerative heat-exchange in CPOM results in a strong increase in syngas yields. This principle is generally applicable for any catalyst as long as temperatures are kept below the ignition temperature of homogeneous reactions inside the inert zone. However, Pt-coated foam monoliths used throughout the experiments proved to deactivate rather quickly.

Apart from the focus on application of efficient, multifunctional reactor concepts, a topic addressed in our research group is the development of high temperature stable nano-structured catalysts. Recent progress in this area resulted in the synthesis of highly syngas selective Pt catalysts which were shown to be stable under high temperature conditions for at least 100 hours in a steady-state process [46].

In the following, experimental runs in dynamic reactor operation using these novel nano-structured Pt catalysts are presented. The catalyst consists of a powder, which was inserted into the reactor by sandwiching it between sheets of alumina floss. Apart from general insights into the reaction behavior using a powdered catalyst, the deactivation behavior of the catalyst was of primary interest.

Figure 31 shows syngas selectivities and methane conversions (left) as well as RFR temperatures (right) during 10 hours of dynamic reactor operation at a  $\text{CH}_4/\text{O}_2$  ratio of 2.0, a flow-rate of 4 slm and a semi-cycling period of 15 s. Very high partial oxidation selectivities (~

95 %) and high methane conversions (~ 85 %) at moderate maximum temperatures ( $T < 1100^{\circ}\text{C}$ ) are observed. Additionally, since the ratio of  $\text{H}_2$  and CO selectivity is close to one, the product gas composition has the ideal  $\text{H}_2/\text{CO}$  ratio of 2.0 needed for most downstream processes. Generally, the catalyst does not show any sign of deactivation over the short time-period investigated.

Finally, Figure 32 shows syngas yields and temperatures as a function of the  $\text{CH}_4/\text{O}_2$  ratio for steady-state and dynamic reactor operation. While particularly  $\text{H}_2$  selectivities and  $\text{CH}_4$  conversions at steady-state conditions are significantly improved in comparison to the conventional monolith-supported Pt catalysts (Figure 12), syngas selectivities and methane conversions generally increase by about 10-15 % in dynamic RFR operation.

These results confirm that enhancements in syngas yields in the RFR are independent of the catalyst used. Dynamic reactor operation generally yields better syngas selectivities as well as methane conversions and the reactor configuration seems universally applicable. Furthermore, the structure of the catalyst bed is, at least for the experimental investigation performed, not decisive for enhancements achieved in dynamic reactor operation.

It can be concluded that optimization of the investigated system must not only incorporate optimization of the reactor configuration but also of the catalyst itself.

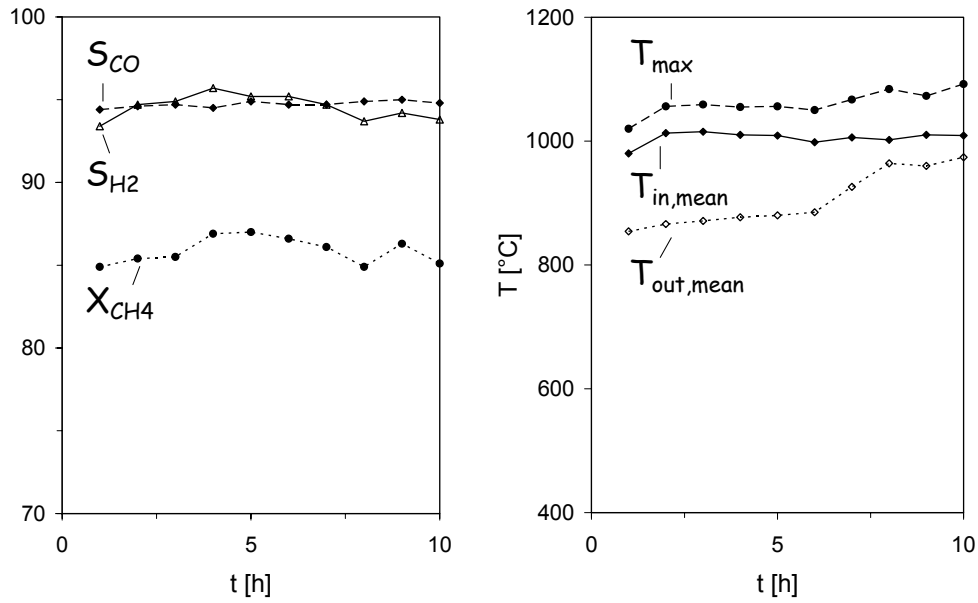


**Figure 31:**  $X_{CH_4}$  (dotted line),  $S_{CO}$  (dashed line) and  $S_{H_2}$  (solid line, left) as well as RFR temperatures (right) as a function of time using a Pt nano-catalyst;  $CH_4/O_2 = 2.0$ ,  $\dot{V} = 4$  slm,  $\tau/2 = 15$  s

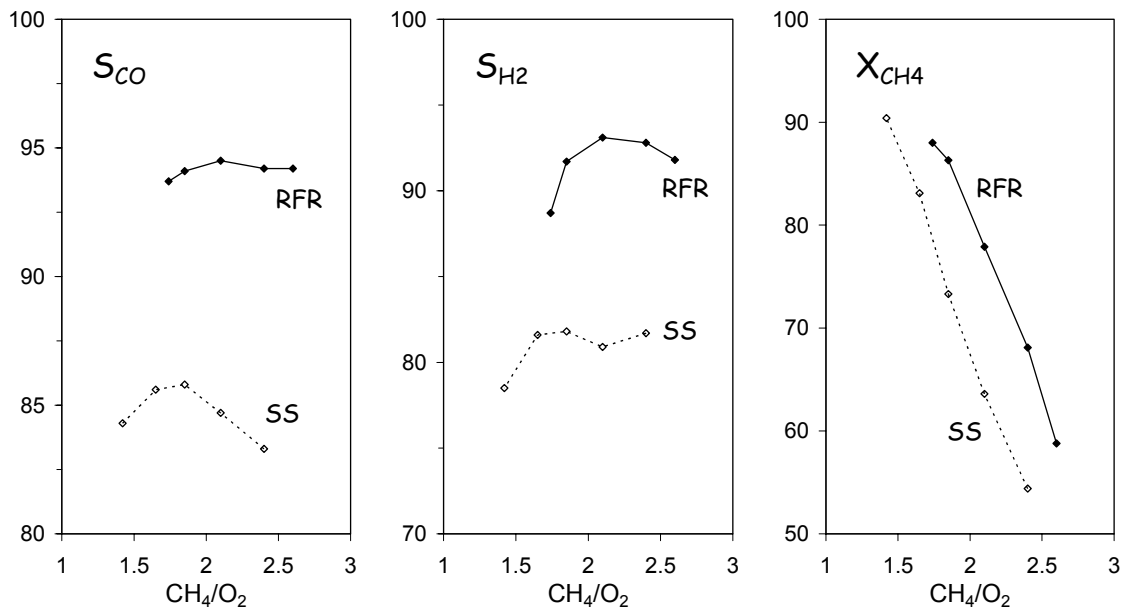


**Figure 32:**  $S_{CO}$  (left),  $S_{H_2}$  (middle) and  $X_{CH_4}$  (right) as a function of the  $CH_4/O_2$  ratio using Pt nano-catalyst; steady-state (dashed lines) and RFR (solid lines) operation;  $\dot{V} = 4$  slm,  $\tau/2 = 15$  s



### 3.3 Discussion

#### 3.3.1 Reactor Temperatures and Syngas Yields

Performing CPOM in a laboratory-scale RFR strongly increases  $\text{CH}_4$  conversions and selectivities towards  $\text{H}_2$  and  $\text{CO}$  in all cases investigated when compared to operation in a conventional steady-state reactor. This improvement is the direct result of an increase in catalyst entrance temperatures and advantageous temperature profiles along the reactor axis in the RFR.

Catalyst temperatures have a major influence on syngas yields in the investigated reaction system. Due to differences in reaction enthalpies for the two competing reaction pathways ( $\Delta H_r = -800$  kJ/mol for total oxidation and  $\Delta H_r = -37$  kJ/mol for partial oxidation of methane), low temperatures thermodynamically result in a preferential combustion of methane which is by definition detrimental for syngas selectivities. While in steady-state reactor operation catalyst exit temperatures are generally very high, catalyst entrance temperatures are much lower and decrease strongly with increasing flow-rates, thus favoring total oxidation of methane in the front section of the catalyst bed [16].

The temperature at the catalyst entrance is mainly influenced by convective cooling of the reactants as well as thermal conductivity of the catalyst. Hohn et al. [10] could show that by using alumina spheres rather than alumina foam monolith as a support, one can influence the heat-transfer properties and effectively increase syngas yields at high space-velocities over Rh-catalysts. In contrast to that, dynamic reactor operation leads to a strong increase in catalyst entrance temperatures due to efficient regenerative heat-exchange. Therefore, total oxidation is reduced and syngas yields improved compared to conventional reactor operation. Enhancements in selectivities and conversions could in all cases be explained by advantageous temperature profiles in the RFR throughout the experiments performed.

However, deactivation experiments revealed that dynamic reactor operation is limited by excessively high temperatures, which not only result in a quick decrease in catalyst activity, but ultimately lead to ignition of unselective gas phase reactions inside the heat-reservoir. Homogeneous reactions in the inert zone were observed to reduce syngas yields and quickly lead to unacceptably high temperatures which degrade reactor stability (i.e. melting of inert zone).

Excessively high temperatures must thus be prevented under any circumstances. This can be accomplished e.g. by lowering the flow-rate through the reactor. Additionally, using more syngas selective catalysts (or catalyst supports) is not only preferential with respect to overall syngas yields, but also results in a strong decrease of reactor temperatures in the investigated system. This highlights the necessity of optimizing not only the reactor configuration but also the catalyst for an optimization of CPOM.

### 3.3.2 Converting Sensible Heat into Chemical Energy

The RFR principle is based upon the idea of integrating sensible heat released by an exothermic reaction into the system to increase catalyst temperatures. The additional heat fed back to the system is (to a certain extent) converted into chemical energy which is observed in form of an increase in syngas yields (in case of CPOM). However, due to heat losses, non ideal reactor operation as well as kinetic limitations not all of the sensible heat is eventually converted into chemical energy. To characterize the system, it is important to estimate the efficiency  $\eta$  of dynamic operation, i.e. how much of the sensible heat is ultimately converted into chemical energy. Some basic calculations using experimental data presented throughout chapter 3.0 are thus performed.

Figure 33 shows an enthalpy versus temperature plot to schematically illustrate the calculations described in the following. In the steady-state process, products exit the catalyst bed at a high temperature  $T_{\text{catalyst-exit,SS}}$  and a relatively low enthalpy ( $H_{\text{SS}}$ ). The products of the RFR process exit the reactor at a low temperature ( $T_{\text{reactor-exit,RFR}}$ ) and a higher enthalpy due to increased syngas yields ( $H_{\text{RFR}}$ ). The difference between  $T_{\text{catalyst-exit,SS}}$  and  $T_{\text{reactor-exit,RFR}}$  is proportional to the amount of sensible heat which is integrated from the steady-state process in the RFR. The difference between the enthalpies of the steady-state and the RFR process at temperature  $T_{\text{reactor-exit,RFR}}$  is equal to the difference in latent heat of the product gases (i.e. the difference in chemical energy). The efficiency estimates how much of the sensible heat is converted into latent heat.

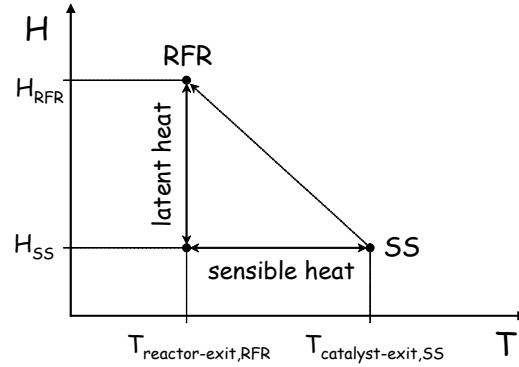


**Figure 33:** Schematic  $H$  vs.  $T$  diagram illustrating function principle of RFR

The change in sensible heat of a gas is proportional to the change in temperature and is defined as:

$$dH = c_p dT$$

Since the product gas is a mixture of different components, the respective heat-capacities are multiplied with the molar flow of the gas species and yield an enthalpy flow (of sensible heat):

$$\dot{H}_{sh} = \sum_i \dot{n}_{i,SS} \cdot (c_{p,i} T_{catalyst-exit,SS} - c_{p,i} T_{reactor-exit,RFR})$$

where  $\dot{H}_{sh}$  is the flow of sensible heat,  $\dot{n}_{i,SS}$  is the molar flow of component  $i$  of the steady-state process,  $c_{p,i}$  is the temperature dependent heat-capacity of species  $i$ ,  $T_{catalyst-exit,SS}$  is the temperature at the catalyst exit in the steady-state process and  $T_{reactor-exit,RFR}$  is the temperature at the reactor exit in the RFR.  $\dot{H}_{sh}$  thus represents the maximum amount of enthalpy per time unit which is integrated in the RFR system.

Differences in latent heat between product gases of the RFR and the steady-state process are calculated with the respective product gas compositions and enthalpies at the exit temperature of the reactor in dynamic operation. This difference therefore represents the amount of enthalpy that was converted into ‘chemical energy’ in the RFR. Again, enthalpies are expressed as enthalpy flows by multiplying the enthalpy of species  $i$  with the molar flow and yield:

$$\Delta\dot{H}_{RFR-SS} = \sum_i \dot{n}_{i,RFR} H_i(T_{reactor-exit,RFR}) - \sum_i \dot{n}_{i,SS} H_i(T_{reactor-exit,RFR})$$

where  $\Delta\dot{H}_{RFR-SS}$  is the difference in enthalpy flow between RFR and steady-state operation,  $\dot{n}_{i,RFR}$  is the molar flow of the RFR product gas component  $i$ ,  $H_i$  is the enthalpy of species  $i$  at temperature  $T$ .

The efficiency  $\eta$  of converting sensible heat into chemical energy through regenerative heat-exchange is calculated by dividing the two enthalpy flows:

$$\eta = \frac{\Delta\dot{H}_{RFR-SS}}{\dot{H}_{sh}}$$

This is a conservative approximation of the efficiency since the sensible heat enthalpy flow does not take heat losses of the reactor to the surroundings into account, which occur in the laboratory-scale reactor. These heat-losses reduce  $T_{reactor-exit,RFR}$  and increase  $\dot{H}_{sh}$  compared to the case if heat losses were accounted for, thus reducing the overall efficiency.

Using above equations and experimental data (chapter 3.2), reactor efficiencies were calculated as a function of the  $CH_4/O_2$  ratio, the flow-rate as well as catalyst activity and are shown in Figure 34.

A variation of the  $CH_4/O_2$  ratio has hardly any influence on process efficiency which remains almost constant at about 50 % over the range investigated and given reactor parameters. This is in agreement with yield (Figure 12) and temperature (Figure 13) curves, which run parallel for steady-state and RFR operation. However, since maximum  $H_2$  selectivities are shifted towards higher  $CH_4/O_2$  ratios in the RFR compared to the conventional reactor and decrease at a  $CH_4/O_2$  ratio of 1.4, a slight reduction in process efficiency is observed at low  $CH_4/O_2$  ratios.

Variation of the flow-rate on the other hand has a pronounced effect on process efficiency, which increases from below 20 % at a flow-rate of 1 slm to above 70 % at 5 slm. This correlates well with results presented in chapter 3.2.4. Thermo-camera scans (Figure 17) showed that at higher flow-rates a much larger portion of the inert zone is used for regenerative heat-exchange, which results in a pronounced increase in process efficiency. As a consequence,  $S_{H_2}$ ,  $S_{CO}$  and

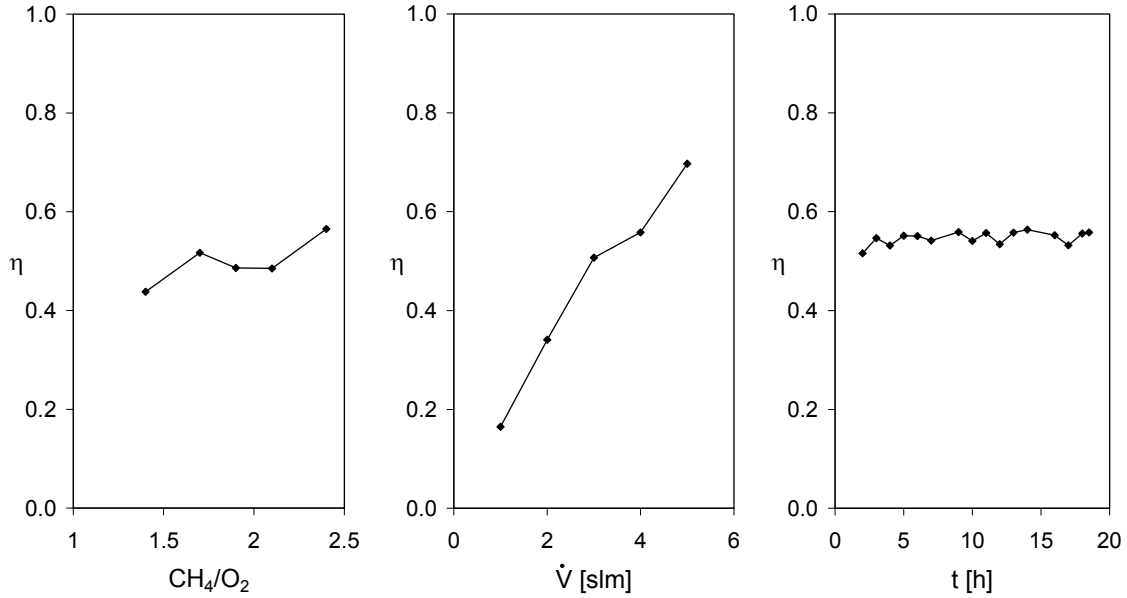


**Figure 34:** Efficiency of heat-integration in the RFR as a function of  $\text{CH}_4/\text{O}_2$ -ratio ( $\dot{V} = 4$  slm,  $\tau/2 = 15$  s, left), flow-rate ( $\text{CH}_4/\text{O}_2 = 2.0$ ,  $\tau/2 = 15$  s, middle) and catalyst deactivation ( $\text{CH}_4/\text{O}_2 = 2.0$ ,  $\tau/2 = 15$  s,  $\dot{V} = 4$  slm, right)

$X_{\text{CH}_4}$  curves of steady-state compared to RFR operation diverge with increasing flow-rates (Figure 15). The results clearly emphasize that high flow-rates are not only beneficial for high syngas yields, but necessary for good process efficiency.

Catalyst deactivation does not have an influence on  $\eta$ , which remains constant at 55 % over the range of activities investigated. This is at first surprising, since it was clearly observed in Figure 27 that dynamic reactor operation intrinsically counteracts catalyst deactivation and syngas yields decrease slower than in the conventional reactor. Hence,  $\Delta\dot{H}_{\text{RFR-SS}}$  increases with decreasing catalyst activity which should generally be a result of increased process efficiency. However, catalyst deactivation also leads to an increase in the amount of available sensible heat ( $\dot{H}_{sh}$ ) due to changing product gas compositions (particularly decreasing  $S_{\text{H}_2}$  in conventional reactor operation). As a consequence, overall efficiency of the heat-integration remains constant even though yields between steady-state and conventional reactor operation diverge.

### 3.3.3 Thermodynamics and Kinetics

A chemical reaction is influenced by thermodynamics and kinetics. While thermodynamics determine the equilibrium state of the system and can hence set limits to the maximum achievable selectivities and conversions, kinetics determine the rate of a reaction step and thus the reaction route taken during the approach to equilibrium.

In conventional syngas production (e.g. ATR), where residence times inside the reactor lie in the order of several seconds, product gas compositions are determined by the thermodynamic equilibrium composition at the exit temperature of the reactor. While the residence times in high temperature catalytic reactions only lie in the range of several milliseconds, extreme temperatures observed in CPOM result in very high reaction rates which suggests that thermodynamic equilibrium could nevertheless be reached.

To investigate the importance of kinetics on the overall process in CPOM, experimental results are compared to thermodynamic equilibrium calculations in the following.

Let us assume that in CPOM thermodynamic equilibrium is reached. In this case, the product gas composition exiting the system should be equal to the thermodynamic equilibrium composition of the quenching temperature (i.e. the temperature where the composition is ‘frozen’ due to very slow reaction rates). Figure 35 shows partial oxidation selectivities as well as methane conversions at thermodynamic equilibrium as a function of temperature for a  $\text{CH}_4/\text{O}_2$  ratio of 2.0. While a pronounced increase in syngas yields is observed with increasing temperatures, CO selectivities stay below  $\text{H}_2$  selectivities over the whole range of temperatures investigated. This is not observed in steady-state experiments (chapter 3.0, as well as [1, 16]), where  $S_{\text{CO}}$  is typically much higher than  $S_{\text{H}_2}$ . Clearly, the system does not reach thermodynamic equilibrium and the observed selectivities are mainly determined by the reaction kinetics in the system.

To estimate the time-frame necessary for gas phase reactions to approach thermodynamic equilibrium, calculations were performed using the GRI mechanism [47], a well developed mechanism for homogeneous  $\text{C}_1$  reactions. Figure 36 shows  $\text{CH}_4$  and partial as well as total oxidation product concentrations as a function of reactor residence time at  $1200^\circ\text{C}$  (left) and  $900^\circ\text{C}$  (right). An initial gas mixture equal to a typical measured product gas composition of the steady-state conventional process is assumed at  $\tau = 0$  s.

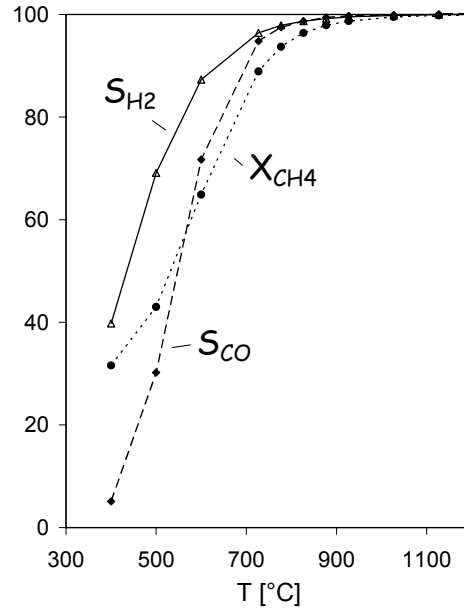


**Figure 35:**  $S_{CO}$  (dashed line),  $S_{H_2}$  (solid line) and  $X_{CH_4}$  (dotted line) in thermodynamic equilibrium for a  $CH_4/O_2$  ratio of 2.0 at different temperatures

At 1200°C,  $H_2$  concentrations increase continuously while  $H_2O$  concentrations decrease within 25 s.  $CO$  concentrations exhibit a minimum and  $CO_2$  a maximum at around 2 s. Methane concentrations show a strong decrease during the first 3 s followed by weak decrease thereafter. Clearly, changing concentrations indicate that equilibrium has not been reached even after a residence time as long as 25 s.

In the case of 900°C, concentration profiles remain flat and do not change noticeably over the course of 25 s. Obviously, the approach towards thermodynamic equilibrium (where  $CO_2$ ,  $H_2O$  and  $CH_4$  concentrations are close to zero) is strongly inhibited by kinetics which indicates that product gas compositions do not change in the inert zone downstream of the catalyst due to homogeneous reactions (where the residence time is typically below 30 ms) in CPOM.

These results are also confirmed by a theoretical investigation by Zhu et al. [48], who compared thermodynamic equilibrium to kinetic calculations using the GRI mechanism. Only for very long residence times (600 s at 1200°C) or extreme temperatures (1500°C), thermodynamic equilibrium compositions could be achieved.

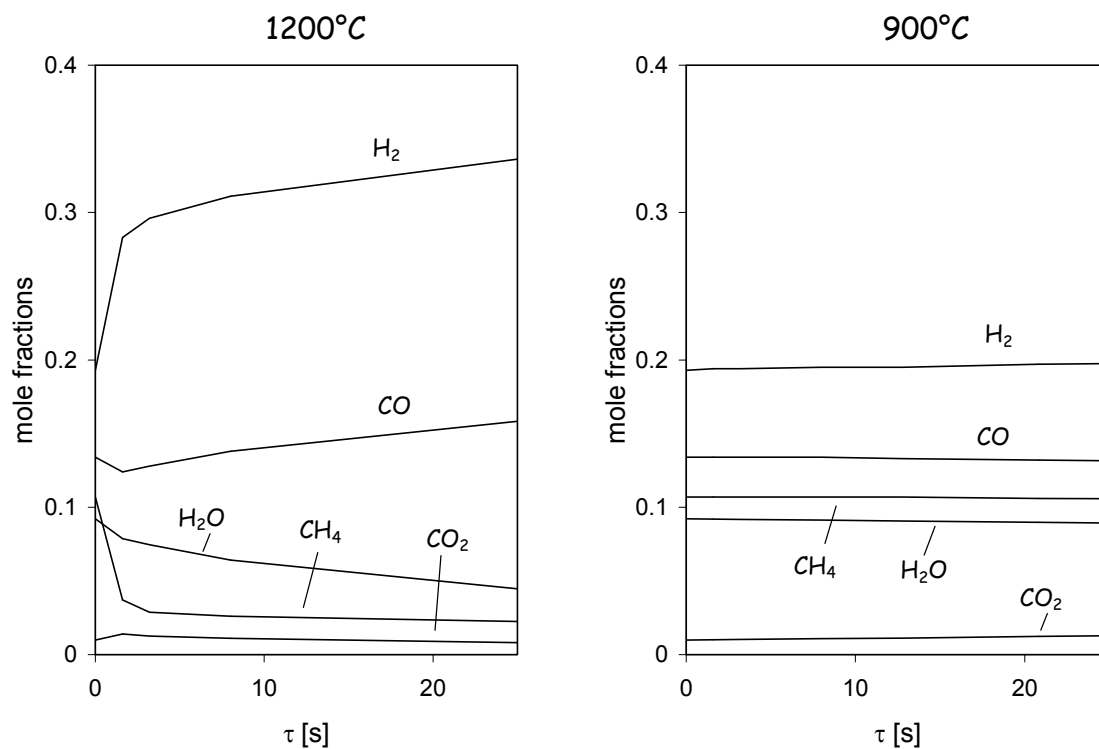


**Figure 36:** Mole fractions of reactants and products in CPOM as a function of residence time at 1200°C (left) and 900°C (right); composition at  $\tau = 0$  s equal to typical product composition measured in CPOM

The results thus suggest that syngas yields could be improved by maintaining temperatures at a very high level and increasing the residence time inside the reactor to enhance reforming reactions. However, the decrease in space-time yields (residence times would have to increase several orders of magnitude compared to CPOM!) as well as the increase in process complexity associated with these changes would destroy the nature of simple, autothermal and efficient CPOM.

Finally, to investigate differences between a purely homogeneous and a catalytic process, we compared results obtained using the GRI mechanism (i.e. homogeneous process) with results of catalytic surface kinetics published by Aghalayam [49]. Figure 37 shows oxygen gas phase



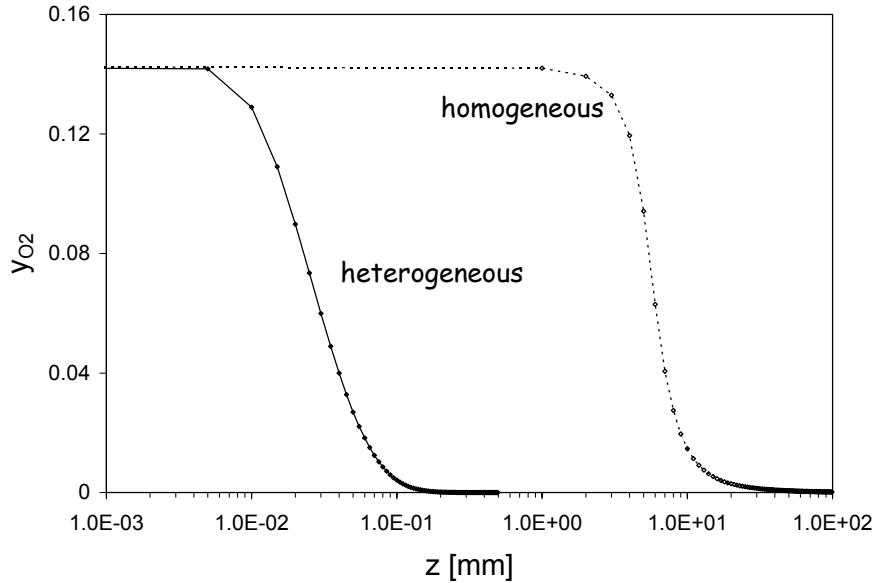


**Figure 37:** Gas phase oxygen mole fractions versus reactor length at  $T = 1000^{\circ}\text{C}$ : heterogeneous (solid line) vs. homogeneous (dashed line) kinetics ( $\text{CH}_4/\text{O}_2 = 2.0$ ,  $\dot{V} = 4\text{slm}$ , steady-state process)

concentrations along the reactor axis for the two cases at a temperature of  $1000^{\circ}\text{C}$  and a  $\text{CH}_4/\text{O}_2$  feed gas ratio of 2.0 (in air). Clearly, the heterogeneous process converts the reactants roughly two orders of magnitude faster than a purely homogeneous process, which shows that surface reactions are necessary for compact and efficient syngas production

To sum up the above discussion, Figure 38 shows a schematic, simplified plot of gas composition vs. temperature. The thermodynamic equilibrium curve is represented by the solid line while the star represents the composition and temperature due to kinetics in CPOM. The position of the star strongly depends on the catalyst material and reactor operation (e.g. conventional vs. RFR). The approach of temperature and composition of the catalytic process towards thermodynamic equilibrium is indicated by the arrows and it is distinguished between adiabatic and non-adiabatic case. At a given temperature, the non-adiabatic approach is shifted towards more total oxidation (lower syngas yields) than the adiabatic case. This occurs due to the fact that temperatures not only decrease due to endothermic reactions (as in the adiabatic case), which result in enhanced compositions, but also due to heat losses. However, the approach

towards equilibrium is obviously very slow and thermodynamic equilibrium can only be reached at very high temperatures and long residence times due to strong kinetic inhibitions, as argued above.

It can thus be summarized that kinetics have on strong influence on overall syngas yields in CPOM, and thermodynamic equilibrium is not reached due to very short residence times.

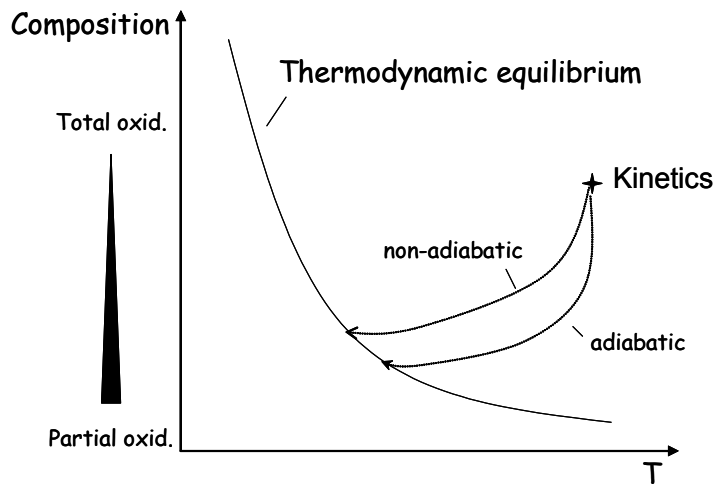


**Figure 38:** Schematic gas-composition vs. temperature diagram: thermodynamic equilibrium and kinetic influence

## 4.0 REACTOR SIMULATION

The experimental investigation of CPOM in an RFR (chapter 3.0) revealed that syngas yields can be strongly improved due to efficient regenerative heat-exchange compared to conventional reactor operation. The general principles governing the reaction and reactor behavior were clearly understood. However, temperature profiles along the catalyst axis cannot be measured experimentally due to the foam structure of the monolith and therefore the influence of dynamic temperature profiles on syngas yields cannot be investigated. Furthermore, a detailed experimental investigation of the surface reaction mechanism under unsteady-state conditions is not possible due to extreme temperatures.

In addition, dynamic reactor operation not only leads to efficient regenerative heat-exchange but also results in an inversion of surface coverages after flow-reversal. It is hypothesized in this work (chapter 2.2.3) that transient surface coverages might lead to a reduction of total oxidation reactions due to dominant carbon coverage on the catalyst surface.

To gain a more thorough understanding of the reaction mechanism of CPOM in an RFR, detailed numerical simulations are thus performed.

### 4.1 Model Validation: Original Reactor Model in Steady-State Operation

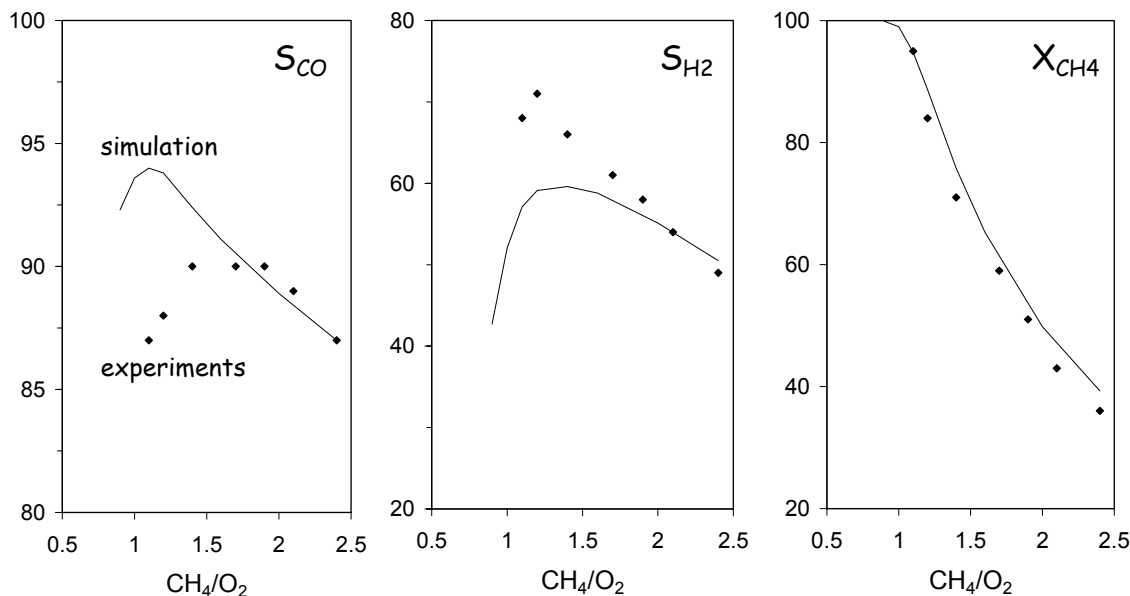
The model initially used for simulating CPOM in a plug-flow reactor was developed in previous studies by Veser et al. [15]. The reactor is modeled by a heterogeneous one-dimensional reaction-dispersion model, and catalytic reactions on the Pt surface are described using elementary step reaction kinetics consisting of 23 individual reaction steps. An in depth description of the model as well as surface kinetics is performed in Appendix F (page 110). This ‘original’ reactor model is in the current work extended by inert zones on either side of the catalyst bed and updated physical properties. To evaluate the model, it is in a first step validated against experimental results of the steady-state process presented in chapter 3.2.

Figure 39 shows partial oxidation selectivities and methane conversions as a function of the  $\text{CH}_4/\text{O}_2$  ratio for experiments (symbols) as well as simulation results (lines) at a flow-rate of 4

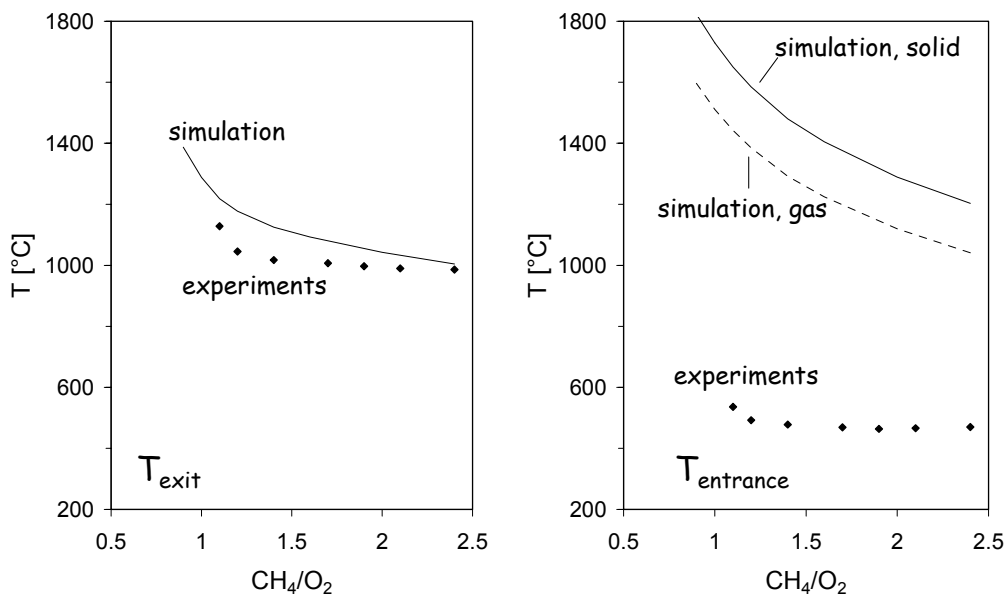
slm. CO selectivities are somewhat overestimated and H<sub>2</sub> selectivities underestimated at fuel lean conditions (CH<sub>4</sub>/O<sub>2</sub> < 1.5). Furthermore, maximum CO selectivities are shifted to lower CH<sub>4</sub>/O<sub>2</sub> ratios in the simulation, while the maximum in S<sub>H<sub>2</sub></sub> is reproduced well. CH<sub>4</sub> conversions agree almost quantitatively. The curves thus generally show a reasonable qualitative agreement which suggests that the major reaction steps are modeled correctly.

Figure 40 shows corresponding catalyst entrance and exit temperatures. While gas and solid phase catalyst entrance temperatures of the simulation are displayed separately, they are identical at the catalyst exit and are therefore shown as a single temperature in the diagram. Taking into account the experimental error, catalyst exit temperatures are reproduced well in the simulation. However, catalyst entrance temperatures differ noticeably and are strongly over predicted in the simulation.

In previous experimental studies, which were the basis for the model used, catalyst entrance temperatures were not measured experimentally and simulation results therefore not validated against this variable. The current results clearly indicate that the model is not capable of



**Figure 39:**  $S_{CO}$  (left),  $S_{H_2}$  (middle) and  $X_{CH_4}$  (right) as a function of the  $CH_4/O_2$  ratio ( $\dot{V} = 4$  slm); experimental data (diamonds) and simulation results (lines, original model)



**Figure 40:** Catalyst exit (left) and entrance (right) temperatures with varying  $\text{CH}_4/\text{O}_2$  ratios ( $\dot{V} = 4 \text{ slm}$ ); experimental data (diamonds) and simulation (lines, original model)

adequately predicting catalyst entrance temperatures as observed experimentally. It is, however, particularly important for a correct simulation of the RFR process that steady-state temperature profiles are modeled precisely. It can be expected that any deviations occurring in the steady-state process will increase even more in the dynamic reactor with integrated heat-exchange.

It is thus necessary to improve the reactor model to fit catalyst entrance temperatures more accurately. A description of the influence of several process parameters onto yields and temperatures as well as evaluation of this improved model is presented in the following chapter.

## 4.2 Model Validation: Improved Reactor Model in Steady-State Operation

Evaluation of the ‘original’ model revealed that while syngas yields and catalyst exit temperatures of the steady-state process agree reasonably well with experimental data, catalyst entrance temperatures are strongly overestimated. It must thus be the objective to better fit catalyst entrance temperatures of the simulation to experimental data by improving reactor

parameters, but at the same time keep yields and catalyst exit temperatures constant. Due to highly temperature dependent reaction selectivities in CPOM, however, it can be expected that a change in temperature profile will most probably also have a strong effect on overall yields. This interaction emphasizes the complexity of the problem: a reactor parameter cannot be varied without influencing the whole system, i.e. temperatures and yields. It is therefore likely that several parameters (which interact with each other) have to be improved.

In addition to reactor parameters, kinetic rate parameters have to be adjusted. Lowering catalyst entrance temperatures by enhancing the reactor model will, using unchanged kinetics, result in decreased syngas yields (since total oxidation is favored at lower temperatures). The only way to combine lowering temperatures while keeping yields constant is by simultaneously adjusting rate parameters. This adjustment is complex, since 23 individual reaction steps describe the system and extend the range of variable parameters considerably.

An in depth analysis of the system revealed that the reactor model can be improved by implementing external mass transfer into the simulation. Mass transfer may not be neglected as was the case in the original model and has a strong influence on temperatures and yields. Additionally, the specific surface area of the catalyst was adjusted. However, improvement of these parameters resulted in an unsatisfactory agreement of syngas yields in comparison to experimental data. Hence, reaction rate parameters were adjusted within strict boundaries until a satisfactory agreement was obtained. A detailed description of the changes made to the reactor model and kinetic rate parameters is given in Appendix G (page 116).

Using this improved reaction and reactor model, the simulation is again validated against experimental results of the steady-state process.

Figure 41 shows partial oxidation selectivities and methane conversions as a function of the  $\text{CH}_4/\text{O}_2$  ratio for experiments (dots) as well as simulation data (lines). CO selectivities are reproduced well and exhibit a maximum error of about 5 % at low  $\text{CH}_4/\text{O}_2$  ratios.  $\text{S}_{\text{H}_2}$  is underestimated at high  $\text{CH}_4/\text{O}_2$  ratios by as much as 10 % but shows a very good qualitative agreement. The maxima in syngas selectivities observed experimentally are also reproduced well.  $\text{CH}_4$  conversions show a quantitative agreement at high  $\text{CH}_4/\text{O}_2$  ratios and are over-predicted in the simulation at fuel lean conditions by as much as 10-15 %. Even though quantitative differences between simulation and experimental results exist, the curves show a

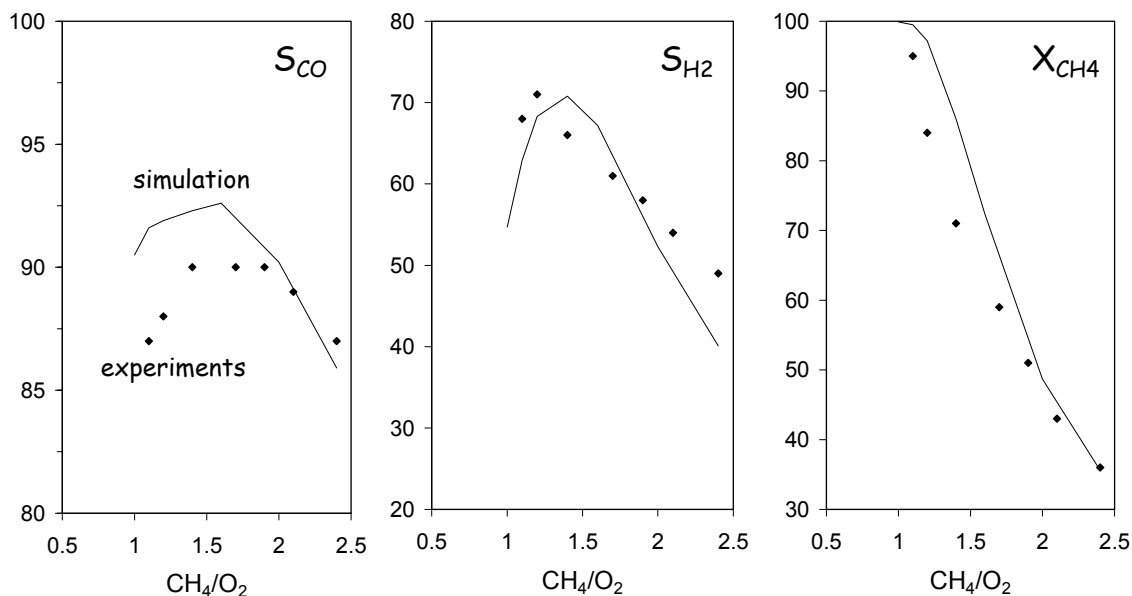


**Figure 41:**  $S_{CO}$  (left),  $S_{H_2}$  (middle) and  $X_{CH_4}$  (right) as a function of  $CH_4/O_2$  ratio ( $\dot{V} = 4$  slm); experiments (dots) and simulation (lines, improved reactor model) results in steady-state reactor operation

very good qualitative agreement and are significantly improved in comparison to the original model (see Figure 39). Obviously, changes made to the reactor model improved the validity of the model.

Corresponding catalyst exit and entrance temperatures are shown in Figure 42. Simulated temperatures increase continuously with decreasing  $CH_4/O_2$  ratios and do not show the plateau like behavior observed experimentally over a broad range of  $CH_4/O_2$  ratios. Catalyst exit temperatures are slightly under-predicted at high  $CH_4/O_2$  ratios but generally show a semi-quantitative agreement over the range of  $CH_4/O_2$  ratios investigated. Catalyst entrance temperatures are still somewhat over-predicted in the simulation. They are, however, much lower than in the original model (compare to Figure 40). While in the original model deviations (between experiments and simulated gas phase temperatures) ranged from 600°C at high  $CH_4/O_2$  ratios to above 1000°C at lower  $CH_4/O_2$  ratios, catalyst entrance temperatures are strongly reduced in the improved reactor model where deviations range from less than 100°C at high  $CH_4/O_2$  ratios to slightly above 300°C at lower  $CH_4/O_2$  ratios.

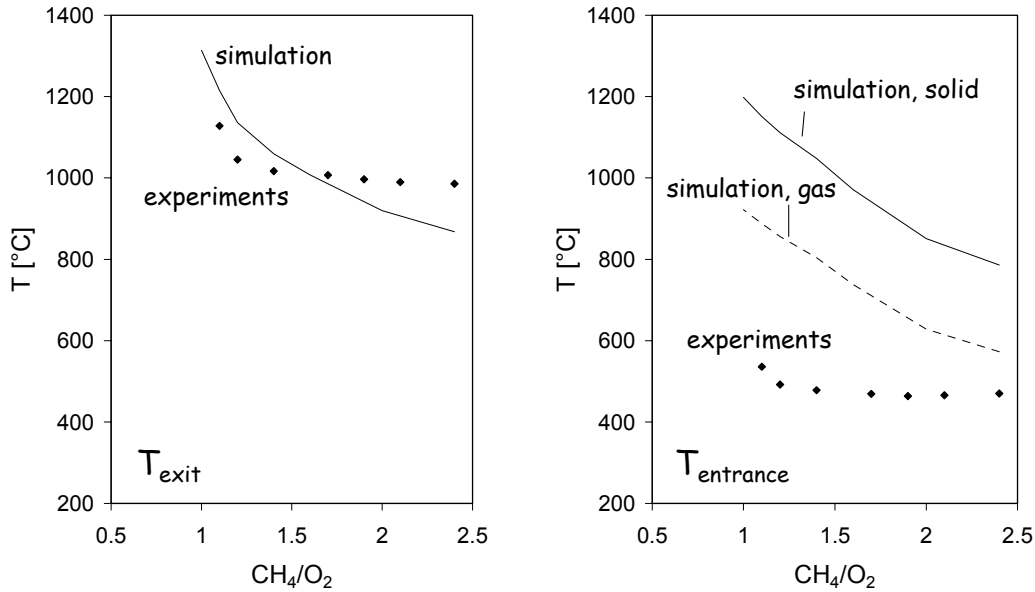


**Figure 42:** Catalyst exit (left) and entrance (right) temperatures as a function of  $CH_4/O_2$  ratio ( $\dot{V} = 4$  slm); experiments (dots) and simulation (lines, improved reactor model) results in steady-state reactor operation

Improvements made to the reactor model as well as adjusted reaction rate parameters thus result in a much better agreement of yields and temperatures between experimental and simulated data compared to the original model for a variation of the  $CH_4/O_2$  ratio.

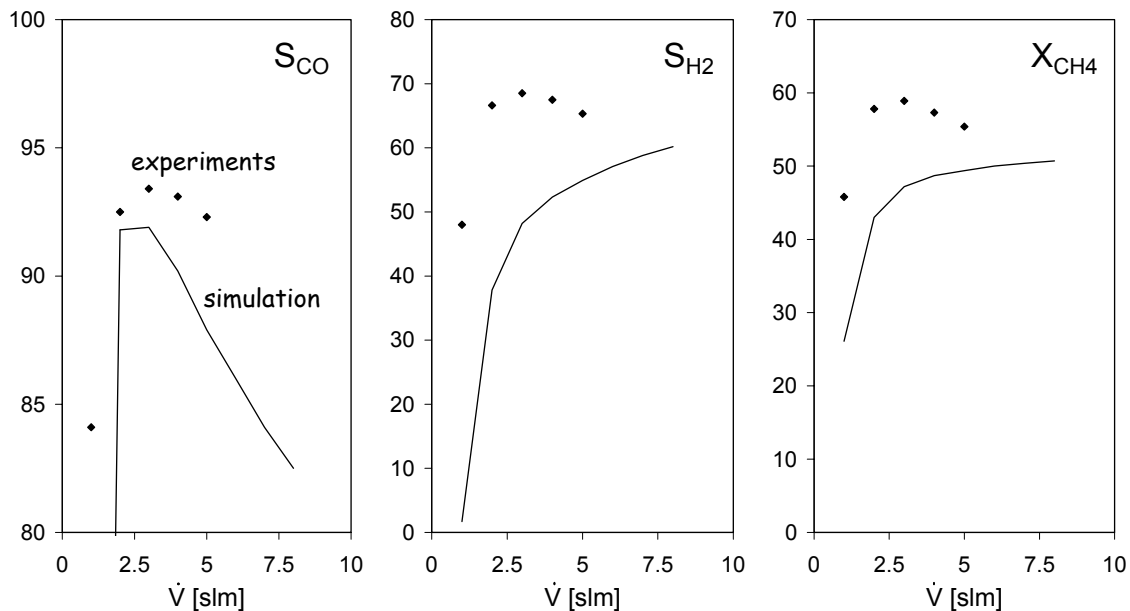
In addition to a variation of  $CH_4/O_2$  ratios, the model is also validated against experimental results for varying flow-rates at steady-state conditions. Figure 43 shows syngas selectivities and methane conversions as a function of the flow-rate.  $S_{CO}$  shows a good qualitative agreement between simulation and experimental data. The experimentally observed maximum at a flow-rate of 3 slm as well as the strong decrease towards lower and less pronounced decrease towards higher flow-rates is reproduced. However,  $S_{H_2}$  and  $X_{CH_4}$  differ qualitatively and quantitatively from experiments over the whole range of flow-rates. The simulation results do not exhibit the experimentally observed maximum at 3 slm but instead increase continuously with higher flow-rates.



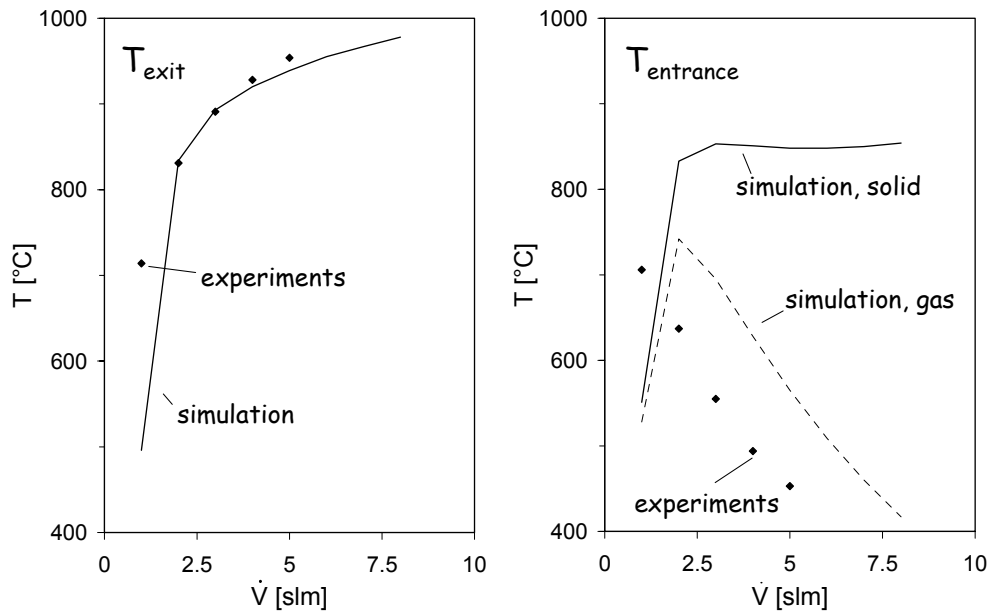
The fact that a variation of the flow-rate results in distinct qualitative differences between simulation and experimental data shows that the reactor model is still missing some essential features of the experimental system.

Figure 44 shows catalyst exit and entrance temperatures as a function of the flow-rate for conventional reactor operation. The experimentally observed trend of continuously increasing catalyst exit temperatures with higher flow-rates (left graph) is reproduced in the simulation almost quantitatively. Gas phase catalyst entrance temperatures (right graph) are about 100°C too high compared to experimental data and show a good qualitative agreement for flow-rates above 2 slm. In contrast, solid phase catalyst entrance temperatures exhibit a strong increase between 1 and 2 slm and remain constant for flow-rates higher than 2 slm.

The experimentally observed temperature decrease at the catalyst entrance with increasing flow-rates explained decreasing syngas yields at high flow-rates (see chapter 3.2.4). While simulated gas phase temperatures show a similar behavior at the catalyst entrance with increasing flow-rates, solid phase temperatures show a different qualitative behavior and remain



**Figure 43:**  $S_{CO}$  (left),  $S_{H_2}$  (middle) and  $X_{CH_4}$  (right) as a function of the flow-rate ( $CH_4/O_2 = 2.0$ ); comparison between experiments (dots) and simulation results (improved model, lines)



**Figure 44:** Catalyst exit (left) and entrance (right) temperatures as a function of the flow-rate ( $\text{CH}_4/\text{O}_2 = 2.0$ ); experiments (dots) and simulation (improved model, lines)

almost constant. The fact that surface kinetics are influenced by the temperature of the solid and not the gas phase explains the observed qualitative differences in syngas yields (Figure 43) with a variation of the flow-rate.

A potential reason for the dissatisfactory modeling of the monolith with a variation of the flow-rate might be the fact that a simplified, one-dimensional model is used which is not capable of adequately reproducing all decisive (particularly entrance) effects. Furthermore, the inert zone and catalyst bed are treated in the model as a single piece of monolith with different physical properties. Experimentally, however, the interface between the two monoliths is much more complex, and heat-transfer between the two may not be described adequately in the model.

However, at a flow-rate of 4 slm, a variation of the  $\text{CH}_4/\text{O}_2$  ratio gives a qualitative agreement between experiments and simulation so that for these conditions the major reaction steps are described with satisfactory accuracy.

Keeping the described limitations of the model in mind, evaluation of the model validity is in the following chapter extended and dynamic reactor operation investigated.

### 4.3 Model Validation: Improved Reactor Model in Dynamic Reactor Operation

Evaluation of the improved model in steady-state reactor operation (chapter 4.2) revealed that at a flow-rate of 4 slm and varying  $\text{CH}_4/\text{O}_2$  ratios, syngas yields and catalyst temperatures show a good qualitative agreement with experimental data. However, variation of flow-rate at a constant  $\text{CH}_4/\text{O}_2$  ratio results in qualitative differences between experiment and simulation which suggests that some features of the monolithic reactor are not modeled adequately yet. To further evaluate the model validity, simulation and experimental data obtained in dynamic RFR operation at a flow-rate of 4 slm are compared in the following.

Figure 45 shows mean syngas selectivities and methane conversions as a function of the  $\text{CH}_4/\text{O}_2$  ratio at a flow-rate of 4 slm and a semi-cycling period of 15 s. Simulated CO selectivities differ by about 2-5 % to experimental data and show a more or less flat curve over the  $\text{CH}_4/\text{O}_2$  range investigated as observed experimentally.  $\text{H}_2$  selectivities remain constant at  $\text{CH}_4/\text{O}_2$  ratios

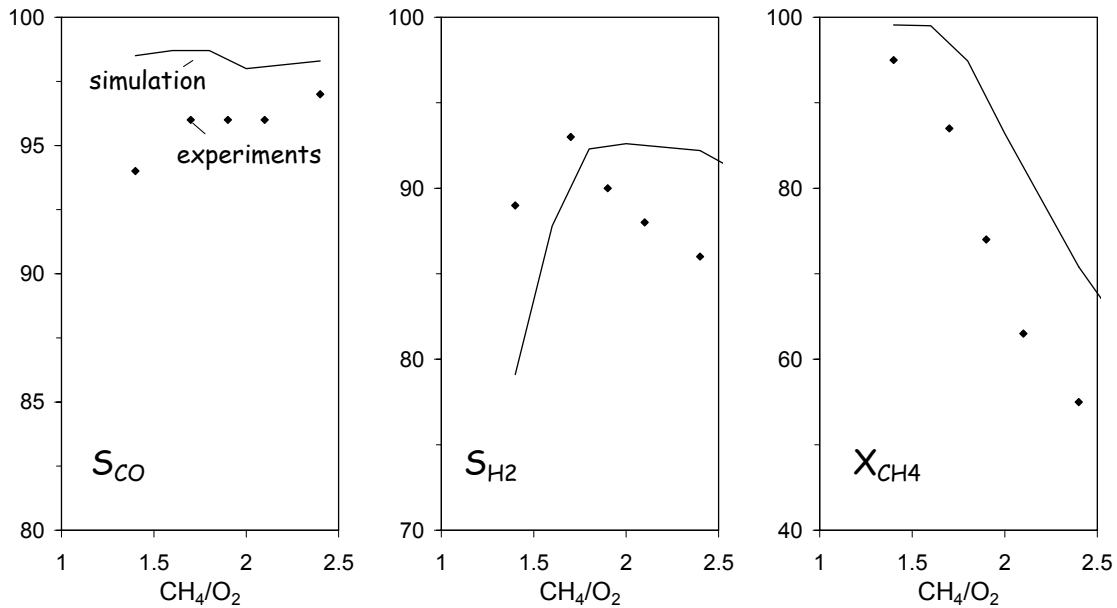


**Figure 45:**  $S_{\text{CO}}$  (left),  $S_{\text{H}_2}$  (middle) and  $X_{\text{CH}_4}$  (right) as a function of the  $\text{CH}_4/\text{O}_2$  ratio in dynamic reactor operation ( $\dot{V} = 4$  slm,  $\tau/2 = 15$  s); comparison between experiments (dots) and simulation (lines, improved model)

larger than 1.8 in the simulation and show a sharp decrease towards smaller  $\text{CH}_4/\text{O}_2$  ratios, while experimental results show a maximum at a  $\text{CH}_4/\text{O}_2$  ratio of 1.7 with decreasing values towards higher and lower  $\text{CH}_4/\text{O}_2$  ratios. However, quantitative differences stay below 10 %. Methane conversions agree qualitatively but are overestimated by as much as 15 % at high  $\text{CH}_4/\text{O}_2$  ratios in the simulation.

A reasonable qualitative agreement is observed between mean selectivities and conversions with varying  $\text{CH}_4/\text{O}_2$  ratios in dynamic reactor operation.

Mean catalyst entrance and exit as well as maximum (at the catalyst entrance and exit) temperatures in RFR operation with varying  $\text{CH}_4/\text{O}_2$  ratios for simulation and experiments are shown in Figure 46. The curves show a similar behavior as in steady-state reactor operation. While in steady-state operation, catalyst entrance temperatures were overestimated by 100-300°C (Figure 42), the heat-integration in RFR operation leads to a further increase in temperature differences compared to experimental data. Differences range from 200-300°C at high  $\text{CH}_4/\text{O}_2$  ratios to above 600°C at low  $\text{CH}_4/\text{O}_2$  ratios.

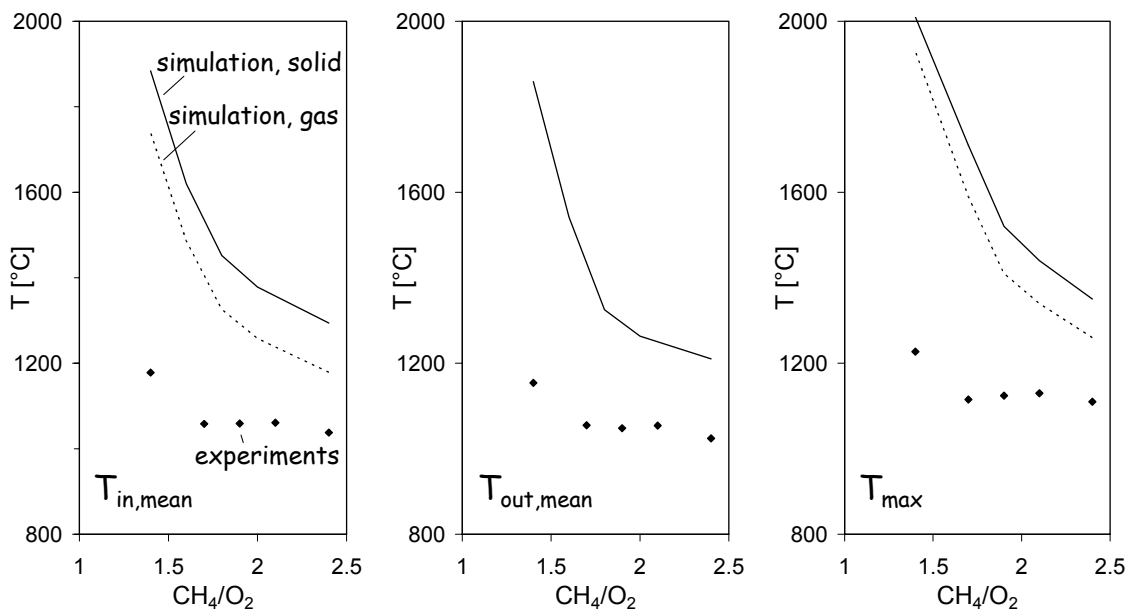


**Figure 46:** Mean catalyst entrance (left) and exit (middle) as well as maximum (at catalyst entrance/exit, right) temperatures as a function of the  $\text{CH}_4/\text{O}_2$  ratio in RFR operation ( $\dot{V} = 4$  slm,  $\tau/2 = 15$  s); experiments (dots) and simulation (lines, improved model)

We observe that while noticeable quantitative differences in mean yields and temperatures exist between experimental and simulation results with varying  $\text{CH}_4/\text{O}_2$  ratios, a rough qualitative agreement in dynamic RFR operation is observed.

The comparison of mean temperatures and yields of the dynamic process performed above allows to evaluate the validity of general characteristics of the model (e.g. global kinetics). However, to draw reliable conclusions about dynamic properties in the RFR, it is necessary to additionally compare time dependent progression of temperatures and concentrations during a semi-cycle.

A comparison between time-dependent temperatures for simulation (left, gas phase temperatures) and experiments (right) is shown in Figure 47. Solid phase temperatures of the simulation are not shown but qualitatively show the exact same behavior as gas phase temperatures only shifted  $\sim 200^\circ\text{C}$  higher. The graphs show the development of catalyst entrance and exit temperatures during four semi-cycles at a  $\text{CH}_4/\text{O}_2$  ratio of 2.0, a flow-rate of 4 slm and a semi-cycle periodicity of 15 s. In the first and third semi-cycle, the solid line represents catalyst

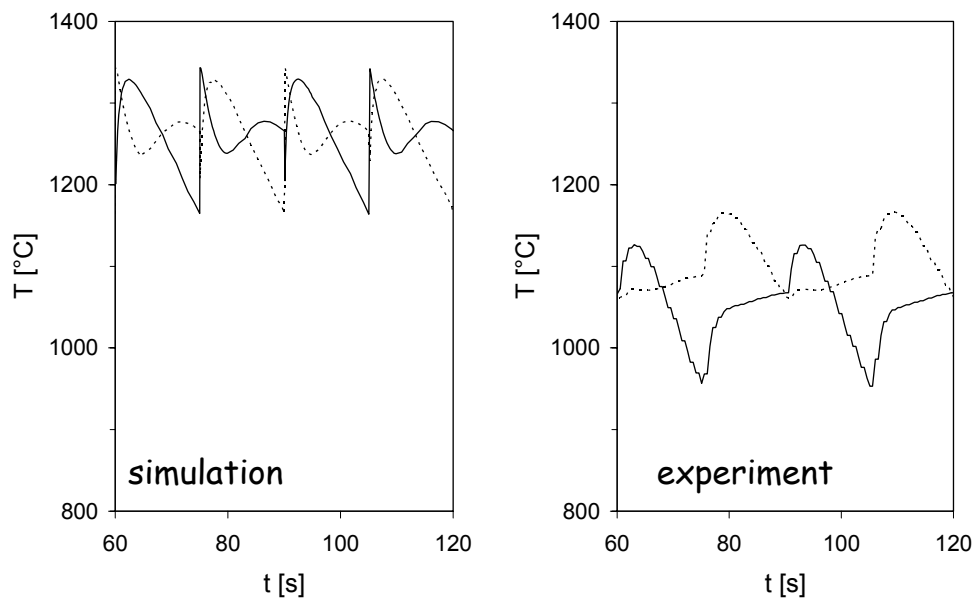


**Figure 47:** Time dependent temperatures measured on either side of the catalyst bed; left: simulation (improved model), right: experiment;  $\text{CH}_4/\text{O}_2 = 2.0$ ,  $\tau/2 = 15$  s,  $\dot{V} = 4$  slm

entrance temperatures while the dashed line represents exit temperatures and vice versa in semi-cycles two and four (for details see also chapter 3.2.1).

Catalyst entrance temperatures show a maximum at 3 s into the semi-cycle, followed by a pronounced decrease during the rest of the semi-cycle. Simulated entrance temperatures show a very good qualitative agreement with these main features of the experimental data but are shifted towards higher temperatures.

Catalyst exit temperatures on the other hand show a markedly different behavior in comparison with experiments. While the experimental curve is characterized by an initial increase followed by a flat temperature plateau during most of the semi-cycle, simulation results show a pronounced peak immediately after flow-reversal followed by an S-shaped curve. As will be shown in chapter 4.4.2, the temperature spike is the result of a heat-wave pushed out of the catalyst bed after flow-reversal. The heat-source corresponds to the reaction front of the preceding semi-cycle. The fact that this spike is not observed in the experiment can potentially be due to the following: a) The response time of the thermocouple to the extreme temperature jump is too slow so that the peak is not resolved; furthermore the thermocouple might not be positioned exactly at the catalyst exit; or b) The reaction front is positioned further inside the catalyst bed in the experiment, so that it takes a longer time for the heat-wave to exit the reactor after flow-reversal. Since a larger part of the catalyst bed is heated up by this heat-wave, no temperature spike is observed at the catalyst exit. The fact that catalyst entrance temperatures in steady-state operation are generally over-predicted in the simulation compared to experiments (Figure 42) does indeed suggest that the reaction front is located closer to the front edge of the catalyst bed in the simulation. However, due to the foam structure of the catalyst, an experimental test of this hypothesis is not possible.

The progression of catalyst entrance temperatures during a semi-cycle agree well qualitatively which suggests that dynamic regenerative heat-exchange is modeled accurately.

In addition to temperatures, time-dependent concentrations are measured experimentally at the outlet of the reactor using an MS. The MS used does not allow to measure concentrations quantitatively, so that a comparison to simulated results can only be performed qualitatively.

Figure 48 shows time dependent H<sub>2</sub> (top), H<sub>2</sub>O, CH<sub>4</sub>, CO<sub>2</sub> and CO (bottom) concentrations at the outlet of the reactor for simulation (left, mole fractions) and experiments (right,

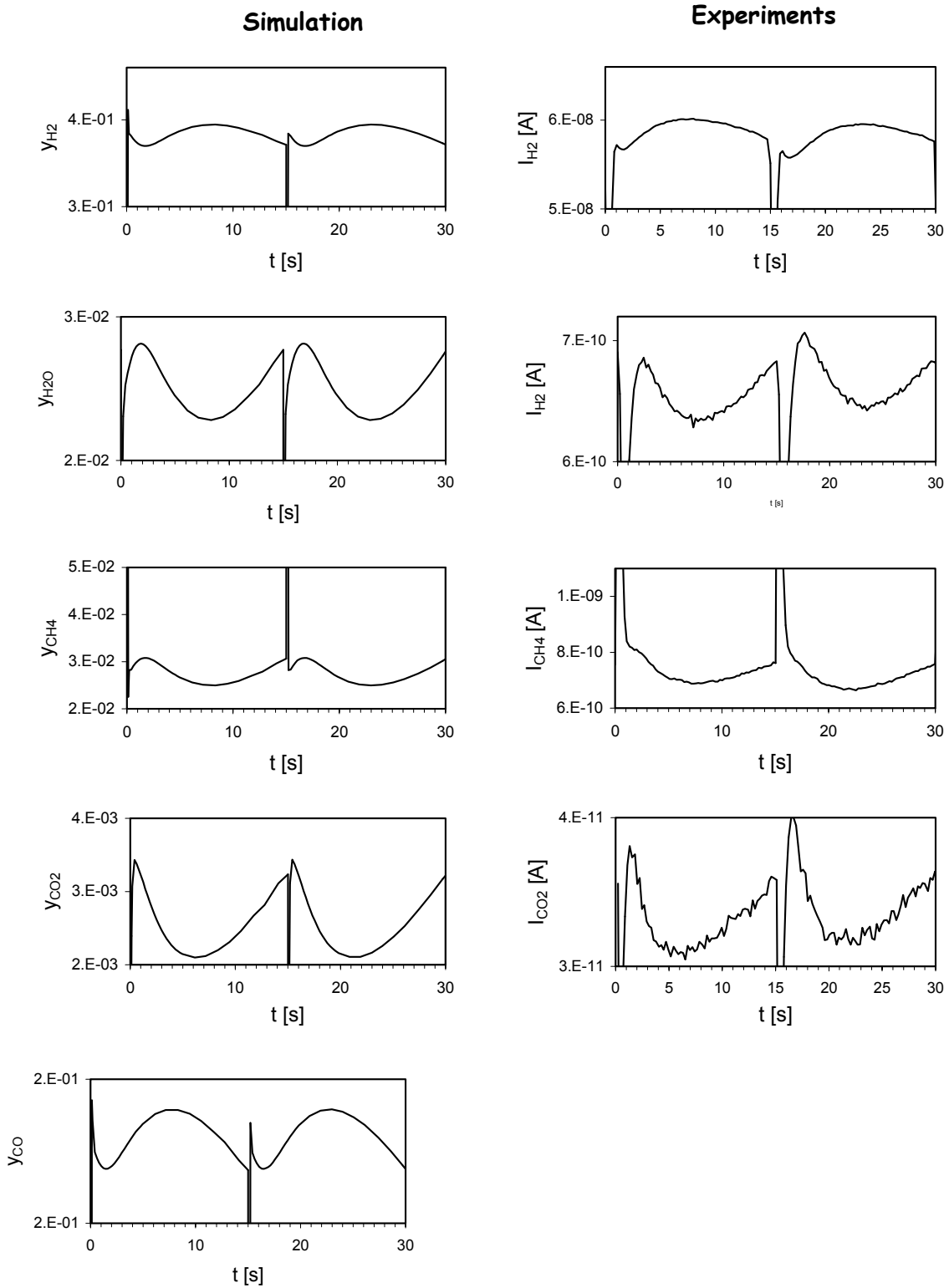


**Figure 48:** Time dependent  $H_2$  (top),  $H_2O$ ,  $CH_4$ ,  $CO_2$  and  $CO$  (bottom) concentrations measured at the reactor exit during 2 semi-cycles; comparison between simulation (left, improved model) and experiment (right);  $CH_4/O_2 = 2.0$ ,  $\tau/2 = 15$  s,  $\dot{V} = 4$  slm

concentrations measured in current [A]) for a  $\text{CH}_4/\text{O}_2$  ratio of 2.0, a flow-rate of 4 slm and a semi-cycle periodicity of 15 s. The graphs show concentration curves during two semi-cycles. Experimental CO concentrations are not shown since in MS spectra,  $\text{N}_2$  (same mass ( $m^+ 28$ ) as CO) interferes with CO and thus CO concentrations cannot be determined.

Partial oxidation concentrations show an initial drop to zero immediately after flow-reversal, which occurs due to back-flushing of reactants positioned in the inert zone upstream of the catalyst. The drop is directly followed by a peak. Thereafter, a broad maximum appears with a peak at 8 s into the semi-cycle.  $\text{H}_2\text{O}$  concentrations are characterized by an initial drop to zero, followed by a peak at 2 s into the semi-cycle and a broad, concave curve with a minimum at 8 s into the semi-cycle.  $\text{CH}_4$  concentrations show a similar behavior to the  $\text{H}_2\text{O}$  curves. However, back-flushing of reactants after flow-reversal results in a sharp peak in  $\text{CH}_4$  concentrations rather than a drop to zero as observed for product gases.  $\text{CO}_2$  concentrations are characterized by the initial drop to zero, which is followed by a broad convex curve with a minimum around 6 s into the semi-cycle. The minimum appears somewhat earlier than the minimum observed in  $\text{CH}_4$  and  $\text{H}_2\text{O}$  or the maximum observed in  $\text{H}_2$  concentrations.

Experimental concentration curves generally show some time-delay as well as additional dispersion effects compared to the simulation. These occur since the MS capillary is not positioned exactly at the outlet of the reactor but further downstream (see Figure 7). Furthermore, the frequency with which the MS records data is limited to roughly 4.5 Hz, so that very fast changes in gas concentrations may not be resolved.

Nevertheless, an excellent qualitative agreement is observed between simulated and experimental curves. Maxima and minima appear at identical times within a semi-cycle. This at first seems somewhat surprising, since the qualitative agreement of global yields and temperatures with varying  $\text{CH}_4/\text{O}_2$  ratios is not as good (Figure 45). However, concentration curves at the reactor exit are a direct result of dynamic temperature profiles in the RFR, so that the excellent agreement clearly indicates that heat-integration and major reaction steps are modeled accurately.

The model can thus be used to investigate the reaction mechanism during dynamic reactor operation in detail. Results are presented in the following chapter.



## 4.4 Reaction Mechanism during Dynamic Reactor Operation

Extreme temperatures result in very low surface coverages (except for C) and make an experimental investigation of surface reactions impossible. Furthermore, the foam structure of the monolithic catalyst does not allow measurement of temperature profiles inside the reaction zone. However, dynamic temperature profiles and possibly transient surface coverages during RFR operation are responsible for the observed increase in syngas yields. To truly understand and potentially enhance reactor operation further, it is necessary to identify how RFR operation increases syngas yields. This is performed in the following using the model described above.

The reactions occurring during a semi-cycle under unsteady-state conditions can generally be divided into two parts: an initial, short period where products from the previous semi-cycle - positioned in the inert zone upstream of the catalyst - are led through the catalyst, followed by a period (for the remaining part of the semi-cycle) where reactants enter the catalyst bed and concentrations as well as temperatures are influenced by dynamic regenerative heat-exchange. The two periods are investigated separately in chapters 4.4.1 and 4.4.2.

### 4.4.1 Reaction Mechanism during Initial Phase after Flow-Reversal

In a technical RFR system, a so-called flushing phase with an inert gas prior to every flow-reversal is used to flow reactants positioned in the inert zone upstream of the catalyst bed through the reaction zone. In this way, reactants are prevented from exiting the system after flow-reversal. While flushing phases can be very important, e.g. if one of the reactants of the RFR process is a poison for a catalyst used in a downstream process, they also add complexity to the system and reduce production efficiency.

In the present RFR setup, no flushing phase is included and small amounts of reactants exit the system immediately after every flow-reversal. Furthermore, products positioned downstream of the reaction zone flow through the catalyst bed after every flow-reversal, as schematically shown in Figure 49.

To investigate these processes in detail, Figure 50 shows the progression of partial and total oxidation product as well as  $\text{CH}_4$  and  $\text{O}_2$  concentrations at the outlet of the reactor during initial

0.3 s after flow-reversal. The concentration curves can be divided into 3 phases: an initial phase (I), where product concentrations are zero while reactant concentrations exhibit a constant high value, a second phase (II), where product concentrations increase and exhibit a maximum while methane concentrations show a minimum and O<sub>2</sub> concentrations drop to zero, and a final phase (III), where partial oxidation concentrations decrease, total oxidation concentrations increase and CH<sub>4</sub> and O<sub>2</sub> concentrations remain constant.

In phase I, unconverted reactants positioned in the inert zone downstream of the catalyst are flushed out of the system. At a flow-rate of 4 slm, an inert zone length of 11 cm and 1.7 cm diameter and a temperature of ~850°C this phase (i.e. phase I) takes about 0.08 s, as observed in Figure 50. In the following 0.08 s (phase II), product gases positioned upstream of the catalyst bed flow through the reaction zone before fresh reactants enter the catalyst bed in phase III.

The fact that partial oxidation concentrations are higher in phase II than in phase III, while at the same time total oxidation concentrations are lower in phase II than in phase III and methane concentrations proceed through a minimum indicates that reforming reactions take place in phase II.

To investigate the reaction mechanism in phase II in more detail, Figure 51 shows partial and total oxidation product concentrations along the center portion of the reactor (catalyst positioned between 110 < z < 120 mm) during the first 0.2 s after flow-reversal. To emphasize decisive effects, concentration axes (i.e. z-axes) only show upper limits of the concentrations.

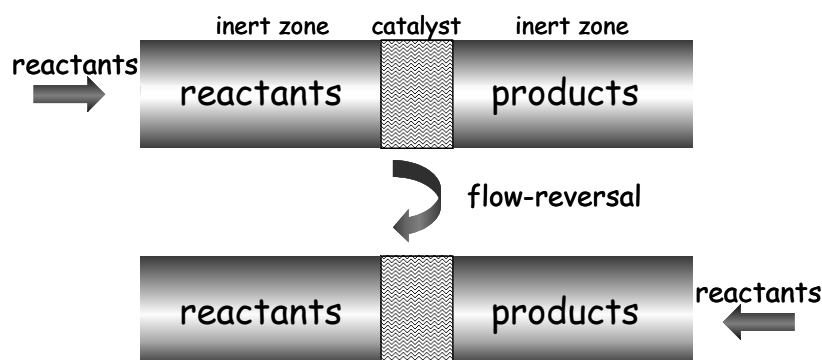


**Figure 49:** Schematic of gas accumulations during initial phase after flow-reversal

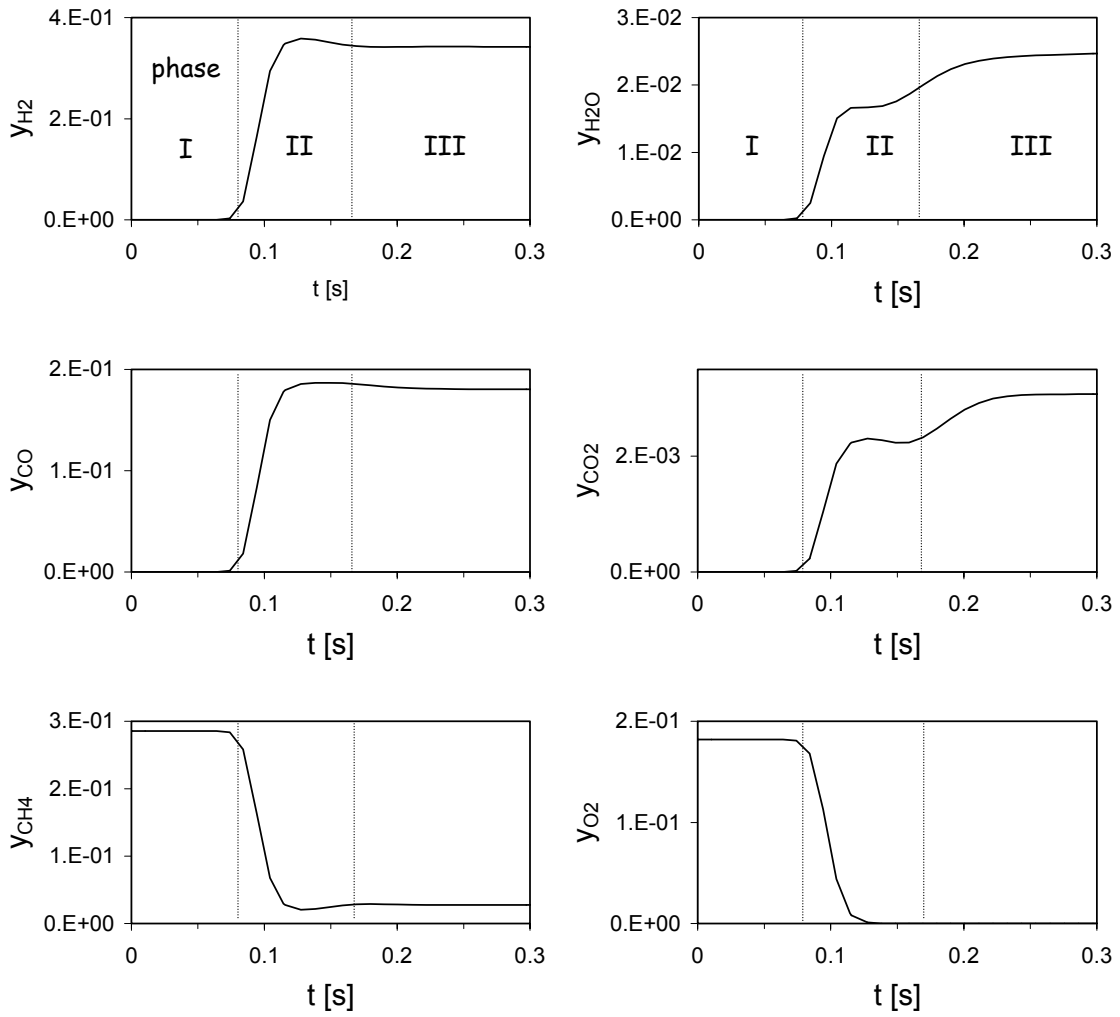


**Figure 50:** Partial and total oxidation product as well as  $\text{CH}_4$  and  $\text{O}_2$  concentrations at the reactor exit during initial 0.3 s after flow-reversal using improved reactor model ( $\text{CH}_4/\text{O}_2 = 2.0$ ,  $\tau/2 = 15$  s,  $\dot{V} = 4$  slm)

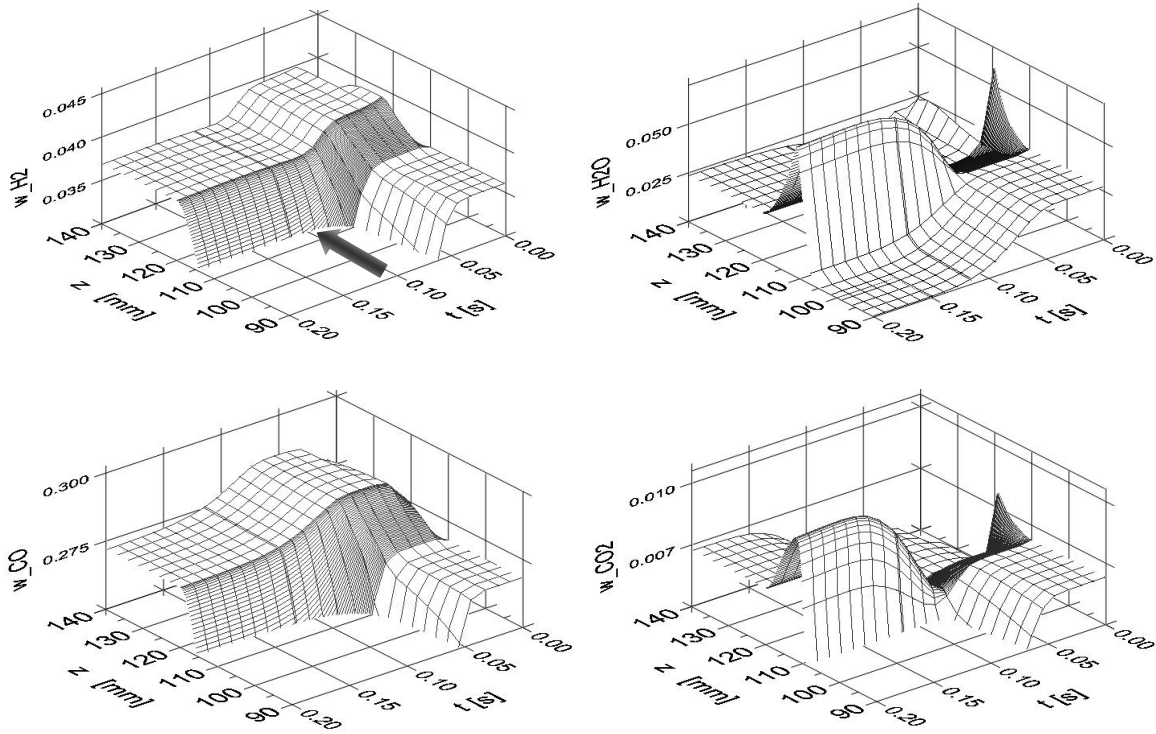


**Figure 51:** Partial (left) and total (right) oxidation product concentrations along the center portion of the reactor (catalyst between  $110 < z < 120$  mm, dark) during initial 0.2 s after flow-reversal (improved reactor model); flow-direction indicated by arrow ( $CH_4/O_2 = 2.0$ ,  $\tau/2 = 15$  s,  $\dot{V} = 4$  slm)

During the first 0.08 s, products positioned in the inert zone upstream of the catalyst bed ( $0 < z < 110$  mm) flow through the catalyst. Within this period,  $H_2$  and CO concentrations increase further (i.e. to values above the initial product gas composition) in the region of the catalyst (a step is observed), while  $H_2O$  and  $CO_2$  concentrations decrease. Once the inert zone upstream of the catalyst is completely flushed with reactants ( $t > 0.08$  s), syngas concentrations at the catalyst exit decrease (as compared to when products flow through the catalyst) while total oxidation product concentrations increase.

Concentration profiles therefore indicate that during the initial phase after flow-reversal, when product gases are led through the catalyst bed, syngas yields are increased. Because no oxygen is present in the gas phase at that time, this can only occur due to endothermic  $H_2O$  and  $CO_2$

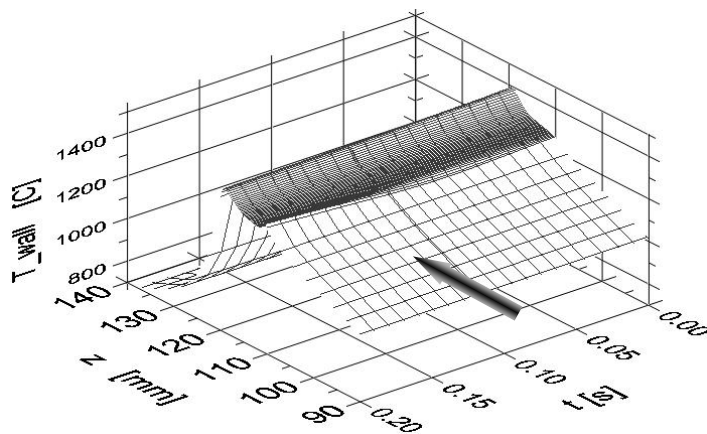


**Figure 52:** *Temperature profiles along the center portion of the reactor (catalyst between  $110 < z < 120$  mm, dark) during initial 0.2 s after flow-reversal (improved reactor model), flow-direction indicated by arrow;  $CH_4/O_2 = 2.0$ ,  $\tau/2 = 15$  s,  $\dot{V} = 4$  slm*

reforming reactions. Temperature profiles shown in Figure 52 indicate that advantageous temperature profiles, particularly high temperatures at the catalyst exit, are beneficial for these endothermic reactions.

The gases exit the reactor between 0.08 and 0.15 s after flow-reversal and result in the observed maximum in CO and H<sub>2</sub> as well as the minimum in CH<sub>4</sub> concentrations in Figure 50.

From these results it could be expected that increasing the catalyst bed length should lead to increased syngas yields, since product gases are converted further when they are led over the catalyst bed again. In steady-state operation, however, increasing the catalyst bed length does not lead to increased syngas yields. Additional endothermic reactions can hence only occur due to advantageous temperature profiles in RFR operation for a short period of time.

Following the initial back-flushing phase, reactants enter the catalyst bed. The reaction mechanisms occurring during this major part of the semi-cycle are investigated in the next chapter.

#### 4.4.2 Reaction Mechanism during Second Part of a Semi-Cycle

After the initial 0.2 s, where product gases are flushed through the catalyst bed (chapter 4.4.1), fresh reactants ( $\text{CH}_4$  and air) enter the catalyst bed for the remaining part of the semi-cycle. Dynamic temperature profiles along the reactor axis determine the reaction mechanisms during this period.

While Figure 48 showed the progression of product and reactant concentrations at the reactor exit in dynamic reactor operation, Figure 53 shows the progression of  $\text{H}_2$  as well as  $\text{CO}$  selectivities during two semi-cycles.

Since  $\text{H}_2$  and  $\text{H}_2\text{O}$  are the only H-containing product species in the system,  $\text{H}_2$  selectivities can be expressed by  $S_{\text{H}_2} = y_{\text{H}_2}/(y_{\text{H}_2}+y_{\text{H}_2\text{O}})$ . Since maxima in  $\text{H}_2\text{O}$  concentrations appear at the same time as  $\text{H}_2$  minima and vice versa (Figure 48),  $\text{H}_2$  selectivities qualitatively show the same curve as  $\text{H}_2$  concentrations. The same is valid for  $S_{\text{CO}}$ . However, minimum  $\text{CO}_2$  concentrations

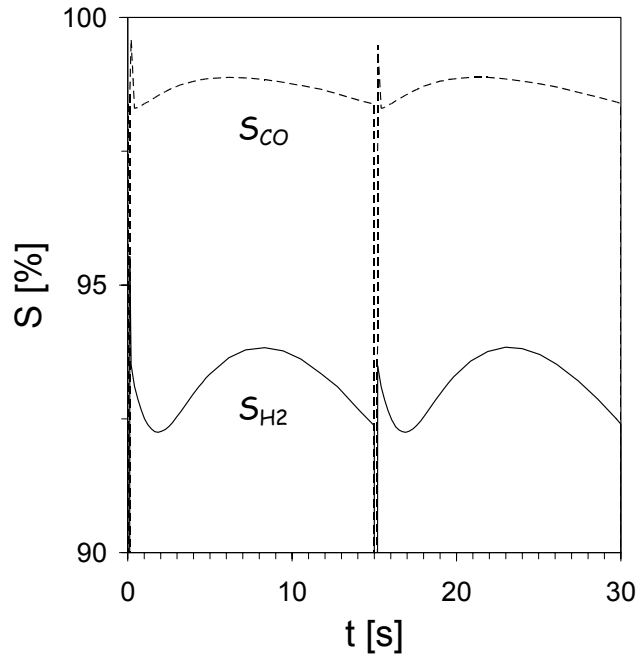


**Figure 53:** Syngas selectivities at the reactor exit during two semi-cycles;  $\text{CH}_4/\text{O}_2 = 2.0$ ,  $\tau/2 = 15$  s,  $\dot{V} = 4$  slm (calculated using improved reactor model)

appear at 6 s into the semi-cycle while maximum CO concentrations appear at 8 s into the semi-cycle. Hence, maximum  $S_{CO}$  appear at around 7 s into the semi-cycle and is thus slightly shifted compared to maximum  $S_{H_2}$ . The curves suggest that optimum conditions in a semi-cycle exist around 7 s into the semi-cycle for  $S_{CO}$  and around 8 s for  $S_{H_2}$ . This implies that optimum temperature profiles are different for maximum  $S_{CO}$  and  $S_{H_2}$ . To investigate the influence of dynamic temperatures on concentration profiles, concentration and temperature profiles along the reactor axis during a semi-cycle are compared in the following.

Figure 54 shows partial and total oxidation product concentration profiles along the catalyst axis  $z$  during one semi-cycle of 15 s at a constant  $CH_4/O_2$  ratio of 2.0 and a flow-rate of 4 slm.

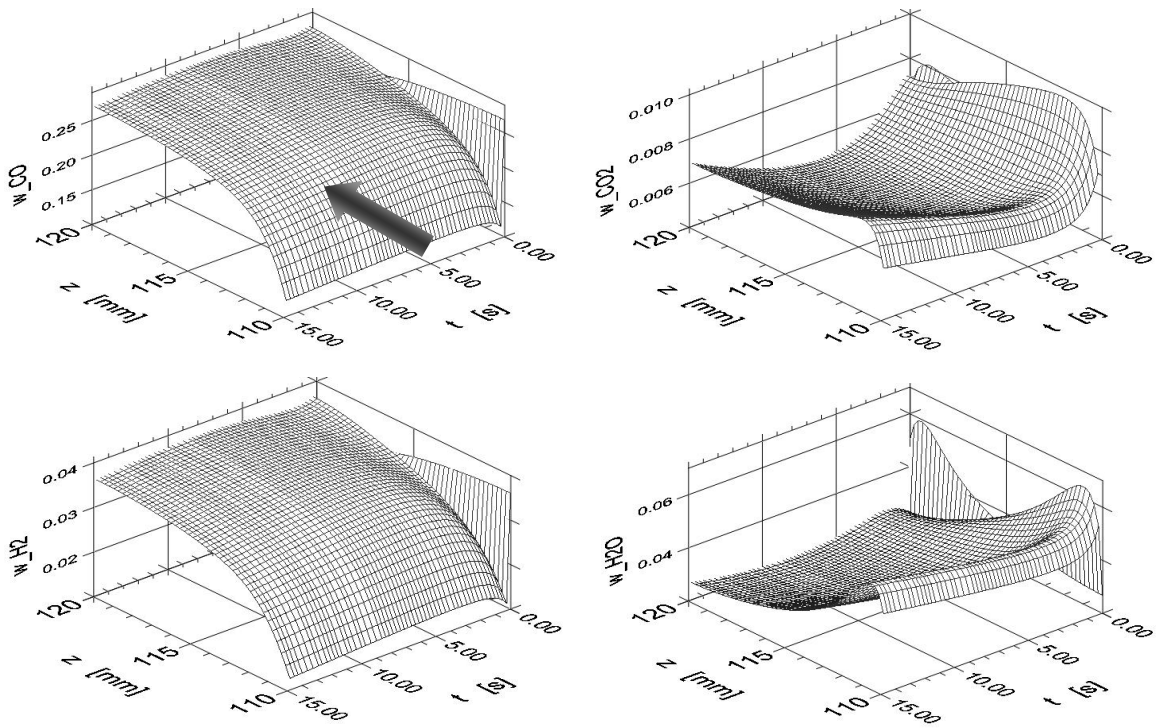


**Figure 54:** Partial (left) and total (right) oxidation product concentrations along the catalyst axis  $z$  during one semi-cycle (15 s); flow-direction indicated by arrow;  $CH_4/O_2 = 2.0$ ,  $\dot{V} = 4$  slm; improved reactor model

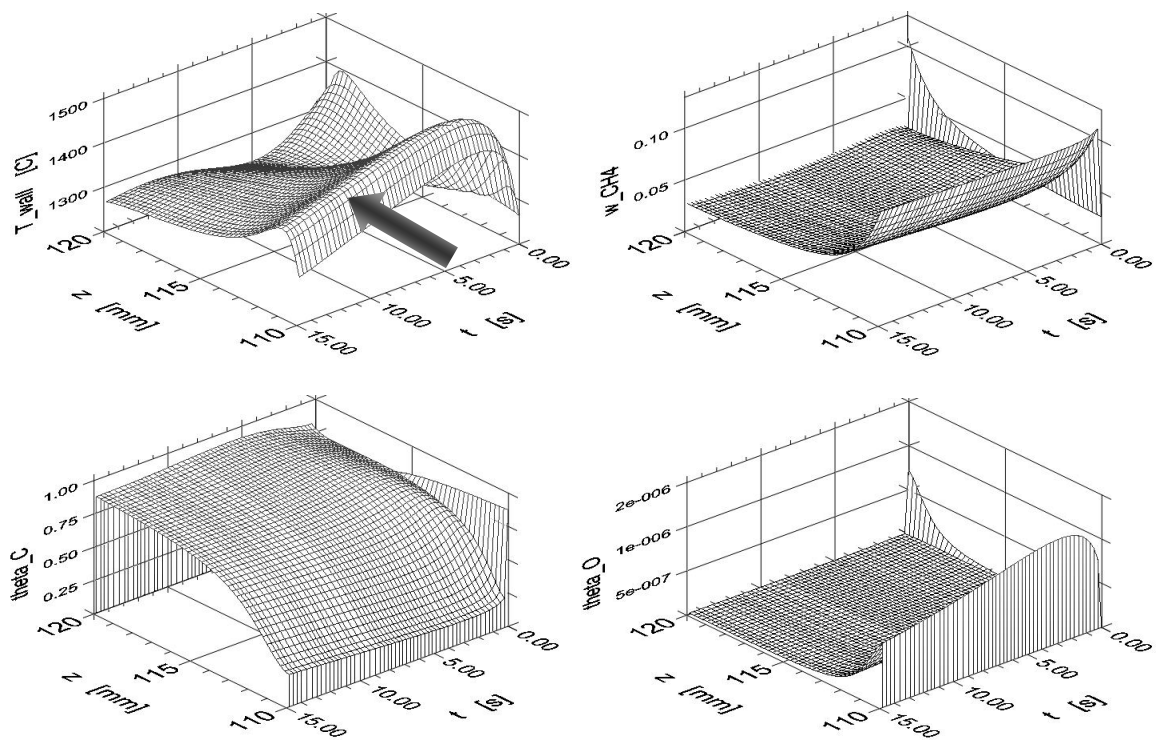
CO and H<sub>2</sub> concentration profiles on one hand and CO<sub>2</sub> and H<sub>2</sub>O concentration profiles on the other show very similar concentration curves. Syngas concentrations exhibit a strong increase during the first 4 mm of the catalyst bed, followed by a less pronounced increase during the last 6 mm of the catalyst bed. Along the time-axis, CO and H<sub>2</sub> concentrations show a convex behavior. Total oxidation product concentrations show an initial increase at the catalyst entrance (~1-2 mm into the catalyst bed) which is followed by a strong decrease in case of H<sub>2</sub>O and a weak decrease in case of CO<sub>2</sub> in the rest of the catalyst bed. Along the time-axis, H<sub>2</sub>O and CO<sub>2</sub> concentrations show a concave behavior with a minimum at the catalyst entrance around 3-4 s into the semi-cycle. Concentration curves thus generally suggest that a major part of the reaction takes place in the first 2-4 mm of the catalyst bed, where steep concentration profiles are observed. To fully understand the concentration curves of the products, it is necessary to investigate time-dependent temperature and surface coverage profiles.

Figure 55 shows corresponding catalyst temperatures, CH<sub>4</sub> concentrations and C- as well as O-surface coverages along the catalyst axis z during a semi-cycle. Temperature profiles show a complex behavior along the catalyst axis during the semi-cycle. Maximum temperatures along an axial slice are generally observed roughly 1-2 mm into the catalyst bed. During the initial stages of the semi-cycle, a second maximum is observed at the exit of the reaction zone which is pushed out of the catalyst bed within the first five seconds. Furthermore, the center portion of the catalyst bed is slowly heated up during the semi-cycle before it cools down slightly towards the end of the semi-cycle. Maximum catalyst entrance temperatures are observed 3 s into the semi-cycle.

Methane concentrations generally show a strong decrease during the first 2-3 mm into the catalyst bed and do not change noticeably during the semi-cycle, which supports the statement made above that a large part of the reaction occurs in this initial part of the catalyst bed.

Oxygen surface coverage shows a peak at the catalyst entrance followed by a drop to zero within the first 4 mm of the catalyst bed along the spatial axis. Along the time-axis, a maximum appears at the front edge of the catalyst about 3 s into the semi-cycle which correlates to maximum temperatures. Carbon coverage increases continuously from minimum values at the catalyst entrance to values around 0.9 at the catalyst exit. A minimum appears 3 s into the semi-cycle at the front edge of the catalyst.





**Figure 55:** Catalyst temperatures (upper left), CH<sub>4</sub> concentrations (upper right), C- (lower left) and O- (lower right) surface coverages along the catalyst axis  $z$  during one semi-cycle (15 s); flow-direction indicated by arrow; CH<sub>4</sub>/O<sub>2</sub> = 2.0,  $\dot{V}$  = 4 slm; improved model

Before a detailed investigation into the reaction mechanisms occurring during the semi-cycle is performed, a general observation will be discussed. The progressions of product concentrations and temperatures at the catalyst entrance, i.e. at  $z = 110$  mm, during the semi-cycle show optimum conditions for syngas yields about 3-4 s into the semi-cycle. Here, temperatures show a maximum and H<sub>2</sub>O and CO<sub>2</sub> concentrations a minimum and as could be expected from thermodynamics. However, at the same position, O-surface coverages exhibit a maximum and C-coverages a minimum. Clearly, the idea of a direct correlation between O-coverage and total oxidation on one hand and C-coverage and partial oxidation on the other (as proposed in chapter 2.2) cannot hold. The profiles thus suggest that syngas yields can only be influenced by optimized temperatures. A more detailed investigation of a potential increase in

syngas yields due to transient surface coverages immediately after flow-reversal is performed in Appendix H (page 126).

To better understand the complex interplay between temperature and concentration profiles, Figure 56 shows axial temperature and concentration slices along the catalyst axis at four different times (1, 5, 10 and 15 s) within the semi-cycle. Figure 57 shows corresponding oxygen concentration profiles (which however do not change at different times within a semi-cycle).

In the beginning of the semi-cycle, temperature profiles are characterized by two distinct peaks. One is positioned at the catalyst exit ( $z = 119$  mm) and corresponds to the reaction front of the preceding semi-cycle. This temperature peak is pushed out of the catalyst bed within the first couple of seconds into the semi-cycle. The second temperature peak corresponds to the newly developed reaction front at the catalyst entrance ( $z = 111$  mm). Here, the temperature initially increases due to regenerative heat-exchange in the RFR and decreases for  $t > 5$  s. The center portion of the catalyst bed ( $113 < z < 117$  mm) is slowly heated up by the front part of the catalyst bed and exhibits maximum temperatures around 10 s into the semi-cycle.

Methane concentrations are characterized by an initial strong decrease in the first 2-3 mm of the catalyst bed, followed by a less pronounced decrease thereafter. Syngas concentrations show a mirror-like behavior to methane concentrations: a strong increase at the catalyst front edge is followed by a weaker increase thereafter. Total oxidation product concentrations show a maximum at 1 mm into the catalyst bed followed by a pronounced decrease in case of  $H_2O$  and a less pronounced decrease in case of  $CO_2$  during the remaining part of the catalyst bed.  $O_2$  concentrations drop to zero within the first 3 mm of the reaction zone and do not change throughout the whole semi-cycle.

Concentration and temperature curves thus suggest that an initial oxidation (partial and total) of methane within the first 2-3 mm of the catalyst bed (where oxygen is still present) is followed by methane reforming reactions further downstream and results in the observed decrease in  $H_2O$  and  $CO_2$  concentrations. Higher temperature generally result in increased syngas yields, in the direct oxidation section as well as the reforming section, as can be observed from the slopes of the product concentration curves in Figure 56. However, the slopes of  $H_2O$  and  $CO_2$  concentrations in the reforming section suggests that steam reforming preferably takes place (at lower T) compared to  $CO_2$  reforming.

The concentration curves along the axis of the catalyst bed are influenced by dynamic temperature profiles along the entire catalyst bed during a semi-cycle (and not only at the catalyst entrance). Maximum temperatures at the catalyst front edge do not appear at the same time as maximum temperatures further downstream. Reforming reactions occurring in the final 2/3 of the catalyst bed therefore explain why optimum temperature profiles do not coincide with temperature profiles where maximum catalyst entrance temperatures are observed.

The fact that CO<sub>2</sub> reforming is not as pronounced as steam reforming explains why minimum CO<sub>2</sub> concentrations at the catalyst exit occur earlier within the semi-cycle than minimum H<sub>2</sub>O and maximum syngas concentrations (Figure 53): The influence of oxidation reactions (and hence catalyst entrance temperatures) on CO<sub>2</sub> concentrations is more pronounced than the influence of reforming reactions (temperatures further downstream).

Simulation results thus show that temperature profiles along the spatial axis of the catalyst bed, which cannot be measured experimentally, have a decisive influence on syngas yields. The catalyst bed can be divided into two parts: a direct oxidation zone during the first 2-3 mm of the reaction zone, which results in the formation of partial and total oxidation products, is followed by a reforming section, where predominantly steam reforming and to a certain extent also CO<sub>2</sub> reforming occurs. Increasing the temperature level enhances syngas yields, in the oxidation as well as the reforming section. Dynamic temperature profiles, which are mainly influenced by regenerative heat-exchange during the semi-cycle, explain time-dependent product gas concentration curves along the catalyst axis (Figure 54) and at the reactor exit (Figure 53).

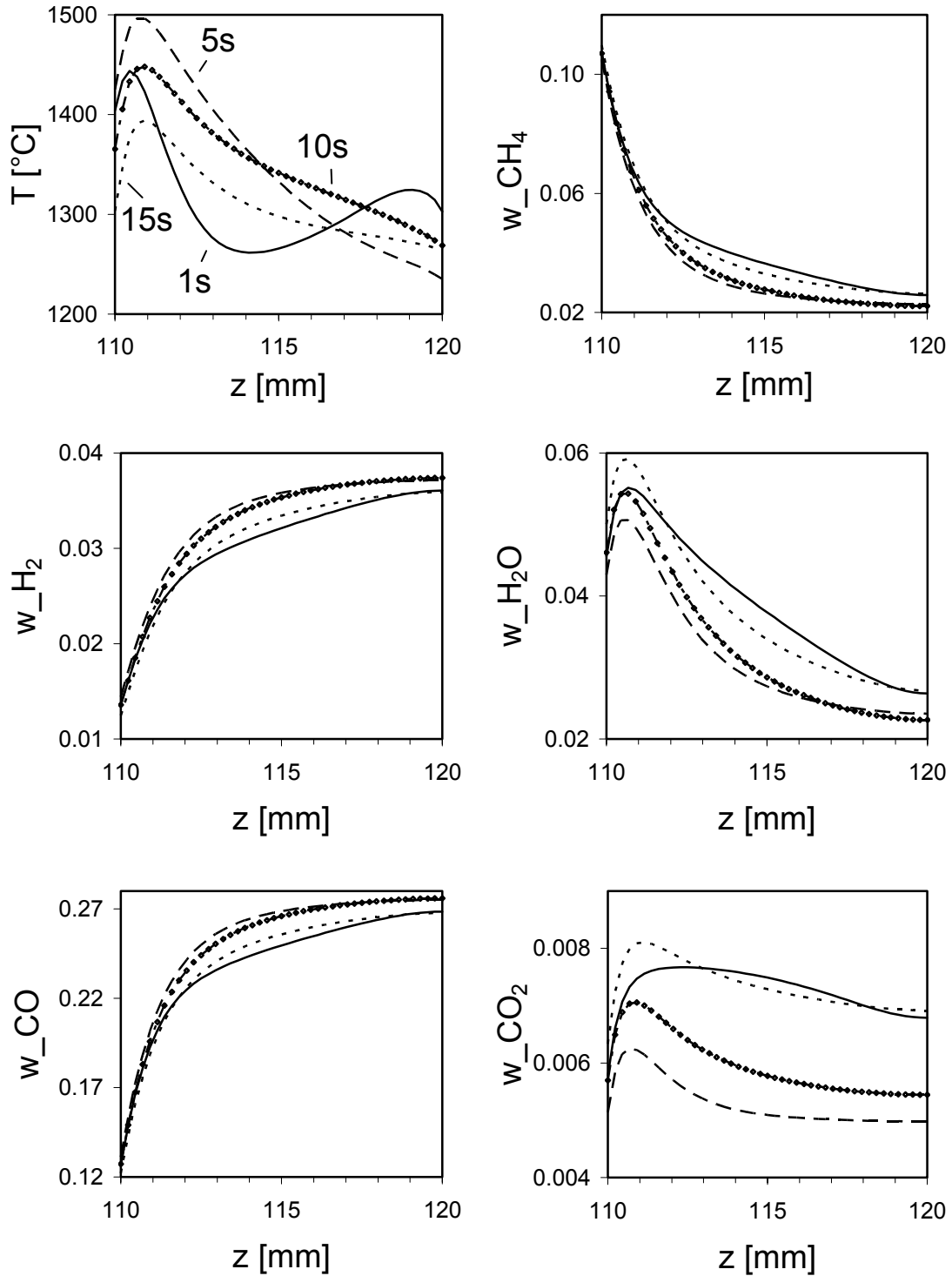


**Figure 56:** Catalyst temperatures as well as  $CH_4$ , partial and total oxidation product concentrations along the catalyst axis at 1 (solid line), 5 (dashed line), 10 (dots) and 15 s (dotted line) after flow-reversal; flow-direction from left to right;  $CH_4/O_2 = 2.0$ ,  $\tau/2 = 15$  s,  $\dot{V} = 4$  slm (calculated using improved reactor model)

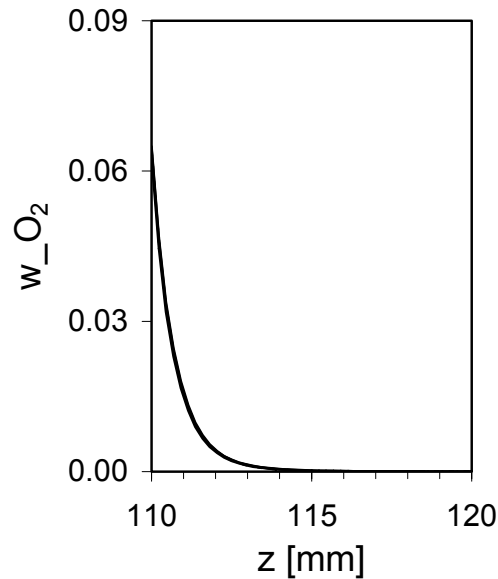


**Figure 57:**  $O_2$  concentrations along the catalyst axis during one semi-cycle;  $CH_4/O_2 = 2.0$ ,  $\tau/2 = 15$  s,  $\dot{V} = 4$  slm (calculated using improved reactor model)

#### 4.5 Summary and Discussion

Using a 1D reaction dispersion model and detailed elementary step reaction kinetics, CPOM in a plug-flow reactor was simulated. While syngas yields predicted by the ‘original’ model (as proposed by Vesper et al. [15]) showed an acceptable qualitative agreement to experiments at various  $CH_4/O_2$  ratios, temperature profiles, particularly catalyst entrance temperatures, were strongly overestimated.

Modifications were thus made to improve the reactor model. These included implementation of external mass transfer between gas and solid phase as well as optimization of monolith parameters (specific surface area). The changes made to the reactor model highlighted a general feature of reactor simulation: the quality of the complete model is strongly dependent on the error in the physical parameters describing the system. Unfortunately, high temperatures and complex catalyst support structure make an exact determination of these values extremely difficult or impossible.

Nevertheless, improvement of the reactor model as well as adjusted kinetic rate parameters resulted in lower catalyst entrance temperatures (compared to the original model) while enhancing the qualitative agreement to experimental data with varying CH<sub>4</sub>/O<sub>2</sub> ratios. Variation of the flow-rate however shows that the model validity is limited to a flow-rate of 4 slm and potentially catalyst entrance effects are not modeled accurately.

In dynamic reactor operation, global reaction yields agree qualitatively with experiments at different CH<sub>4</sub>/O<sub>2</sub> ratios, while temperatures are somewhat over-estimated. Additionally, time-dependent concentrations measured at the reactor exit show an excellent qualitative agreement with experiments and suggests that decisive reaction steps are modeled correctly. Furthermore, catalyst entrance temperatures show a maximum at comparable times within a semi-cycle and similar slopes thereafter, which shows that dynamic regenerative heat-exchange is also modeled correctly.

An analysis of the reaction mechanism revealed that endothermic steam and CO<sub>2</sub> reforming reactions occur in RFR operation. As a result, when product gases are flushed through the catalyst bed in the initial part of a semi-cycle, an increase in syngas yields is observed. However, this only occurs due to advantageous temperature profiles in the RFR immediately after flow-reversal and does not indicate that increasing the catalyst bed length should lead to improved syngas yields.

Investigation of the reaction mechanism during the major part of a semi-cycle revealed that the catalyst bed can generally be divided into two parts: an oxidation zone at the catalyst front edge (2-4 mm into the catalyst bed), followed by a section where steam and CO<sub>2</sub> reforming reactions occur (final 6-8 mm). The intensity of each reaction is dependent on the temperature level, which changes during the course of a semi-cycle.

Furthermore, simulation results show that a hypothesized 'kinetic' enhancement in syngas yields due to transient surface coverages after flow-reversal does not occur.

It can be said that improvements in syngas yields in the RFR are due to improved temperature profiles rather than surface coverage effects. We can therefore conclude that this principle is applicable also for high temperature catalytic partial oxidations of higher hydrocarbons, since temperature effects are generally less specific than surface coverage effects.

## 5.0 SUMMARY AND OUTLOOK

### 5.1 Summary

The presented work investigated the performance of CPOM in a dynamic RFR system. While autothermal CPOM is characterized by extreme temperatures, thermodynamics show that a complex interaction between partial and total oxidation reactions limits obtainable syngas yields at autothermal conditions. These limitations can be overcome by integrating sensible heat leaving the reaction zone in a multifunctional reactor concept. The particularly efficient regenerative heat-exchange in an RFR makes this reactor configuration particularly interesting for CPOM.

We built a computer controlled, laboratory-scale RFR to investigate general characteristics of CPOM in the dynamic reactor configuration. It was shown that RFR operation leads to particularly high catalyst entrance temperatures compared to steady-state conventional reactor operation. Increased catalyst entrance temperatures efficiently reduce total oxidation of methane and result in a pronounced increase in syngas yields.

Variation of flow-rate revealed that maximum attainable syngas yields are shifted towards even higher flow-rates and thus allow for even higher space-time yields in the RFR. Generally, increasing the flow-rate results in a strong increase in efficiency of the heat-integration since a larger part of the inert zone is used for heat-exchange. However, the temperature level increases strongly with higher flow-rates which eventually leads to onset of homogeneous reactions inside the inert zone and results in a destruction of the reactor (melting of inert zone). Furthermore, excessively high temperatures are potentially responsible for a fast catalyst deactivation and must thus be prevented under any circumstances.

However, long-term experiments revealed that dynamic reactor operation intrinsically counteracts catalyst deactivation and results in a less pronounced decrease in syngas yields compared to conventional reactor operation.

Increasing the selectivity of the catalyst or catalyst support (e.g. by reducing the pore size) is not only advantageous for syngas yields, but also leads to a strong reduction in mean and

maximum temperatures in the RFR. Experimental investigation using a novel nano-structured Pt catalyst showed that stable reactor operation at very high syngas yields could be obtained for at least 10 hours. Evidently, optimization of the complete process must include improvements in reactor configuration as well as optimization of the catalyst.

While the principles of dynamic reactor operation and high-temperature catalysis were clearly understood, the influence of dynamic temperatures inside the catalyst bed and surface reaction mechanisms could not be investigated experimentally. Thus, reactor simulations were performed to gain insights into the reaction mechanism.

Detailed numerical simulations showed that back-flushing of products through the catalyst bed during initial phase after flow-reversal results in a further increase in syngas yields which however only occurs due to advantageous temperature profiles (i.e. high temperatures at the catalyst exit) in dynamic reactor operation for a short period of time. Furthermore, the catalyst bed can generally be divided into two parts: an initial oxidation zone where partial and total oxidation of methane occurs, followed by a broad section where foremost endothermic reforming reactions occur. Steam reforming generally takes place more dominantly than CO<sub>2</sub> reforming. The relative amount of oxidation and reforming is dependent on the temperature level in each section. The temperature profile shows a complex development during a semi-cycle which is influenced by regenerative heat-exchange in dynamic reactor operation.

A kinetic improvement in syngas yields due to transient surface coverages in dynamic reactor operation as hypothesized in chapter 2.2.3 is not observed. Enhancements in syngas yield generally occur due to improved temperature profiles in the RFR.

Finally, high space-time yields and intense heat-exchange make this reactor concept particularly interesting for small scale, decentralized or mobile application for the production of syngas where compact, yet efficient reactors are needed.

## 5.2 Outlook

The study proved that total oxidation of methane can be reduced effectively by improved temperature profiles along the reactor axis. It can be expected that improvements in temperature profiles occur generally for partial oxidation reactions. The RFR principle and yield enhance-



ments should thus also be applicable to other high-temperature catalytic reactions, i.e. oxidative dehydrogenations e.g. of ethane to ethylene or propane to propylene. These reactions are characterized by similar partial and total oxidation interplays as CPOM. However, the reaction enthalpy for dehydrogenation reactions is lower than for partial oxidation of methane, so that some of the high temperature related problems in CPOM could potentially be bypassed in high-temperature oxidative dehydrogenation reactions in an RFR.

In CPOM, the  $H_2/CO$  ratio of the product gas can be influenced by adding steam or  $CO_2$  to the reactants. In this way, reforming reactions are enhanced and the  $H_2/CO$  ratio shifted to higher values if  $H_2O$  is added and lower values if  $CO_2$  is added. Particularly small-scale production of  $H_2$  e.g. for mobile applications (fuel cells in cars) is of current interest and could be realized in the RFR concept. Simultaneous reforming and oxidation reactions at the catalyst front edge should furthermore result in a better control of temperature level in dynamic reactor operation and could potentially allow for even higher flow-rates and space-time yields. A system to investigate the proposed configuration is currently being set up in our group.

## APPENDICES

## APPENDIX A

### Thermodynamic Calculations

The thermodynamic equilibrium product gas composition of a CH<sub>4</sub>/air mixture at different temperatures and a pressure of 1 atm is obtained by implementing the set of data into [42]. Selectivities and methane conversions are calculated using the mass fractions of the product gas composition given by [42].

The adiabatic temperature rise of a CH<sub>4</sub>/air mixture is calculated via an enthalpy balance. The total enthalpy of the feed gas is calculated by multiplying the mole fraction of the species (reactants) with the enthalpy of each species at the feed gas temperature (room temperature). The enthalpy of the product gas mixture is calculated with the mole fractions of the product gas mixture (as given by [42]) and the corresponding enthalpy at a (at first randomly) chosen temperature. In adiabatic case, the enthalpies of the two gas mixtures must be equal:

$$\sum_i n_i H_i(T_{feed}) = \sum_j n_j H_j(T)$$

By iterating between the product gas temperature and above equation, the temperature is estimated at which the above requirement is fulfilled.

Temperature and species dependent enthalpies are calculated using standard thermodynamic data [43].

## APPENDIX B

### Catalyst Preparation

The catalyst substrate consists of  $\alpha$ -Al<sub>2</sub>O<sub>3</sub> foam monoliths (Vesuvius High-Tech Ceramics) with a diameter of 1.7cm and a length of 1cm. The open space porosity is specified as ~80 %. The mean pore size of the monoliths is described by the ‘number of pores per linear inch’ (ppi). Where not stated otherwise, 45 ppi monoliths are used throughout the experiments.

The substrates are coated with Pt using standard impregnation procedures as listed in the following:

1. The surface of the monolith is cleaned of any residuals by holding it under a Bunsen-burner flame for several minutes.
2. The cold monolith is impregnated with a 25 %wt H<sub>2</sub>PtCl<sub>6</sub> (Sigma-Aldrich,) solution (using de-ionized water). Care has to be taken not to use too much solution since pores can get plugged and change the flow characteristics of the gases through the foam monolith.
3. The monolith is dried in an oven at 120°C for 10 hours.
4. The H<sub>2</sub>PtCl<sub>6</sub> is then reduced in an oven at 280°C in a 5 mol % H<sub>2</sub> in N<sub>2</sub> stream for 2-3 hours.

The impregnation and calcination procedure results in a thin metal coating on the foam structure and yields about 5-6 wt % Pt.

## APPENDIX C

### GC-Oven Setup

The GC system is used to measure the concentrations of the seven product gases CH<sub>4</sub>, O<sub>2</sub>, N<sub>2</sub>, H<sub>2</sub>, H<sub>2</sub>O, CO and CO<sub>2</sub>. The GC system consists of two separate ovens. The oven and detector parameters are listed in Table 2.

Oven 1 uses H<sub>2</sub> as a carrier gas and separates CH<sub>4</sub>, O<sub>2</sub>, N<sub>2</sub>, H<sub>2</sub>O, CO and CO<sub>2</sub> (H<sub>2</sub> concentrations cannot be determined since H<sub>2</sub> is the carrier gas). Two columns are used to perform the separation: one Haysep P (3m long and 1/8" in diameter) and one Molesieve 13X (3m long and 1/8" in diameter). Figure 58 shows a schematic of the column setup in oven 1. At the start of a GC run, the gases flow through the Haysep P column. Here, CH<sub>4</sub>, N<sub>2</sub>, O<sub>2</sub>, CO ('group 1') are separated from CO<sub>2</sub> and H<sub>2</sub>O. The approximate retention times of these components on the Haysep P column are listed in Table 3. CO<sub>2</sub> and H<sub>2</sub>O must not get on the molecular sieve. The group one components exit the Haysep P column first and are led onto the molecular sieve. Once this has been achieved, a valve is switched to 'bypass' mode. In this mode, the gases exiting the Haysep P column bypass the molecular sieve and are lead directly to the TCD (thermal conductivity detector) and FID (flame ionization detector). During this bypass period, the group 1 components are 'parked' on the molecular sieve. Following the group 1 components, CO<sub>2</sub> is the next component to exit the Haysep column and is therefore the first component to be detected in the chromatograph. Once all of the CO<sub>2</sub> has exited the Haysep column, the valve is again switched to molecular sieve. The molecular sieve now separates the group 1 components which are detected in the following order: O<sub>2</sub>, N<sub>2</sub>, CH<sub>4</sub>, CO. Once CO has exited the molecular sieve, the valve is again switched to bypass mode and water exits as the last component the Haysep column.

**Table 2:** GC oven and detector parameters

Parameter	Oven 1	Oven 2
INITT (initial oven T)	40°C	40°C
INJT (injection T)	250°C	200°C
DETT (detector T)	250°C	80°C
TCDT	100°C	80°C
D4CR (TCD current)	100	65
D4PL (TCD polarity)	1	2
Gas pressures [kPa]:		
Air (FID)	60	-
H <sub>2</sub> (FID)	80	-
carrier gas (column)	240 H <sub>2</sub>	190 Ar

Oven 2 separates H<sub>2</sub> from all other gases using 2 Haysep P columns (each 3m long and 1/8” diameter) switched in series with Ar as a carrier gas.

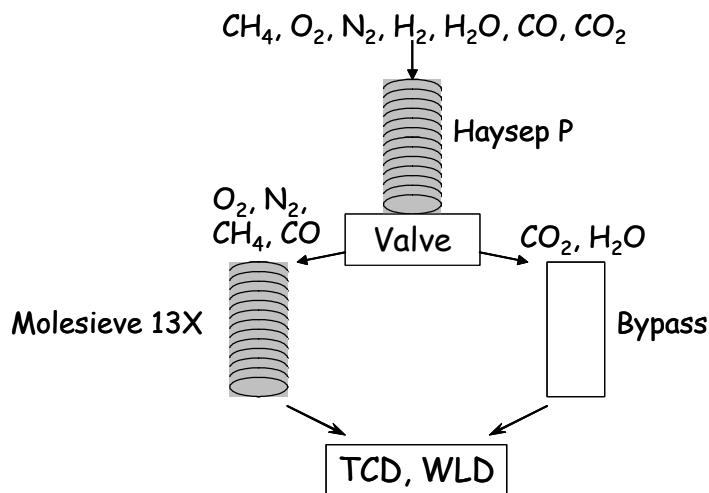


**Figure 58:** Schematic of the GC column setup in oven 1

**Table 3:** *Retention times of gas phase components on a Haysep P column*

component	approx. retention time [minutes]
O <sub>2</sub>	
N <sub>2</sub>	
CO	0.8-1.4
CH <sub>4</sub>	
CO <sub>2</sub>	2.25
H <sub>2</sub> O	9.3

## APPENDIX D

### Calculation of Selectivity and Conversion

Methane conversion ( $X_{CH_4}$ ) as well as selectivities towards  $H_2$  ( $S_{H_2}$ ) and  $CO$  ( $S_{CO}$ ) are calculated from the concentrations (mole fractions  $y_i$ ) detected with the GC at the outlet of the reactor. The mathematical procedure is laid out in the following.

The total flow of moles entering the system (labeled ‘in’) is a parameter set in the experiment and is (with  $\dot{N}_{CO}^{in} = \dot{N}_{H_2}^{in} = 0$ ):

$$\dot{N}^{in} = \dot{N}_{N_2}^{in} + \dot{N}_{CH_4}^{in} + \dot{N}_{O_2}^{in}$$

The total number of molar flows exiting the system is:

$$\dot{N} = \dot{N}_{N_2} + \dot{N}_{O_2} + \dot{N}_{CH_4} + \dot{N}_{CO} + \dot{N}_{H_2} + \dot{N}_{CO_2} + \dot{N}_{H_2O}$$

Methane conversion and partial oxidation selectivities are defined as:

$$X_{CH_4} = \frac{-\Delta\dot{N}_{CH_4}}{\dot{N}_{CH_4}^{in}} \quad S_{CO} = \frac{\Delta\dot{N}_{CO}}{-\Delta\dot{N}_{CH_4}} \quad S_{H_2} = \frac{\frac{1}{2}\Delta\dot{N}_{H_2}}{-\Delta\dot{N}_{CH_4}}$$

and with  $\Delta\dot{N}_j = \dot{N}_j - \dot{N}_j^{in}$ :



$$X_{CH_4} = \frac{\dot{N}_{CH_4}^{in} - \dot{N}_{CH_4}}{\dot{N}_{CH_4}^{in}} \quad S_{CO} = \frac{\dot{N}_{CO}}{\dot{N}_{CH_4}^{in} - \dot{N}_{CH_4}} \quad S_{H_2} = \frac{\frac{1}{2} \dot{N}_{H_2}}{\dot{N}_{CH_4}^{in} - \dot{N}_{CH_4}}$$

The inlet molar flows (set with the mass flow controllers) as well as the molar fractions  $y_i$  of the product gases (measured with the GC) are known.

The total number of moles can now be calculated by substituting

$$\dot{N}_j = y_j \cdot \dot{N}, \quad \dot{N}_{N_2} = \dot{N}_{N_2}^{in}$$

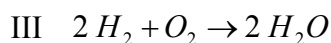
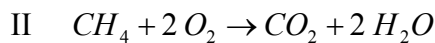
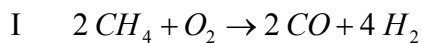
into above equation which yields

$$\dot{N} = \frac{\dot{N}_{N_2}^{in}}{(1 - y_{CH_4} - y_{CO} - y_{CO_2} - y_{H_2} - y_{H_2O} - y_{O_2})}$$

This is sufficient to calculate syngas yields with above mentioned equations.

The error related to the detection of some components is larger than for others (e.g. water as well as components with extremely low molar fractions are very difficult to detect accurately), so that it is desirable to reduce the amount of variables necessary for calculating selectivities and conversions to a minimum. This can be done by using key components. Since there are 6 reactive components but only 3 atomic species present in the gas mixture, 3 molar fractions are sufficient to solve above equations. One example will be shown of how to calculate the X, S using one set of key components.

In a first step it is necessary to choose 3 chemical equations which must be independent of each other. The equations chosen in this example shall be:



Or written in a matrix form:

equation	CH <sub>4</sub>	CO	CO <sub>2</sub>	H <sub>2</sub>	O <sub>2</sub>	H <sub>2</sub> O
I	-2	2	0	4	-1	0
II	-1	0	1	0	-2	2
III	0	0	0	-2	-1	2

Using the conversion of the reaction  $\xi_i$ , the molar conversion of each component can be written as the sum of all conversions of all reactions.

With

$$\Delta \dot{N}_j = \dot{N}_j - \dot{N}_j^{in} \quad \text{and} \quad \Delta \dot{N}_j = \sum_{i=1}^I \nu_{i,j} \xi_i \quad \text{and} \quad \dot{N}_{Products}^{in} = 0$$

( $\nu_i$  is the stoichiometric factor) results:

$$\begin{aligned} \dot{N}_{CH_4} - \dot{N}_{CH_4}^{in} &= -2\xi_1 - \xi_2 \\ \dot{N}_{O_2} - \dot{N}_{O_2}^{in} &= -2\xi_1 - 2\xi_2 - \xi_3 \\ \dot{N}_{H_2} &= 4\xi_1 - 2\xi_3 \\ \dot{N}_{CO} &= 2\xi_1 \\ \dot{N}_{H_2O} &= 2\xi_2 + 2\xi_3 \\ \dot{N}_{CO_2} &= \xi_2 \end{aligned}$$

At this point key components have to be chosen. One has to make sure that all atomic species (in this case O, H, C) appear in either of these components. In this example CH<sub>4</sub>, CO<sub>2</sub> and O<sub>2</sub> shall be the key components. One now has to solve above equations to  $\xi_{1-3}$  in such a way, that only the molar product flows of the key components (and any [known] flow of reactants) appear on the right side of the equation.

$$\xi_1 = -\frac{1}{2} \dot{N}_{CH_4} + \frac{1}{2} \dot{N}_{CH_4}^{in} - \frac{1}{2} \dot{N}_{CO_2}$$

$$\xi_2 = \dot{N}_{CO_2}$$

$$\xi_3 = -\dot{N}_{O_2} + \dot{N}_{O_2}^{in} + \frac{1}{2}\dot{N}_{CH_4} - \frac{1}{2}\dot{N}_{CH_4}^{in} - \frac{3}{2}\dot{N}_{CO_2}$$

Now the molar flows for the components which are not key components (in this case H<sub>2</sub>, H<sub>2</sub>O, CO) can be calculated by replacing  $\xi_{1-3}$  in above equation:

$$\dot{N}_{CH_4} = y_{CH_4} \cdot \dot{N}$$

$$\dot{N}_{O_2} = y_{O_2} \cdot \dot{N}$$

$$\dot{N}_{CO_2} = y_{CO_2} \cdot \dot{N}$$

$$\dot{N}_{H_2} = 3\dot{N}_{CH_4}^{in} - 2\dot{N}_{O_2}^{in} + (y_{CO_2} - 3y_{CH_4} + 2y_{O_2}) \cdot \dot{N}$$

$$\dot{N}_{CO} = \dot{N}_{CH_4}^{in} - (y_{CO_2} + y_{CH_4}) \cdot \dot{N}$$

$$\dot{N}_{H_2O} = 2\dot{N}_{O_2}^{in} - \dot{N}_{CH_4}^{in} + (y_{CH_4} - 2y_{O_2} - y_{CO_2}) \cdot \dot{N}$$

$$\dot{N}_{N_2} = \dot{N}_{N_2}^{in}$$

The molar flows are now added up to calculate the total flow of moles:

$$\dot{N} = \dot{N}_{N_2} + \dot{N}_{O_2} + \dot{N}_{CH_4} + \dot{N}_{CO} + \dot{N}_{H_2} + \dot{N}_{CO_2} + \dot{N}_{H_2O}$$

which results in

$$\dot{N} = \frac{3\dot{N}_{CH_4}^{in} + \dot{N}_{N_2}^{in}}{(1 + 2y_{CH_4} - y_{O_2})}$$

and hence:

$$X_{CH_4} = \frac{\dot{N}_{CH_4}^{in} - y_{CH_4} \cdot \dot{N}}{\dot{N}_{CH_4}^{in}}$$

$$S_{CO} = \frac{N_{CH_4}^{in} - (y_{CO_2} + y_{CH_4}) \cdot \dot{N}}{\dot{N}_{CH_4}^{in} - y_{CH_4} \cdot \dot{N}}$$

$$S_{H_2} = \frac{\frac{3}{2} \dot{N}_{CH_4}^{in} - \dot{N}_{O_2}^{in} + \frac{1}{2} (y_{CO_2} - 3y_{CH_4} + 2y_{O_2}) \cdot \dot{N}}{\dot{N}_{CH_4}^{in} - y_{CH_4} \cdot \dot{N}}$$

These steps can be followed through with different sets of key components as well as different equations (e.g. water-gas shift, steam-reforming). In the experimental part, a total number of 6 pairs of key components as well as 5 equations were used to determine selectivities and conversions. Absolute values between different sets of key components varied only up to 1.5%, so that mean values were calculated and displayed throughout this thesis. These mean values were usually in very good agreement (+/- 0.5%) with selectivities and conversions calculated using the direct method (i.e. not using key components). Furthermore, atom balances closed in a typical run to better than 1%.

## APPENDIX E

### Reactor Startup

The ignition temperature of an air/methane mixture over a Pt-catalyst is dependent on the  $\text{CH}_4/\text{O}_2$  ratio and decreases with fuel richer mixtures. It lies at about  $400^\circ\text{C}$  for a  $\text{CH}_4/\text{O}_2$  ratio of 2.0 [50]. To avoid the time consuming procedure of heating the catalyst above ignition temperature using heating tape wrapped around the steel-housing, the catalyst is heated by feeding a 3 mol % hydrogen in air mixture through the reactor. Since  $\text{H}_2/\text{air}$  mixtures above 5 % are in the explosion regime, care has to be taken to first flush the reactor with air before adding hydrogen. The mixture reacts in an exothermic reaction to water over Pt catalysts at room temperature. The efficient heat-integration in dynamic reactor mode quickly leads to catalyst temperatures exceeding  $400^\circ\text{C}$ . Once this temperature has been reached, the feed gas is switched to  $\text{CH}_4$  and air. To avoid potentially explosive  $\text{CH}_4/\text{air}$  mixtures ( $\text{CH}_4/\text{air}$  mixtures containing less than 20 %  $\text{CH}_4$  are explosive), the reactor has to be flushed with methane first before air is added to the reactant stream. Once the reaction ignites, periodic steady-state is usually reached within 30 to 45 minutes of reactor operation.

## APPENDIX F

### Original Reactor Model and Reaction Mechanism

#### Reactor Model

The model presented in the following was developed in previous studies by Veser et al. [15]. The reactor is modeled by a heterogeneous one-dimensional reaction-dispersion model. Gas and solid phase are described separately by sets of partial differential equations. The gas phase is characterized by the gas temperature as well as mass fractions of the components CH<sub>4</sub>, O<sub>2</sub>, N<sub>2</sub>, CO, CO<sub>2</sub>, H<sub>2</sub> and H<sub>2</sub>O. The solid phase is characterized by the wall temperature and surface coverages of all reactants as well as intermediate species and products on the catalyst. The equations are based on energy and mass balances and are listed in Table 4 (for explanation of abbreviations see Table 5). Detailed derivations of these equations can be found e.g. in [51].

Mass balances for gas phase species consist of mass transport by convection and dispersion, adsorption/desorption of the species to/from the catalyst surface as well as local change in concentration of component  $j$  due to adsorption and desorption of all species  $i$  (last term on the right side). The gas phase energy-balance is composed of convective heat-transport, heat-conduction in the gas phase as well as heat-transfer between gas and solid phase. The energy balance of the catalyst is comprised of monolith heat-conductivity, heat-transfer between solid and gas phase, heat-losses to the environment as well as reaction enthalpies of the reactions occurring on the catalyst surface. Mass balances of surface coverages consist of diffusion of the species on the catalyst surface and net balances due to surface reactions, which will be outlined in more detail in the following chapter. The pressure drop along the axis of the monolith is negligible and is set to zero.

**Table 4:** Energy and mass balance equations of the reactor model

---

Energy balance solid phase:

$$(1-\varepsilon) \cdot \rho_s \cdot c_{p,s} \cdot \frac{\partial T_s}{\partial t} = (1-\varepsilon) \cdot \lambda_s \cdot \frac{\partial^2 T_s}{\partial z^2} - a_V \cdot \alpha \cdot (T_s - T_g) - k_{ext} \cdot a_{ext} \cdot (T_s - T_{ext}) - a_V \cdot \sum_k r_k \cdot \Delta H_{r,k}$$

---

Energy balance gas phase:

$$\varepsilon \cdot \rho_g \cdot c_{p,g} \cdot \frac{\partial T_g}{\partial t} = -\frac{\dot{m}}{A} \cdot c_{p,g} \cdot \frac{\partial T_g}{\partial z} + \varepsilon \cdot \frac{\partial}{\partial z} \left( \lambda_g \cdot \frac{\partial T_g}{\partial z} \right) + a_V \cdot \alpha \cdot (T_s - T_g)$$

---

Mass balance gas phase:

$$\varepsilon \cdot \rho_g \cdot \frac{\partial \omega_j}{\partial t} = -\frac{\dot{m}}{A} \cdot \frac{\partial \omega_j}{\partial z} + \varepsilon \cdot D_{eff} \cdot \frac{\partial^2 \omega_j}{\partial z^2} + a_V \cdot M_j \cdot (r_{des,j} - r_{ads,j}) - a_V \cdot \omega_j \sum_i M_i \cdot (r_{des,i} - r_{ads,i})$$

---

Mass balance surface species:

$$a_V \cdot \theta_i \cdot M_i \cdot \frac{\partial \theta_i}{\partial t} = D_{OF} \cdot \frac{\partial^2 \theta_i}{\partial z^2} + a_V \cdot M_i \cdot (r_{ads,i} - r_{des,i}) + a_V \cdot M_i \cdot \sum_k r_k$$

---

Three simplifying assumptions are made in the model: a) Gas phase reactions are neglected since it has been shown that the ignition delay for homogeneous reactions is much longer than the residence times of the reactants in the reactor; b) Mass transport limitations at the solid-gas boundary layer are disregarded since the system is adsorption-desorption limited (Veser et al. [15] discussed and validated the simplifying assumptions a) and b) in detail); c) Furthermore, heat radiation effects are neglected since the foam structure of the monolithic catalyst strongly reduces radiative heat-transport along the reactor axis.

Reactor dimensions are taken from the experiment and are listed together with physical properties of the solid and the gas phase in Table 5.

**Table 5:** *Reactor dimensions and physical properties used in the model*

parameter	catalyst support		inert zones	
	symbol	value	symbol	value
monolith diameter	$d_m$	1.7 cm	$d_m$	1.7 cm
monolith length	$l_{cat}$	1.0 cm	$l_{IZ}$	11.0 cm
monolith porosity	$\varepsilon$	0.8	$\varepsilon$	0.8
specific surface area	$a_{v,cat}$	$5 \cdot 10^5 \text{ m}^2/\text{m}^3$	$a_{v,IZ}$	$2.6 \cdot 10^3 \text{ m}^2/\text{m}^3$
monolith density	$\rho_{cat}$	$3800 \text{ kg}/\text{m}^3$	$\rho_{IZ}$	$2100 \text{ kg}/\text{m}^3$
monolith heat-capacity	$c_{p,cat}$	$900 \text{ J}/\text{kg}\cdot\text{K}$	$c_{p,IZ}$	$700 \text{ J}/\text{kg}\cdot\text{K}$
heat-transfer coefficient	$\alpha_{cat}$	$100 \text{ W}/\text{m}^2\cdot\text{K}$	$\alpha_{IZ}$	$20 \text{ W}/\text{m}^2\cdot\text{K}$
thermal conductivity	$\lambda_{cat} [\text{W}/\text{m}\cdot\text{K}]$	$1.3 @ 25^\circ\text{C}$ $15 @ 1000^\circ\text{C}$	$\lambda_{IZ}$	$2.0 \text{ W}/\text{m}\cdot\text{K}$
dispersion coefficient	$D_{eff}$	$5 \cdot 10^{-4} \text{ m}^2/\text{s}$		
heat-loss coefficient	$k_{ext}$	$15 \text{ W}/\text{m}^2\cdot\text{K}$		

The monoliths' properties are taken from the manufacturers' data sheets where possible. The thermal conductivity of the foam monolith was set to 1.3 W/m/K at temperatures above 1000°C (experimental investigation by Sweeting et al. [52]) and 15 W/m/K at room temperature and linearly interpolated in between. The heat-loss coefficient was estimated by comparing temperature profiles along the reactor axis of the simulation with those of steady-state experiments (see Figure 19).

### Reaction Mechanism

The above described reactor model is coupled with detailed elementary step reaction kinetics, which considers catalytic reactions and intermediate products of total and partial oxidation of methane on the Pt surface. Kinetic equations and rate parameters, which were developed in previous studies [15], are listed in Table 6 ( $E_{Act}$  activation energy in kJ/mol,  $k_0$  rate constant at standard conditions,  $s_j$  sticking coefficient of species  $j$ ,  $\Delta H_r$  reaction enthalpy in kJ/mol).



Methane decomposition is implemented as a single, irreversible reaction step since no experimental data are available for the intermediate species CH<sub>3</sub>, CH<sub>2</sub> and CH. Even though the decomposition step includes four free surface sites, it is described as a first order reaction since mechanistically it is a series of four individual H subtraction steps.

**Table 6:** Surface reaction steps and rate parameters

Reaction	ID	E <sub>Act</sub> [kJ/mol]	k <sub>0</sub> [1/s]	S <sub>j</sub>	ΔH <sub>r</sub> [kJ/mol]
CH <sub>4</sub> ↔ CH <sub>4</sub> <sup>*</sup>	ads/des,CH <sub>4</sub>	18	10 <sup>13</sup>	10 <sup>-4</sup>	-18.0
O <sub>2</sub> ↔ 2O <sup>*</sup>	ads/des,O <sub>2</sub>	215-θ <sub>O</sub> ·60	10 <sup>13</sup>	0.003	-215.0
CO ↔ CO <sup>*</sup>	ads/des,CO	142	10 <sup>15</sup>	0.84	-142.0
CO <sub>2</sub> ↔ CO <sub>2</sub> <sup>*</sup>	ads/des,CO <sub>2</sub>	21.5	10 <sup>13</sup>	0.005	-21.5
H <sub>2</sub> ↔ 2H <sup>*</sup>	ads/des,H <sub>2</sub>	74	10 <sup>13</sup>	0.05	-74.0
H <sub>2</sub> O ↔ H <sub>2</sub> O <sup>*</sup>	ads/des,H <sub>2</sub> O	43.5	10 <sup>13</sup>	0.1	-43.5
CH <sub>4</sub> <sup>*</sup> → C <sup>*</sup> + 4H <sup>*</sup>	deco,CH <sub>4</sub>	60	5·10 <sup>13</sup>		-89.5
C <sup>*</sup> + O <sup>*</sup> → CO <sup>*</sup>	form,CO	60	5·10 <sup>12</sup>		-120.0
CO <sup>*</sup> → C <sup>*</sup> + O <sup>*</sup>	deco,CO	180	5·10 <sup>13</sup>		120.0
CO <sup>*</sup> + O <sup>*</sup> → CO <sub>2</sub> <sup>*</sup>	form,CO <sub>2</sub>	100-θ <sub>O</sub> ·50	5·10 <sup>14</sup>		-55.0
CO <sub>2</sub> <sup>*</sup> → CO <sup>*</sup> + O <sup>*</sup>	deco,CO <sub>2</sub>	155-θ <sub>O</sub> ·50	5·10 <sup>15</sup>		55.0
O <sup>*</sup> + H <sup>*</sup> → OH <sup>*</sup>	form,OH	10	5·10 <sup>13</sup>		-8.0
OH <sup>*</sup> → O <sup>*</sup> + H <sup>*</sup>	deco,OH	18	5·10 <sup>12</sup>		8.0
OH <sup>*</sup> + H <sup>*</sup> → H <sub>2</sub> O <sup>*</sup>	form,H <sub>2</sub> O	16	5·10 <sup>13</sup>		-94.0
H <sub>2</sub> O <sup>*</sup> → OH <sup>*</sup> + H <sup>*</sup>	deco,H <sub>2</sub> O	110	10 <sup>13</sup>		94.0
2 OH <sup>*</sup> → H <sub>2</sub> O <sup>*</sup> + O <sup>*</sup>	reac,OH	50	10 <sup>13</sup>		-86.0
H <sub>2</sub> O <sup>*</sup> + O <sup>*</sup> → 2 OH <sup>*</sup>	reac,H <sub>2</sub> O	136	10 <sup>13</sup>		86.0

Kinetic equations for each surface species yield:

$$\frac{\partial \theta_{CH_4}}{\partial t} = k_{ads,CH_4} \cdot p_{CH_4} \cdot \theta_{free} - k_{des,CH_4} \cdot \theta_{CH_4} - k_{deco,CH_4} \cdot \theta_{CH_4} \cdot \theta_{free}$$

$$\begin{aligned}\frac{\partial \theta_O}{\partial t} = & 2 \cdot k_{ads,O_2} \cdot p_{O_2} \cdot \theta_{free}^2 - 2 \cdot k_{des,O_2} \cdot \theta^2_O + k_{deco,OH} \cdot \theta_{OH} \cdot \theta_{free} - k_{form,OH} \cdot \theta_O \cdot \theta_H \\ & + k_{deco,CO} \cdot \theta_{CO} \cdot \theta_{free} - k_{form,CO} \cdot \theta_O \cdot \theta_C + k_{deco,CO_2} \cdot \theta_{CO_2} \cdot \theta_{free} - k_{form,CO_2} \cdot \theta_{CO} \cdot \theta_O \\ & + k_{reac,OH} \cdot \theta_{OH}^2 - k_{reac,H_2O} \cdot \theta_{H_2O} \cdot \theta_O\end{aligned}$$

$$\begin{aligned}\frac{\partial \theta_{CO}}{\partial t} = & k_{ads,CO} \cdot p_{CO} \cdot \theta_{free} - k_{des,CO} \cdot \theta_{CO} + k_{form,CO} \cdot \theta_C \cdot \theta_O - k_{deco,CO} \cdot \theta_{CO} \cdot \theta_{free} \\ & + k_{deco,CO_2} \cdot \theta_{CO_2} \cdot \theta_{free} - k_{form,CO_2} \cdot \theta_{CO} \cdot \theta_O\end{aligned}$$

$$\frac{\partial \theta_{CO_2}}{\partial t} = k_{ads,CO_2} \cdot p_{CO_2} \cdot \theta_{free} - k_{des,CO_2} \cdot \theta_{CO_2} + k_{form,CO_2} \cdot \theta_{CO} \cdot \theta_O - k_{deco,CO_2} \cdot \theta_{CO_2} \cdot \theta_{free}$$

$$\begin{aligned}\frac{\partial \theta_H}{\partial t} = & 2 \cdot k_{ads,H_2} \cdot p_{H_2} \cdot \theta_{free}^2 - 2 \cdot k_{des,H_2} \cdot \theta^2_H + 4 \cdot k_{deco,CH_4} \cdot \theta_{CH_4} \cdot \theta_{free} + k_{deco,OH} \cdot \theta_{OH} \cdot \theta_{free} \\ & - k_{form,OH} \cdot \theta_O \cdot \theta_H + k_{deco,H_2O} \cdot \theta_{H_2O} \cdot \theta_{free} - k_{form,H_2O} \cdot \theta_{OH} \cdot \theta_H\end{aligned}$$

$$\begin{aligned}\frac{\partial \theta_{H_2O}}{\partial t} = & k_{ads,H_2O} \cdot p_{H_2O} \cdot \theta_{free} - k_{des,H_2O} \cdot \theta_{H_2O} + k_{form,H_2O} \cdot \theta_{OH} \cdot \theta_H - k_{deco,H_2O} \cdot \theta_{H_2O} \cdot \theta_{free} \\ & + k_{reac,OH} \cdot \theta_{OH}^2 - k_{reac,H_2O} \cdot \theta_{H_2O} \cdot \theta_O\end{aligned}$$

$$\begin{aligned}\frac{\partial \theta_{OH}}{\partial t} = & k_{form,OH} \cdot \theta_O \cdot \theta_H - k_{deco,OH} \cdot \theta_{OH} \cdot \theta_{free} + k_{deco,H_2O} \cdot \theta_{H_2O} \cdot \theta_{free} - k_{form,H_2O} \cdot \theta_{OH} \cdot \theta_H \\ & + k_{reac,H_2O} \cdot \theta_{H_2O} \cdot \theta_O - k_{reac,OH} \cdot \theta_{OH}^2\end{aligned}$$

$$\frac{\partial \theta_C}{\partial t} = k_{deco,CH_4} \cdot \theta_{CH_4} \cdot \theta_{free} + k_{deco,CO} \cdot \theta_{CO} \cdot \theta_{free} - k_{form,CO} \cdot \theta_C \cdot \theta_O$$

Reaction rates for all reaction steps except for the adsorption of the gas phase species are calculated with the Arrhenius law:

$$k = k_0 \cdot e^{-E_{act}/RT}$$

The adsorption steps are non-activated and are calculated using the kinetic gas theory:

$$k_{ads,j} = \frac{S_j}{\sqrt{2\pi \cdot M_j \cdot RT_g}}$$

## Numerics

Above described balance equations are one-dimensional parabolic partial differential equations (PDEs) and can be written in the general form

$$\bar{B} \cdot \frac{\partial \bar{y}}{\partial t} = -\bar{C} \cdot \frac{\partial \bar{y}}{\partial z} + \frac{\partial}{\partial z} \left( \bar{D} \cdot \frac{\partial \bar{y}}{\partial z} \right) + \bar{Q}.$$

Using Danckwerts type boundary conditions [53] and appropriate initial conditions, the system is solved numerically. The algorithm used for solving the set of PDEs is PdexPACK [54] which was developed by Nowak [55]. It is adaptive in time and space and automatically optimizes the accuracy of the calculation by adjusting the number and distribution of the grid points as well as the time-steps according to the discretization error. In this way, an equal distribution of the error along the spatial axis is assured.

## APPENDIX G

### Improved Reactor Model

It is the objective of the model improvement to better fit catalyst entrance temperatures of the simulation to experimental data by improving reactor parameters, but at the same time keep yields and catalyst exit temperatures constant. Due to highly temperature dependent reaction selectivities in CPOM, however, it can be expected that a change in temperature profile will most probably also have a strong effect on overall yields.

In addition to reactor parameters, kinetic rate parameters have to be adjusted. Lowering catalyst entrance temperatures by enhancing the reactor model will, using unchanged kinetics, result in decreased syngas yields. The only way to combine lowering temperatures while keeping yields constant is by simultaneously adjusting rate parameters. This adjustment is complex, since 23 individual reaction steps describe the system and extend the range of variable parameters considerably.

The influence of mass transfer and specific catalyst surface area upon temperature profiles and yields is investigated and the kinetics of the system adjusted.

#### Mass Transfer

Heterogeneously catalyzed chemical reactions consist of several process steps which include the diffusion of gases through a boundary layer (i.e. external mass transfer), pore diffusion, adsorption/desorption of the reactants/products onto the catalyst surface as well as the actual chemical reaction. All of these processes together are called the macro-kinetics of the system. The effective reaction rate is potentially influenced by all of these individual, temperature dependent steps.

When a gas flows across a surface, a laminar boundary layer is formed. Heat and mass transfer through this boundary is limited and strongly dependent on the thickness of the boundary layer and therefore the flow characteristics. Mass transfer is usually characterized by the Sherwood (Sh) number, which is a function of the Reynolds (Re) and the Schmidt (Sc) number.

In the original model described above, mass transfer through the boundary layer at the gas-solid interface was neglected, since it was proposed that the system is adsorption/desorption limited [15] (in which case mass transfer is not rate limiting and may be omitted). Nonetheless, in these previous studies the influence of mass transfer on catalyst entrance temperatures was not investigated and is therefore performed in the following.

To investigate the influence of mass transfer on temperatures and yields in CPOM, the model is extended to include external mass transfer between the gas phase and the catalyst surface. For this purpose, additional equations representing concentrations of the gas phase species immediately above the catalyst surface (i.e. the molecular layer that interacts with the catalyst surface) are included in the model. Mass balance equations for those boundary layer (bl) gas phase species consist of the dispersion term, adsorption/desorption of the species onto the catalyst surface, mass transfer between the bulk gas phase and the boundary layer as well as changes in concentration of the species due to adsorption/desorption and mass transfer of all species:

$$\begin{aligned} \varepsilon_{bl} \cdot \rho_{g,bl} \cdot \frac{\partial \omega_{j,bl}}{\partial t} = & \varepsilon_{bl} \cdot D_{eff,bl} \cdot \frac{\partial^2 \omega_{j,bl}}{\partial z^2} + a_v \cdot M_j \cdot (r_{des,j} - r_{ads,j}) - a_v \cdot \omega_{j,bl} \sum_i M_i \cdot (r_{des,i} - r_{ads,i}) \\ & + \beta \cdot a_v \cdot \frac{M_j}{RT} \cdot (p_j - p_{j,bl}) - a_v \cdot \omega_{j,bl} \sum_i \beta \cdot \frac{M_i}{RT} \cdot (p_i - p_{i,bl}) \end{aligned}$$

with  $\rho_{g,bl}$  density of the gas phase in the boundary layer,  $w_{j,bl}$  mass fraction of species j in the boundary layer,  $D_{eff,bl}$  boundary-layer dispersion coefficient,  $p_j$ ,  $p_{j,bl}$  partial pressures of component j in the bulk gas phase and the boundary layer, respectively,  $\beta$  mass transfer coefficient. For numerical reasons, a value greater than zero has to be assigned to  $\varepsilon_{bl}$  which is set to 0.01. The dispersion coefficient of the boundary layer is assumed to be the one of the bulk gas phase.

Mass balances for the bulk gas phase species are changed accordingly and yield:

$$\varepsilon \cdot \rho_g \cdot \frac{\partial \omega_j}{\partial t} = -\frac{\dot{m}}{A} \cdot \frac{\partial \omega_j}{\partial z} + \varepsilon \cdot D_{eff} \cdot \frac{\partial^2 \omega_j}{\partial z^2} - \beta \cdot a_v \cdot \frac{M_j}{RT} \cdot (p_j - p_{j,bl}) + a_v \cdot \omega_j \sum_i \beta \cdot \frac{M_i}{RT} \cdot (p_i - p_{i,bl})$$

Using the model including mass transfer, partial oxidation selectivities, CH<sub>4</sub> conversions as well as catalyst entrance (solid and gas phase) and exit (solid identical to gas phase) temperatures with varying mass transfer coefficient  $\beta$  were calculated and are shown in Figure 59 (CH<sub>4</sub>/O<sub>2</sub> ratio of 2.0 and a flow-rate of 4 slm).

Syngas yields remain constant for  $\beta$  values larger than 0.05 m/s with a sharp decrease towards smaller  $\beta$ . While catalyst exit temperatures are not influenced over a broad range of  $\beta$  and decrease with  $\beta$  smaller than 0.05 m/s, catalyst entrance temperatures decrease continuously with decreasing  $\beta$  values.

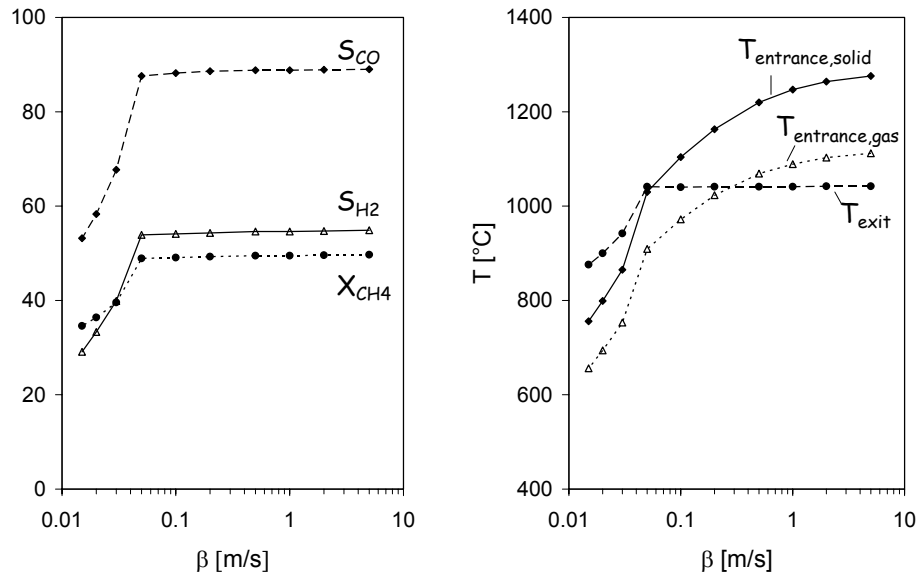


**Figure 59:** Syngas selectivities and methane conversions (left) as well as catalyst temperatures (right) as a function of mass transfer coefficient  $\beta$ ; CH<sub>4</sub>/O<sub>2</sub> = 2.0,  $\dot{V} = 4$  slm

Clearly, mass transfer has a strong influence on catalyst entrance temperatures over the whole range investigated and for  $\beta$  smaller than 0.05 m/s also on syngas yields and catalyst exit temperatures. It is interesting to notice that yields change abruptly for  $\beta$  smaller than 0.05 m/s and do not vary continuously as might be expected. This effect occurs due to a constraint of the reactor model: thermal conductivity of the solid has a constant value at temperatures exceeding 1000°C and is temperature dependent between 25 and 1000°C. Syngas yields and temperature profiles are generally strongly dependent on thermal conductivity of the solid. Figure 60 shows syngas yields and catalyst temperatures as a function of the upper limit (i.e.  $T > 1000^\circ\text{C}$ ) of the thermal conductivity of the solid at a  $\text{CH}_4/\text{O}_2$  ratio of 2.0 and a flow-rate of 4 slm. Increasing the thermal conductivity coefficient strongly reduces yields and temperatures. In case of varying mass transfer coefficient (Figure 59), this means that as soon as the temperature (here: at the catalyst entrance) drops below 1000°C (which occurs for  $\beta$  values smaller than 0.05

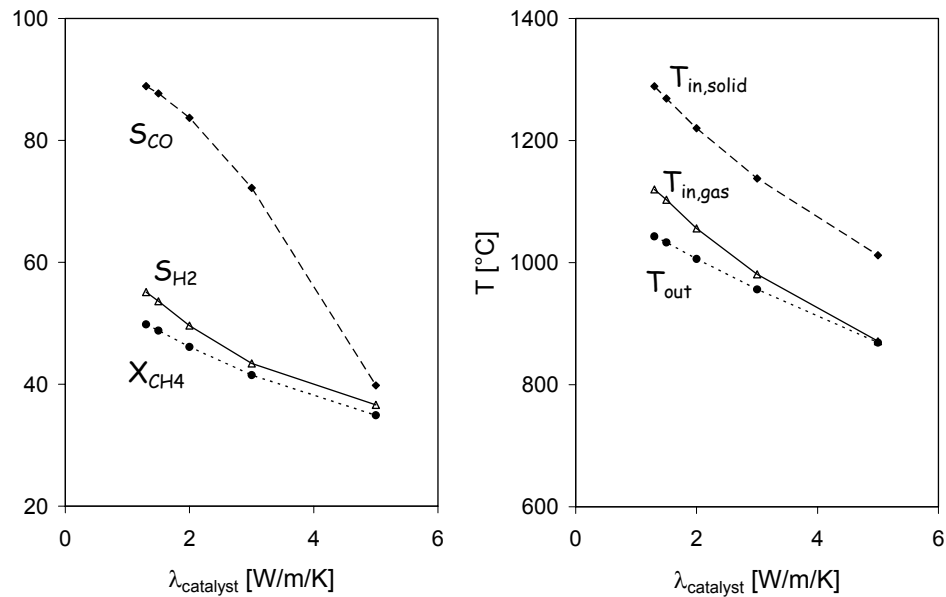


**Figure 60:** Partial oxidation selectivities and methane conversions (left) as well as catalyst temperatures (right) as a function of catalyst thermal conductivity;  $\text{CH}_4/\text{O}_2 = 2.0$ ,  $\dot{V} = 4$  slm

m/s), the conductivity changes abruptly and results in the observed decrease in partial oxidation selectivities and methane conversion.

These results highlight the strong influence of macroscopic parameters (mass transfer, thermal conductivity) on temperature profiles and yields. The accuracy of the whole model is directly linked to the error related to these parameters. Unfortunately, the random structure of the foam monolith as well as extreme temperatures makes an exact determination of these parameters very difficult.

To estimate a value for  $\beta$  for the monolithic catalyst used in the experiments, an appropriate Sherwood number correlation has to be used. Derivations for the tortuous foam structure of the monolith used cannot be found in the literature. Therefore, correlations for extruded monoliths are used which approximately describe the system.

Several studies investigating mass transfer on honeycomb monoliths which are commonly used in the automotive industry have been performed. Vortuba et al. [56] investigated the vaporization of water and hydrocarbons from an extruded monolith and fitted the experimental data to the following correlation:

$$Sh = 0.705 \cdot \left( \frac{d}{L} \cdot Re \right)^{0.43} \cdot Sc^{0.56}$$

Ullah et al. [57] investigated mass transfer in a monolithic reactor under reacting conditions and developed the correlation:

$$Sh = 0.766 \cdot \left( \frac{d}{L} \cdot Re \cdot Sc \right)^{0.483}$$

with

$$Sh = \frac{\beta \cdot d}{D}, \quad Re = \frac{d \cdot v \cdot \rho}{\mu}, \quad Sc = \frac{\mu}{D \cdot \rho},$$

(pore diameter  $d$ , monolith length  $L$ , mass transfer coefficient  $\beta$ , diffusion coefficient  $D$ , linear gas velocity  $v$ , density  $\rho$ , viscosity  $\mu$ ).

Since physical properties of a gas mixture are strongly dependent on gas composition as well as temperature, a gas mixture of air and methane over the temperature range observed in the experiment is assumed for an estimation of  $\beta$ . Table 7 lists properties used for calculating the dimensionless numbers.



Implementing the physical properties into above equations gives comparable results for both correlations (Vortuba and Ullah). The range of mass transfer coefficients varies from minimum values of 0.04 m/s at low temperatures and large pore diameters to above 0.15 m/s at high temperatures and small diameters.

Since generally catalyst entrance temperatures drop with increasing mass transfer resistance and very low temperatures are observed in the experiments, a mass transfer coefficient  $\beta$  of 0.05 m/s will be used in the following, keeping in mind that it can only reflect an estimate of the actually very complex mass transport process across the boundary layer.

**Table 7:** *Physical properties of a methane-air gas mixture*

<b>parameter</b>	<b>value range (300°C &lt; T &lt; 1100°C)</b>
diffusion coefficient D [m <sup>2</sup> /s]	6*10 <sup>-5</sup> - >2*10 <sup>-4</sup>
viscosity $\mu$ [kg/m/s]	3*10 <sup>-5</sup> - 6*10 <sup>-5</sup>
density $\rho$ [kg/m <sup>3</sup> ]	0.5-0.1
pore diameter d [m]	0.008-0.012

#### Variation of Monolith Specific Surface Area

As mentioned above, reactor parameters and physical properties (e.g. monolith thermal conductivity) have a strong influence on yields and temperature profiles. Since the determination of many of these parameters is afflicted with a certain error, it is difficult to adjust model parameters to actual experimental values.

A monolith parameter which is afflicted with a particularly large error is the specific surface area  $a_v$ . Surface areas for foam monoliths are reported between 0.1-1 m<sup>2</sup>/g [6, 16], with similar catalyst supports weighing between 1.2 – 2.0 g. Due to the resulting large range of possible specific surface areas (5.3\*10<sup>4</sup> - 8.8\*10<sup>5</sup> m<sup>2</sup>/m<sup>3</sup>), it is thus important to investigate the influence of specific surface area onto reaction yields and temperatures.

Figure 61 shows syngas selectivities and methane conversions (left) as well as catalyst temperatures (right) as a function of the specific surface area  $a_v$  at a  $\text{CH}_4/\text{O}_2$  ratio of 2.0, a flow-rate of 4slm and  $\beta$  0.05 m/s. Methane conversions and partial oxidation selectivities drop only slightly between  $4.0$  and  $5.0 \cdot 10^5 \text{ m}^2/\text{m}^3$  and show a strong decrease with specific surface areas smaller than  $4.0 \cdot 10^5 \text{ m}^2/\text{m}^3$ . Catalyst entrance temperatures (solid and gas phase) drop continuously by 200-300°C over the investigated range of  $a_v$ . Reducing the specific surface area from  $5.0 \cdot 10^5$  to  $4.0 \cdot 10^5 \text{ m}^2/\text{m}^3$  results in a slight increase in catalyst exit temperatures which is followed by a drop for surface areas smaller than  $4.0 \cdot 10^5 \text{ m}^2/\text{m}^3$ .

The influence of specific surface area of the catalyst support onto reaction yields and temperatures is very complex. In the equations describing the system (Table 4),  $a_v$  appears in heat and mass transfer, adsorption/desorption as well as reaction terms.

Reducing the surface area generally results in a reduction of the number of available surface sites. Therefore, the relative amount of oxygen on the surface increases which results in a

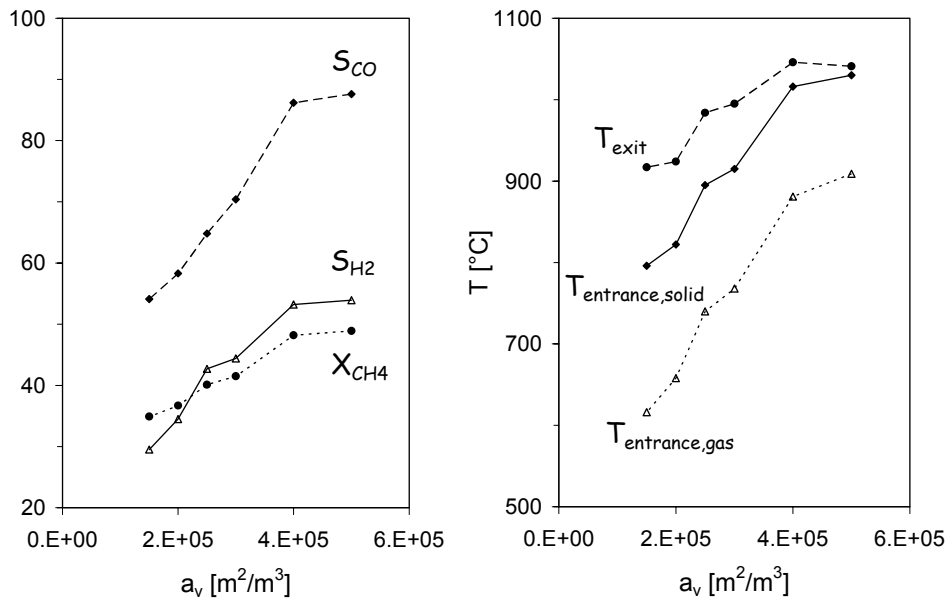


**Figure 61:** Syngas selectivities and methane conversions (left), catalyst temperatures (right) as a function of  $a_v$ ;  $\text{CH}_4/\text{O}_2 = 2.0$ ,  $\dot{V} = 4 \text{ slm}$ ,  $\beta = 0.05 \text{ m/s}$

preferential total oxidation and explains the observed decrease in syngas selectivities and (for  $4 \cdot 10^5 < a_v < 5 \cdot 10^5 \text{ m}^2/\text{m}^3$ ) increasing catalyst exit temperatures. For surface areas smaller than  $4.0 \cdot 10^5 \text{ m}^2/\text{m}^3$ , however, catalyst entrance temperatures of the solid drop below  $1000^\circ\text{C}$  which results in the above described change in thermal conductivity, leading to a pronounced drop in yields and temperatures.

Figure 61 again emphasizes the fact that catalyst entrance temperatures can obviously not be lowered with a single reactor parameter without influencing the whole system, i.e. temperatures and yields.

Choosing an appropriate value for  $a_v$  is difficult. On one hand, catalyst entrance temperatures need to be lowered for a better agreement with experimental data. On the other hand, low specific surface areas result in a decrease of catalyst exit temperatures and syngas yields far below values measured in the experiment. While syngas yields can be adjusted (i.e. improved) within a certain range by optimizing reaction rate parameters, more ‘syngas selective’ kinetics will result in a further decrease of the catalyst exit temperature (due to lower reaction-enthalpies of partial compared to total oxidation reactions). Hence, a compromise (regarding a value for  $a_v$ ) between improved catalyst entrance temperatures and worsened catalyst exit temperatures and yields has to be found. In the following, a value of  $2.0 \cdot 10^5 \text{ m}^2/\text{m}^3$  will thus be used in the model.

The changes made to reactor parameters generally resulted in strongly decreased syngas yields. Hence, reaction rate parameters need to be optimized to increase syngas yields and better fit model predictions to experimentally measured data.

### Adjusting Reaction Rate Parameters

The changes made to the reactor model not only result in a decrease of catalyst entrance temperatures, but also in a loss of syngas selectivities. It is thus necessary to enhance syngas yields to values observed in experiments by adjusting kinetic rate parameters.

The determination of a pre-exponential factor of a specific surface reaction step is very difficult and hence afflicted with a relatively large error. A first-order reaction rate constant of  $10^{13} \text{ s}^{-1}$  can be derived as a first guess from transition state theory for reactions where the transition state complex is not too different from the adsorbed state [15]. However, simplifications and assumptions made in these calculations are reflected in the accuracy of pre-

exponential factors. Pre-exponential factors are hence afflicted with an error which can be as large as an order of magnitude. It is therefore legitimate to adjust the initial pre-exponential factors within this range to better fit model predictions to experimental data.

To correct reaction yields to values observed in the experiments, kinetic parameters were adjusted in the following way: Vesper et al. [15] performed a sensitivity analysis of the system with respect to changes in kinetic rate parameters. Using these results as a guideline, rate parameters were adjusted one by one (at a constant  $\text{CH}_4/\text{O}_2$  ratio of 2.0 and a flow-rate of 4 slm) and the influence on methane conversion and syngas selectivities observed. The system was assumed to be ‘optimized’ once syngas yields matched experimental data for the specific set of reactor parameters. These ‘optimized’ reaction rate parameters for a  $\text{CH}_4/\text{O}_2$  ratio of 2.0 and a flow-rate of 4slm are listed in Table 8.

It must be emphasized that the set of values given in Table 8 is only one of many possible solutions to the described optimization procedure. The behavior of the system towards variation of the  $\text{CH}_4/\text{O}_2$  ratio or the flow-rate depends on the set of values. However, the number of possible sets of optimized parameters (which fit yields at the  $\text{CH}_4/\text{O}_2$  ratio and flow-rate chosen for the optimization procedure) is large due to the large number of surface reaction steps. Therefore, only the one set of parameters given in Table 8 is investigated.

**Table 8:** *Adjusted reaction rate parameters*

Reaction	optimized $k_0$ [1/s]	optimized $s_j$
$\text{CH}_4 \leftrightarrow \text{CH}_4^*$	$2.0 \cdot 10^{14}$	$1.2 \cdot 10^{-4}$
$\text{O}_2 \leftrightarrow 2\text{O}^*$	$10^{13}$	0.003
$\text{CO} \leftrightarrow \text{CO}^*$	$1.2 \cdot 10^{15}$	0.80
$\text{CO}_2 \leftrightarrow \text{CO}_2^*$	$10^{13}$	0.005
$\text{H}_2 \leftrightarrow 2\text{H}^*$	$10^{13}$	0.05
$\text{H}_2\text{O} \leftrightarrow \text{H}_2\text{O}^*$	$9.0 \cdot 10^{12}$	0.1
$\text{CH}_4^* \rightarrow \text{C}^* + 4\text{H}^*$	$2 \cdot 10^{14}$	
$\text{C}^* + \text{O}^* \rightarrow \text{CO}^*$	$1 \cdot 10^{13}$	
$\text{CO}^* \rightarrow \text{C}^* + \text{O}^*$	$5 \cdot 10^{13}$	
$\text{CO}^* + \text{O}^* \rightarrow \text{CO}_2^*$	$5 \cdot 10^{14}$	
$\text{CO}_2^* \rightarrow \text{CO}^* + \text{O}^*$	$5 \cdot 10^{15}$	
$\text{O}^* + \text{H}^* \rightarrow \text{OH}^*$	$5 \cdot 10^{13}$	
$\text{OH}^* \rightarrow \text{O}^* + \text{H}^*$	$6.0 \cdot 10^{12}$	
$\text{OH}^* + \text{H}^* \rightarrow \text{H}_2\text{O}^*$	$3 \cdot 10^{13}$	
$\text{H}_2\text{O}^* \rightarrow \text{OH}^* + \text{H}^*$	$10^{13}$	
$2 \text{OH}^* \rightarrow \text{H}_2\text{O}^* + \text{O}^*$	$10^{13}$	
$\text{H}_2\text{O}^* + \text{O}^* \rightarrow 2 \text{OH}^*$	$10^{13}$	

## APPENDIX H

### Influence of Surface Coverage Inversion on Syngas Yields

As laid out in chapter 2.2.3, periodic flow-reversal not only leads to efficient regenerative heat-exchange but also results in an inversion of catalyst surface coverages.

Numerical investigations by Vesper et al. [15] suggest a close correlation between O-surface coverage and total oxidation on one hand as well as C-coverage and partial oxidation on the other. It was thus hypothesized in this work (chapter 2.2.3) that transient surface coverages in dynamic reactor operation, i.e. where C-coverage is dominant and O-coverage suppressed, could potentially lead to increased syngas yields due to a kinetic effect.

In the following, a close investigation of the first 0.1 s after flow-reversal, i.e. when transient surface coverages can be observed, is performed.

Figure 62 shows O<sub>2</sub> and CH<sub>4</sub> concentrations as well as C- and O-surface coverages along the catalyst axis between  $0.04 < t < 0.14$  s after flow-reversal. As laid out in chapter 4.4.1, back flushing of product gases occurs so that initial 0.04 s are omitted.

Dispersion effects result in a continuous increase of reactant concentrations at the catalyst entrance between  $0.05 < t < 0.14$  s (rather than a sudden jump). At  $t = 0.04$  s, the catalyst is almost completely covered with carbon, while no oxygen is present on the surface. At 0.05 s, C-coverage drops at the catalyst entrance while O-coverage increases continuously. Hence, as soon as gas phase oxygen reaches the catalyst front edge, oxygen is adsorbed onto the catalyst surface due to a higher sticking coefficient of oxygen compared to methane on the Pt surface.

Figure 63 shows corresponding partial (left) and total (right) oxidation product concentrations. At 0.04 s into the semi-cycle, CO and H<sub>2</sub> concentrations increase slightly along the catalyst bed while CO<sub>2</sub> and H<sub>2</sub>O decrease due to endothermic methane reforming reactions

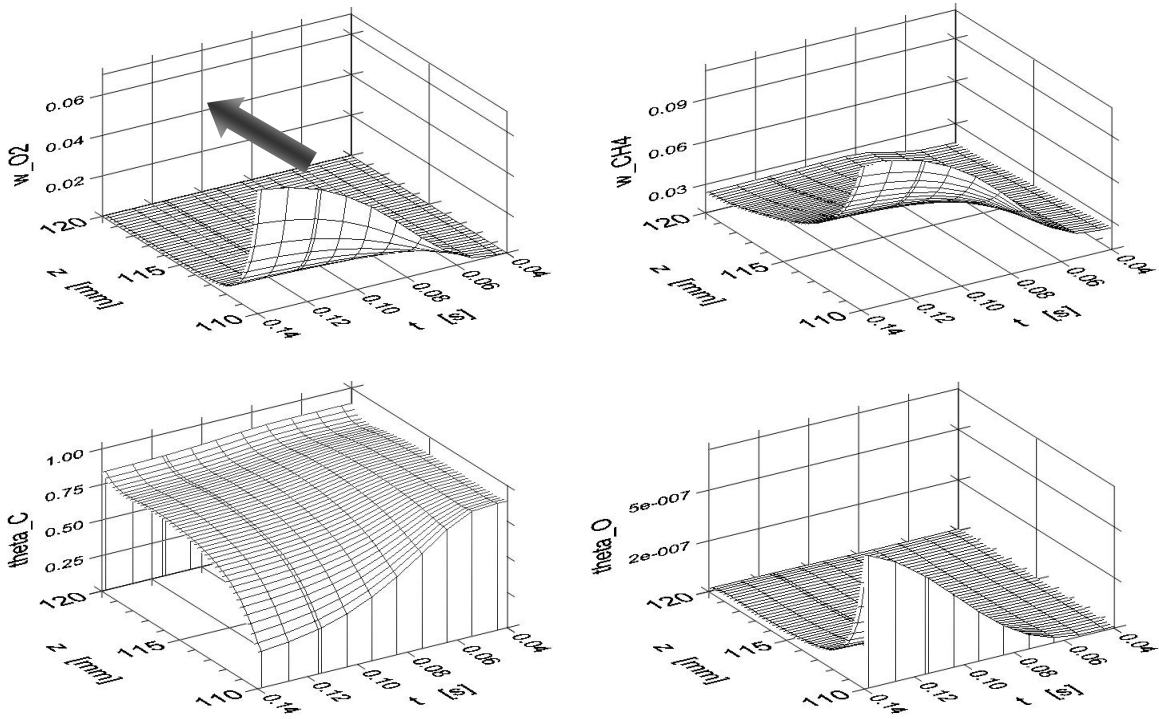


**Figure 62:**  $O_2$ - (upper left) and  $CH_4$ - (upper right) concentrations as well as  $C$ - (lower left) and  $O$ - (lower right) surface coverages along the catalyst axis  $z$  between 0.04 and 0.14 s after flow-reversal;  $CH_4/O_2 = 2.0$ ,  $\tau/2 = 15$  s,  $\dot{V} = 4$  slm (calculated using improved reactor model)

taking place (chapter 4.4.1). At 0.05 s, reactants reach the catalyst front edge (see Figure 62). At this time, CO and  $H_2$  concentrations start decreasing at the catalyst front edge while  $H_2O$  concentrations start increasing.  $CO_2$  concentrations drop between  $0.04 < t < 0.08$  s at the catalyst entrance before they increase continuously at  $t > 0.08$  s.

During the short period investigated, temperatures remain essentially constant along the catalyst bed (Figure 64) and assure isothermal behavior. Generally, dispersion effects make an interpretation of the observed concentration profiles difficult. Syngas concentrations run parallel to carbon coverages and drop at the catalyst entrance as soon as reactants enter the catalyst bed. In parallel, O-coverage builds up at the catalyst entrance ( $t > 0.06$  s) and runs parallel to  $H_2O$

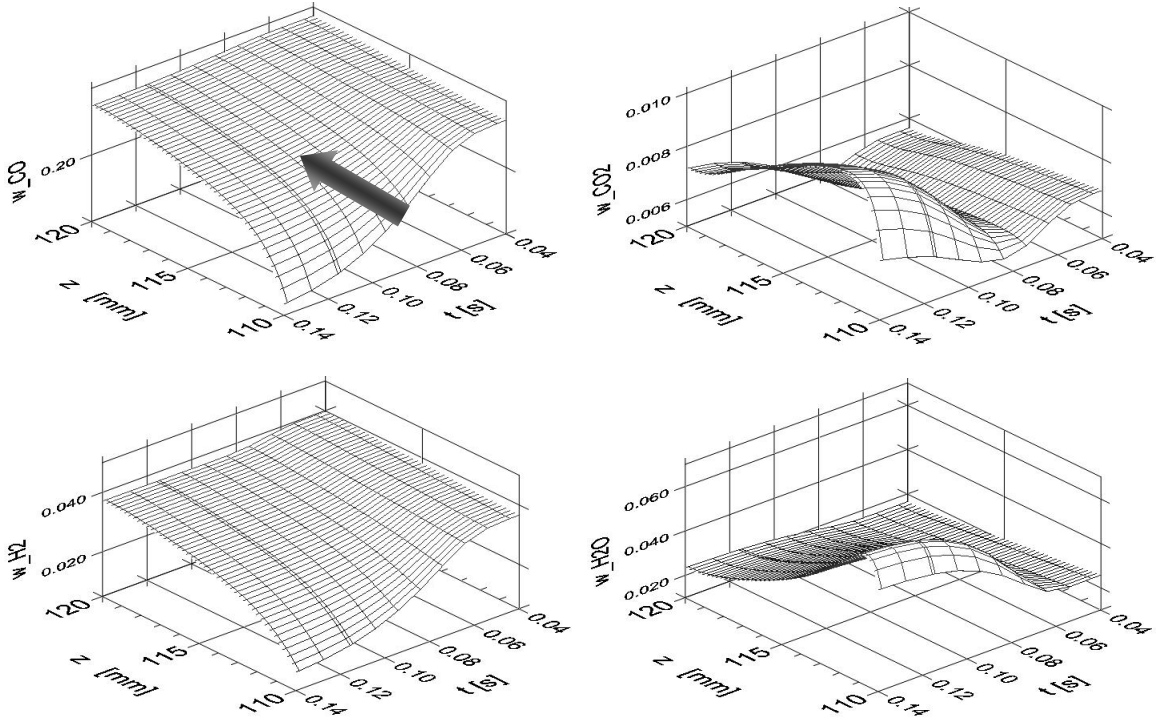


**Figure 63:** Partial (left) and total (right) oxidation product concentrations along the catalyst axis  $z$  between 0.04 and 0.14 s after flow-reversal;  $\text{CH}_4/\text{O}_2 = 2.0$ ,  $\tau/2 = 15$  s,  $\dot{V} = 4$  slm (calculated using improved reactor model)

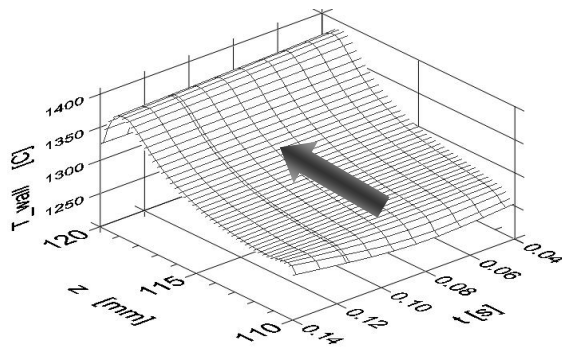


**Figure 64:** Catalyst temperatures along the catalyst axis  $z$  between 0.04 and 0.14 s after flow-reversal,  $\text{CH}_4/\text{O}_2 = 2.0$ ,  $\tau/2 = 15$  s,  $\dot{V} = 4$  slm (calculated using improved reactor model)



concentrations. CO<sub>2</sub> concentrations however show a slightly different behavior. Between 0.05 < t < 0.08 s, CO<sub>2</sub> concentrations drop at the catalyst entrance and only increase for t > 0.08 s. This suggests that H<sub>2</sub>O is (kinetically) preferentially formed compared to CO<sub>2</sub>. Nevertheless, the graphs do not show any kind of peak in partial oxidation product concentrations at the catalyst front edge but rather a continuous decrease. This clearly shows that syngas yield enhancements due to transient surface coverages are not possible.

These results are confirmed by observations made in chapter 4.4.2, where it was shown that minimum total oxidation product concentrations at the catalyst entrance (Figure 54) coincide with maximum temperatures as well as maximum oxygen and minimum carbon surface-coverages (Figure 55). This also indicates that the idea of a direct correlation between O-coverage and total oxidation as well as C-coverage and partial oxidation cannot hold. Generally it seems as though yields can only be enhanced by improving temperature profiles in CPOM.

## BIBLIOGRAPHY

## BIBLIOGRAPHY

- [1] Hickman, D.A. and L.D. Schmidt, *Production of Syngas by Direct Catalytic Oxidation of Methane*, Science, 1993. **259**: p. 343.
- [2] Boreskov, G. and Y. Matros, *Unsteady-State Performance of Heterogeneous Catalytic Reactions*, Catal. Rev.-Sci. Eng., 1983. **25**: p. 551.
- [3] Wender, I., *Reactions of synthesis gas*, Fuel Processing Technology, 1996. **48**(3): p. 189.
- [4] Lunsfort, J.H., *Catalytic conversion of methane to more useful chemicals and fuels: a challenge for the 21st century*, Catalysis Today, 2000. **63**: p. 165.
- [5] Rostrup-Nielsen, J.R., *Syngas in perspective*, Catalysis Today, 2002. **71**(3-4): p. 243.
- [6] Bodke, A.S., S.S. Bharadwaj and L.D. Schmidt, *The Effect of Ceramic Supports on Partial Oxidation of Hydrocarbons over Noble Metal Coated Monoliths*, Journal of Catalysis, 1998. **179**(1): p. 138.
- [7] Bsile, F., et al., *Partial oxidation of methane; Effect of reaction parameters and catalyst composition on the thermal profile and heat distribution*, Catalysis Today, 2001. **64**: p. 21.
- [8] Friedle, U., J. Schicks and G. Vesper, *Synthesis Gas by Direct Oxidation of Methane in a catalytic heat-exchange reactor*, Proceedings of the DGMK-Conference, 2000: p. 53.
- [9] Froment, G.F. and A.M. De Groote, *Simulation of the catalytic partial oxidation of methane to synthesis gas*, Applied Catalysis A: General, 1996. **138**(2): p. 245.
- [10] Hohn, K.L. and L.D. Schmidt, *Partial oxidation of methane to syngas at high space velocities over Rh-coated spheres*, Applied Catalysis A: General, 2001. **211**(1): p. 53.
- [11] Hickman, D.A. and L.D. Schmidt, *Steps in CH<sub>4</sub> Oxidation on Pt and Rh Surfaces: High-Temperature Reactor Simulations*, AIChE Journal, 1993. **39**: p. 1164.

- [12] Schmidt, L.D. and M. Huff, *Partial oxidation of CH<sub>4</sub> and C<sub>2</sub>H<sub>6</sub> over noble metal coated monoliths*, Catalysis Today, 1994. **21**(2-3): p. 443.
- [13] Schmidt, L.D., M. Huff and S. Bharadwaj, *Catalytic partial oxidation reactions and reactors*, Chemical Engineering Science, 1995. **49**: p. 3981.
- [14] Torniainen, P.M., X. Chu and L.D. Schmidt, *Comparison of Monolith-Supported Metals for the Direct Oxidation of Methane to Syngas*, Journal of Catalysis, 1994. **146**: p. 1.
- [15] Vesper, G. and J. Frauhammer, *Modeling steady state and ignition during catalytic methane oxidation in a monolith reactor*, Chemical Engineering Science, 2000. **55**: p. 2271.
- [16] Witt, P.M. and L.D. Schmidt, *Effect of Flow Rate on the Partial Oxidation of Methane and Ethane*, Journal of Catalysis, 1996. **163**(2): p. 465.
- [17] Hickman, D.A. and L.D. Schmidt, *Synthesis Gas Formation by Direct Oxidation of Methane over Pt Monoliths*, J. Catal., 1992. **138**: p. 267.
- [18] Agar, D.W., *Multifunctional reactors: Old preconceptions and new dimensions*, Chemical Engineering Science, 1999. **54**(10): p. 1299.
- [19] Kolios, G., J. Frauhammer and G. Eigenberger, *Autothermal fixed-bed reactor concepts*, Chemical Engineering Science, 2000. **55**(24): p. 5945.
- [20] Friedle, U. and G. Vesper, *A Counter-Current Heat-Exchange Reactor for High Temperature Partial Oxidation Reactions; I. Experiments*, Chemical Engineering Science, 1999. **54**(10): p. 1325.
- [21] Nieken, U., G. Kolios and G. Eigenberger, *Fixed-bed reactors with periodic flow reversal: experimental results for catalytic combustion*, Catalysis Today, 1994. **20**(3): p. 335.
- [22] Boreskov, G.K. and Y.S. Matros, *Flow reversal of reaction mixture in a fixed catalyst bed - a way to increase the efficiency of chemical processes*, Applied Catalysis, 1983. **5**(3): p. 337.
- [23] Peña, M.A., J.P. Gómez and J.L.G. Fierro, *New catalytic routes for Syngas and hydrogen production*, Applied Catalysis A: General, 1996. **144**: p. 7.
- [24] Rostrup-Nielsen, J.R., *Production of synthesis gas*, Catalysis Today, 1993. **18**: p. 305.

- [25] Prettre, M., C. Eichner and M. Perrin, *The Catalytic Oxidation of Methane to Carbon Monoxide and Hydrogen*, Trans. Faraday Soc., 1946. **43**: p. 335.
- [26] Vernon, P., et al., *Partial Oxidation of Methane to Synthesis Gas*, Catalysis Letters, 1990. **6**: p. 181.
- [27] Mallens, E.P.J., J.H.B.J. Hoebink and G.B. Marin, *An investigation on the reaction mechanism for the partial oxidation of methane to synthesis gas over platinum*, Catal. Lett., 1995. **33**: p. 291.
- [28] Kolios, G., J. Frauhammer and G. Eigenberger, *Efficient reactor concepts for coupling of endothermic and exothermic reactions*, Chemical Engineering Science, 2002. **57**(9): p. 1505.
- [29] Kolios, G., J. Frauhammer and G. Eigenberger, *A simplified procedure for the optimal design of autothermal reactors for endothermic high-temperature reactions*, Chemical Engineering Science, 2001. **56**(2): p. 351.
- [30] Kolios, G. and G. Eigenberger, *Styrene synthesis in a reverse-flow reactor*, Chemical Engineering Science, 1999. **54**(13-14): p. 2637.
- [31] Frauhammer, J., et al., *A new reactor concept for endothermic high-temperature reactions*, Chemical Engineering Science, 1999. **54**(15-16): p. 3661.
- [32] Glockler, B., G. Kolios and G. Eigenberger, *Analysis of a novel reverse-flow reactor concept for autothermal methane steam reforming*, Chemical Engineering Science, 2003. **58**(3-6): p. 593.
- [33] Matros, Y. and G. Bunimovich, *Reverse-Flow Operation in Fixed Bed Catalytic Reactors*, Catal. Rev.-Sci. Eng., 1996. **38**: p. 1.
- [34] Nieken, U., G. Kolios and G. Eigenberger, *Fixed-Bed Reactors with Periodic Flow Reversal*, Cat. Today, 1994. **20**: p. 355.
- [35] Eigenberger, G. and U. Nieken, *Catalytic combustion with periodic flow reversal*, Chemical Engineering Science, 1988. **43**(8): p. 2109.
- [36] Elsner, M.P., et al., *The Claus process: teaching an old dog new tricks*, Catalysis Today, 2003. **79-80**: p. 487.
- [37] Elsner, M.P., C. Dittrich and D.W. Agar, *Adsorptive reactors for enhancing equilibrium gas-phase reactions--two case studies*, Chemical Engineering Science, 2002. **57**(9): p. 1607.

- [38] Blanks, R.F., T.S. Wittrig and D.A. Peterson, *Bidirectional adiabatic synthesis gas generator*, Chemical Engineering Science, 1990. **45**(8): p. 2407.
- [39] de Groote, A.M. and G.F. Froment, *Synthesis Gas Production from Natural Gas in a Fixed Bed Reactor with Reversed Flow*, The Canadian Journal of Chemical Engineering, 1996. **74**: p. 735.
- [40] Gosiewski, K., et al., *Effect of the intra-particle mass transport limitations on temperature profiles and catalytic performance of the reverse-flow reactor for the partial oxidation of methane to synthesis gas*, Chemical Engineering Science, 1999. **54**: p. 4589.
- [41] Gosiewski, K., *Simulations of non-stationary reactors for the catalytic conversion of methane to synthesis gas*, Chemical Engineering Science, 2001. **56**(4): p. 1501.
- [42] Chemical-Equilibrium-Calculation, <http://grashof.engr.colostate.edu/tools/equil.html>.
- [43] NIST-WebBook, <http://webbook.nist.gov/chemistry/>.
- [44] Nowak, E.J., *Prediction of platinum losses during ammonia oxidation*, Chemical Engineering Science, 1969. **24**(2): p. 421.
- [45] Albertazzi, S., et al., *Deactivation of a Pt/[gamma]-Al<sub>2</sub>O<sub>3</sub> catalyst in the partial oxidation of methane to synthesis gas*, Applied Catalysis A: General. **In Press, Corrected Proof**.
- [46] Schicks, J., et al., *Nanoengineered catalysts for high-temperature methane partial oxidation*, Catalysis Today, 2003. **81**(2): p. 287.
- [47] GRI-mechanism, [http://www.me.berkeley.edu/gri\\_mech/](http://www.me.berkeley.edu/gri_mech/).
- [48] Zhu, J., D. Zhang and K.D. King, *Reforming of CH<sub>4</sub> by partial oxidation: thermodynamic and kinetic analyses*, Fuel, 2001. **80**(7): p. 899.
- [49] Aghalayam, P., et al., *A CI mechanism for methane oxidation on platinum*, Journal of Catalysis, 2003. **213**(1): p. 23.
- [50] Veser, G. and L.D. Schmidt, *Ignition and Extinction in the Catalytic Oxidation of Hydrocarbons over Platinum*, AIChE Journal, 1996. **42**: p. 1077.
- [51] Schmidt, L.D., *The Engineering of Chemical Reactions*, ed. K.E. Gubbins. 1998: Oxford University Press.

- [52] Sweeting, T.B., et al., *Reticulated ceramics for catalyst support applications*, Mater. Res. Soc. Symp. Proc., 1994.
- [53] Pearson, J.R.A., *A note on the " Danckwerts " boundary conditions for continuous flow reactors*, Chemical Engineering Science, 1959. **10**(4): p. 281.
- [54] PdexPACK-code, <http://elib.zib.de>.
- [55] Nowak, U., J. Frauhammer and U. Nieken, *A fully adaptive algorithm for parabolic partial differential equations in one space dimension*, Computers & Chemical Engineering, 1996. **20**(5): p. 547.
- [56] Vortuba, J., et al., *Heat and mass transfer in honeycomb catalysts--II*, Chemical Engineering Science, 1975. **30**(2): p. 201.
- [57] Ullah, U., et al., *Monolithic reactors: mass transfer measurements under reacting conditions*, Chemical Engineering Science, 1992. **47**(9-11): p. 2413.